

STRUCTURE-PROPERTY RELATIONSHIPS OF ADVANCED
HIGH TEMPERATURE MATERIALS

Jun Ding

B.E. East China Institute of Technology, Nanjing, China, 1982
M.S. East China Institute of Technology, Nanjing, China, 1985

A dissertation submitted to the faculty of the
Oregon Graduate Institute of Science & Technology
in partial fulfillment of the
requirements for the degree
Doctor of Philosophy
in
Materials Science and Engineering

April, 1995

The dissertation "Structure-Property Relationships of Advanced High Temperature Materials" by Jun Ding has been examined and approved by the following Examination Committee:

Maciej S. Kumosa, Thesis Adviser
Associate Professor

David G. Atteridge
Professor

Jack H. Devletian
Professor

Khalid H. Khan
Professor
University of Portland

Jim T. Stanley
Assistant Professor

DEDICATION

I sincerely dedicate this thesis to
my parents and my wife

ACKNOWLEDGEMENT

I thank Dr. M. S. Kumosa for his guidance and support through this work. I greatly appreciate Dr. W.E. Wood for accepting me as a Ph.D. student. I also thank my thesis committee members, Dr. J.H. Devletian, Dr. D.G. Atteridge, Dr. K.H. Khan and Dr. J.T. Stanley for agreeing to examine my dissertation. I am indebted to Drs. P. Clayton, L. Meekisho, M. Scholl, and M. E. Ziomek-Moroz for their instruction and encouragement to my study here. The financial support from Precision Castparts Corporation and Oregon Metal Initiative is gratefully acknowledged. I deeply appreciate the many valuable discussions I had with my fellow students M. Balakrishnan, V. Dikshit, L. Fang, N. Jin, and R. Parthasarathy. I wish to thank Dr. L. Korusiewicz for his cooperative work in high-temperature mechanical tests of the superalloy. Special thanks are due to my wife, Baoyu Lin, for her patience, understanding and support.

TABLE OF CONTENTS

TITLE PAGE	i
APPROVAL PAGE	ii
DEDICATION	iii
ACKNOWLEDGEMENT	iv
TABLE OF CONTENTS	v
LIST OF TABLES	viii
LIST OF FIGURES	ix
ABSTRACT	xiii
INTRODUCTION	1
CHAPTER 1 LITERATURE SURVEY	6
1.1. Superalloys	6
1.1.1. Microstructures of Superalloys	7
1.1.2. Properties of Superalloys	9
1.2. Intermetallics	11
1.2.1. Features of Intermetallics	11
1.2.2. Ti-Al Intermetallic System	14
1.3. Comparison Between Superalloys and Intermetallic Alloys	16
1.4. Factors Affecting the Room-temperature Ductility of TiAl Intermetallics	19
1.4.1. Effect of Stoichiometry	19
1.4.2. Effect of Alloying Elements	20
1.4.3. Effect of Impurities	23
1.5. Theories of the Brittle Nature of TiAl Intermetallic Alloys	25
1.5.1. Effect of Crystal Structure	25
1.5.2. Effect of Covalent Bond	26
1.6. Post-cast Treatments	28
1.6.1. Hot Isostatic Pressing	28

1.6.2. Heat Treatment of Superalloys	29
1.6.3. Heat Treatment of Intermetallic Alloys	31
CHAPTER 2. MATERIALS AND EXPERIMENTS	39
2.1. Materials	39
2.1.1. Superalloy X	39
2.1.2. 48-2-2 TiAl Intermetallics	41
2.2. Experiments	42
2.2.1. Tensile Test	43
2.2.2. Creep Test	43
2.2.3. Creep Crack Growth Test	43
2.2.3.1. Crack Length Measurement	43
2.2.3.2. Testing Procedure	45
2.2.4. High Temperature Low Cycle Fatigue Tests	48
2.2.5. TEM and SEM Examinations	48
CHAPTER 3. RESULTS AND DISCUSSION (SUPERALLOY X)	56
3.1. Creep Test	56
3.1.1. Creep Behavior of Superalloy X as a Function of Grain Size and Applied Stress	56
3.1.2. Creep Rate	57
3.1.3. Microstructural Effects on Creep Behavior	59
3.2. Creep Crack Growth Test (Constant K Test)	61
3.2.1. Parameters Describing the Creep Crack Growth Behavior . .	61
3.2.2. Creep Crack Growth in the Fine Grain Material	63
3.2.3. Creep Crack Growth in the Coarse Grain Material	64
3.2.4. Microstructural Effects on Creep Crack Propagation	65
3.3. Fatigue Test	69
3.3.1. Low Cycle Fatigue With and Without Holding Time	69
3.3.2. Microstructural Effects on Fatigue Behavior	71

CHAPTER 4. RESULTS AND DISCUSSION (48-2-2 TiAl ALLOY)	99
4.1. Effect of Solidification Rate on RT Ductility	99
4.2. Effect of Microstructure on RT Ductility	102
4.3. Testing Temperature Effect	104
4.4. Effects of Phase Constituents on Plastic Deformation of 48-2-2 TiAl Alloy	107
4.4.1. Defect Configurations in Deformed Samples	109
4.4.2. Function of α_2/γ Interface	110
4.4.3. Function of γ Phase	112
4.4.4. Function of α_2 Phase	114
4.4.5. Volume Fraction Control of α_2 Phase	115
CHAPTER 5. CONCLUSIONS AND SUGGESTIONS FOR FUTURE WORK	134
5.1. Conclusions	134
5.2. Suggestions for Future Work	135
REFERENCE	137
VITA	150

LIST OF TABLES

Table 1.1	Some potential intermetallic compounds	13
Table 1.2	General properties of Ti, TiAl, Ti ₃ Al and superalloys	17
Table 1.3	Alloying effects observed in gamma-based alloys	22
Table 1.4	Metallurgical factors controlling the ductility of γ alloys	24
Table 2.1	Room and high temperature properties of Superalloy X	41
Table 2.2	Representative room temperature physical and mechanical properties of Ti-Al intermetallics	42
Table 3.1	Creep test results for both fine and coarse grain materials	59
Table 3.2	Creep crack propagation rate in fine grain samples	65
Table 4.1	Tensile properties of the specimens with different solidification rates	100
Table 4.2	Tensile properties of 48-2-2 TiAl alloy with different microstructures	104
Table 4.3	Tensile properties of 48-2-2 TiAl alloy at different test temperatures	105

LIST OF FIGURES

Figure 1.1	Ti-Al binary phase diagram	33
Figure 1.2	Atomic arrangement in the lattices and the close-packed planes of γ -TiAl and α_2 -Ti ₃ Al structures in the stoichiometric compositions	34
Figure 1.3	A partial Ti-Al phase diagram near the stoichiometric TiAl composition	35
Figure 1.4	The effect of Cr addition on the plasticity of wrought γ -base alloys	36
Figure 1.5	Charge density in the (100) plane of copper	37
Figure 1.6	Charge density in the (100) plane of CuAu intermetallic alloy	37
Figure 1.7	Charge density in the (100) plane of TiAl intermetallic alloy	38
Figure 2.1	Morphology of γ' phase in Superalloy X	50
Figure 2.2	Morphology of γ'' phase in Superalloy X	50
Figure 2.3	Morphology of δ phase in Superalloy X	51
Figure 2.4	Microstructure of coarse grain sample	51
Figure 2.5	Microstructure of fine grain sample	52
Figure 2.6	Microstructure of 48-2-2 TiAl alloy	52
Figure 2.7	Lamellar structure in 48-2-2 TiAl alloy	53
Figure 2.8	Specimen for tensile test	53
Figure 2.9	Taped double cantilever beam specimen	54
Figure 2.10	Compact tension specimen	55
Figure 3.1	Stress-strain diagram at a constant creep time of 50h	75
Figure 3.2	Strain-time diagrams under creep conditions for different σ /YS ratio	76
Figure 3.3	Creep rates versus stress for fine and coarse grain materials	77
Figure 3.4	Crack propagation path in a creep tested coarse grain sample	77
Figure 3.5	Persistent slip band in a creep tested coarse grain sample	78
Figure 3.6	Creep crack initiation in a fine grain sample	78

Figure 3.7	Creep crack propagation rate, da/dt, versus the stress intensity factor, K	79
Figure 3.8	Time of crack incubation as a function of the stress intensity factor in constant K specimen tests	80
Figure 3.9	Creep crack propagation rate, da/dt versus the effective driving force, $G_e \sim K^2 - K_{th}^2$	81
Figure 3.10	Stress intensity history used in the coarse grain specimens	82
Figure 3.11	Crack profile of a coarse grain sample (TAP3)	83
Figure 3.12	Crack profile of a coarse grain sample (TAP3)	84
Figure 3.13	Crack profile of a fine grain sample (TAR4)	85
Figure 3.14	Crack tip structure of a fine grain sample (TAR1)	86
Figure 3.15	Crack tip structure of a fine grain sample (TAR2)	86
Figure 3.16	Crack tip structure of a fine grain sample (TAR3)	87
Figure 3.17	Crack tip structure of a fine grain sample (TAR4)	87
Figure 3.18	Crack tip structure of a fine grain sample (TAR5)	88
Figure 3.19	Potential drop versus number of cycles in fatigue tests without holding time effect	89
Figure 3.20	Comparison of crack propagation rates in coarse and fine grain samples	90
Figure 3.21	Fatigue (with holding time) crack propagation rates versus the stress intensity factor range in coarse and fine samples	91
Figure 3.22	Crack profile of a fatigued fine grain sample	92
Figure 3.23	Crack profile of a fatigued (with holding time) fine grain sample	93
Figure 3.24	Fractograph of a fatigued fine grain sample	94
Figure 3.25	Fractograph of a fatigued fine grain sample	94
Figure 3.26	Crack tip morphology of a fatigued fine grain sample	95
Figure 3.27	Crack profile of a fatigued coarse grain sample	96

Figure 3.28	Crack profile of a fatigued (with holding time) coarse grain sample	97
Figure 3.29	Crack tip morphology of the crack profile in Fig. 3.27	98
Figure 3.30	Crack tip morphology of the crack profile in Fig. 3.28	98
Figure 4.1	Microstructure of the sample with slow solidification rate	118
Figure 4.2	Microstructure of the sample with medium solidification rate	118
Figure 4.3	Microstructure of the sample with fast solidification rate	119
Figure 4.4	Fractograph: River pattern	119
Figure 4.5	Fractograph: Cleavage along certain crystal plane	120
Figure 4.6	Fractograph: Cracking through lamellar area	120
Figure 4.7	Fractograph: Delamination of α_2/γ interfaces	121
Figure 4.8	Fractograph: Cleavage	121
Figure 4.9	Microstructure of the As-Cast sample	122
Figure 4.10	Microstructure of the As-HIP sample	122
Figure 4.11	Microstructure of the HIP+HT sample	123
Figure 4.12	Fractograph of the As-Cast sample	123
Figure 4.13	Fractograph of the As-HIP sample	124
Figure 4.14	Fractograph of the HIP+HT sample	124
Figure 4.15	Fractograph of the sample tested at 760 °C	125
Figure 4.16	Dislocation configuration in deformed γ phase	126
Figure 4.17	Twins in deformed lamellar structure	126
Figure 4.18	Interaction between a row of dislocations and a stacking fault	127
Figure 4.19	Stacking faults in γ phase	127
Figure 4.20	Dislocation network in deformed γ phase	128
Figure 4.21	Defect configurations in deformed lamellar structure	128
Figure 4.22	Tangled dislocations near grain boundary and parallelly arranged dislocations in γ grain	129

Figure 4.23	Defects configuration in deformed lamellar structure	129
Figure 4.24	SAD pattern from α_2/γ interface	130
Figure 4.25	Atomic arrangement on α_2/γ interface	131
Figure 4.26	Arrangement of dislocations along α_2/γ interface	132
Figure 4.27	Dislocation network in deformed α_2 phase	132
Figure 4.28	Backscattered electron images of 48-2-2 samples with different heat treatment	133

ABSTRACT

STRUCTURE-PROPERTY RELATIONSHIPS OF ADVANCED HIGH TEMPERATURE MATERIALS

JUN DING

Oregon Graduate Institute of Science and Technology

1995

Thesis Adviser: Maciej S. Kumosa

This study investigated the structure-property relationships of a newly developed Ni-based cast superalloy and a γ -based TiAl alloy.

The investigation on the superalloy concentrated on understanding the effect of grain size and precipitate morphology on crack growth under creep and low cycle fatigue conditions at elevated temperatures. A series of mechanical tests conducted on fine and coarse grain samples revealed significant differences in mechanical properties. Fine grain samples had a much lower fracture toughness compared to coarse grain samples. In addition, when holding periods at the peak load were imposed, the fatigue crack growth rate of the fine grain material accelerated, in sharp contrast to the constant crack growth of the coarse grain material. Analysis of the samples before and after testing for microstructural changes and crack growth mechanisms indicated the importance of grain size and microstructure on high temperature properties. For example, a high volume fraction of large δ plates significantly weakened the precipitate strengthening effect. Also, the δ -rich regions acted as preferred crack initiation sites and crack propagation paths.

The mechanical behavior of a γ -based TiAl alloy on variations in solidification rate, post-cast heat treatment and testing temperature was determined. After mechanical testing, samples were examined for deformation-induced defects and fracture surface morphology. These analyses were used to correlate the macro-mechanical behavior to the micro-mechanism of deformation. TEM examination revealed that, in the tested samples, equiaxed γ grains had the highest defect density and the α_2 plates had the lowest. The role of α_2 and its contribution to the plastic deformation of the alloy were discussed based on the defect configuration. It showed that α_2 itself had little direct participation in the deformation process. However, its appearance indirectly assisted the deformation of γ . This conclusion supported the bond theory which attributes the brittleness of the TiAl intermetallic to its covalent bond, and explained the ductility behavior for a wide composition range of γ -based TiAl alloys.

INTRODUCTION

Selection of materials for applications in the design and fabrication of advanced airframes and aeroengines requires a primary consideration of keeping weight to a minimum, so as to get a higher thrust-to-weight ratio and to maximize specific strength and stiffness (1-4). The employment of new materials capable of withstanding higher temperatures and having a lower density results in reduction of the cooling air in the hot section of the engine and a reduction in weight (1). In addition, the efficiency and thrust of the propulsion system are dependent on the peak operating temperature of the combusting gas. The performance efficiency of civil and military jet engines, like any other heat engines, increases with the peak operating temperature. Increment in peak temperature will result in both a higher thermal efficiency and a higher power output for an engine with a fixed size (1). However, the current limits of the peak temperature are set by the thermal constraints on materials. Based on the above considerations and other requirements from operating conditions, the ideal materials for the next generation jet engines should have:

- a combination of high melting point and low density;
- strong mechanical properties, including good elevated temperature strength and stiffness, superior creep strength and certain room-temperature ductility;
- good oxidation and corrosion resistance.

Since it is very difficult to find a single material which has all of the properties mentioned above, for a long period, the material problem has been the major obstacle to building high performance jet engines.

Conventional materials which are currently used in the aerospace industries are various superalloys and titanium alloys. These materials have reached their upper temperature limit of utilization. For example, the upper temperature limit of the most commonly used Ni-based superalloy-Inconel 718 is around 600 °C, and the applications of advanced titanium alloys are confined to the temperature range below 600 °C because of the consideration of strength, oxidation, damage tolerance and fire resistance. While studies continue on the improvement of these two alloy systems, the aerospace industry is in search of "alternative" materials which would be lighter, stronger, and have a higher operating temperature potential compared with the presently available alloys (1,3).

In recent years, great efforts have been undertaken to develop light weight materials with good high temperature properties (1, 3-7), especially in the USA, motivated by projects such as IHPTET (Integrated High Performance Turbine Engine Technology), HITEMP (The Advanced High Temperature Engine Materials Technology Program), and NASP (National Aerospace Plane) (1, 6). The following material systems are considered as potential candidates (1, 8-16):

- intermetallic compounds (monolithic and composite)
- high temperature metallic composites
- refractory metals
- structural ceramics
- ceramic/ceramic composites

Among these material systems, intermetallic compound and intermetallic matrix composites are well known in offering great potential for high temperature applications owing to their low density as well as good high temperature strength capabilities.

Two high-temperature materials were studied in this research, a newly developed Ni-based Superalloy X¹ which is currently used in jet engines, and a γ -based TiAl alloy which is considered as one of the most potential candidates of next generation materials for jet engine applications.

Superalloy X is a precipitation-hardened cast superalloy and has been developed to satisfy the needs for structural component applications in advanced aircraft engines. This superalloy has a higher temperature limit than Inconel 718. It is designated for some components in jet engines where materials are required to have sufficient resistance to high temperature deformation, including creep-fatigue-environmental interaction. The experimental and analytical studies on this material concentrated on the relationship between microstructure and high temperature mechanical properties. High temperature mechanical tests such as creep, creep crack growth, low cycle fatigue and low-cycle fatigue with holding time, were carried out on the Superalloy X samples with different grain sizes. The phenomena of crack extension due to creep deformation and damage in the crack tip region in response to sustained or slowly varying load were investigated. Further studies on the interaction between cracks and microstructures were conducted to correlate metallurgical factors to mechanical behavior of the alloy. Experimental results showed that the difference in the distribution, morphology and volume fraction of intermetallics, especially the δ phase, was one of the most important origins to the variation in mechanical properties.

For the γ -based TiAl alloy, structure-property relationships were studied based on results from mechanical testing and microstructure analysis. Major efforts were focused on room-temperature (RT) ductility improvement, because the low RT ductility and fracture toughness are considered the primary obstacle which has

¹The commercial name of the alloy is confidential information

prevented the immediate application of this material in jet engine industry.

Experimental investigations were done to examine the effects of solidification rate, testing temperature, and post-cast treatment on mechanical property. Fractograph and deformation-induced defects were checked after mechanical tests to correlate the macro-mechanical behavior to the micro-mechanism of deformation.

With the increase in solidification rate, the room temperature ductility increased and fracture mode changed from pure cleavage to quasi-cleavage. This improvement came from several sources such as refined metallurgical structure, more uniform element distribution and more ductile γ phase. Various factors which affect the room temperature ductility of TiAl were also discussed. Unlike in some single crystal intermetallic alloys where yield strength increased with increase in temperature, a negative dependence of yield strength on the testing temperature was found in this alloy. Ultimate strength increased slightly with increasing temperature. Grain boundary deformation and strain hardening were believed to be responsible for this phenomenon.

By comparing deformation-induced defects configurations in each phase, it was found that initiation and slip of dislocations in γ -phase carried out the major part of plastic deformation and planar defects such as stacking faults and twins also played important roles. The α_2 phase indirectly assisted the plastic deformation but it had little direct contribution to room temperature ductility. The difference in plastic deformation ability between γ and α_2 phases was reflected by the difference in defect density and delamination fracture mode which was an indication of stress concentration on the γ/α_2 interfaces.

Based on the findings from this study and a theory in which the brittle nature of TiAl alloy was attributed to the appearance of the covalent bond between d electron

of Ti atom and p electron of Al atom, the influences of Ti/Al ratio and alloying element on room temperature ductility were interpreted. It was also found that the bond system can be improved by supersaturation of Ti atoms in γ -phase with suitable heat treatment.

CHAPTER 1

LITERATURE SURVEY

This work focussed on the structure-property relationships of a Ni-based Superalloy X and a γ -based TiAl intermetallic alloy.

This literature survey was conducted to assist the experimental design and results analysis. The following major areas were briefly covered: microstructure and property features of superalloys and intermetallics, factors affecting the room-temperature ductility of TiAl intermetallics and relevant theories, property comparison between these two alloys, and their post-cast treatments.

1.1. Superalloys

Superalloys are a group of iron, nickel or cobalt-based alloys which provide the necessary strength capabilities and oxidation resistance for high temperature applications. These properties, together with their low thermal expansion, good corrosion resistance and microstructural stability, have led to their use in gas turbines for such components as blades, vanes and discs (17-20). Their application did raise the engine operating temperature significantly (14). Other elevated temperature applications of superalloys are found in nuclear industry, power generation, coal gasification and hydrogen production equipment (19).

From the 1930's to the mid-1960's, a wide range of superalloys evolved by various discoveries of unique effects of compositional changes on the properties (14, 18). Later, more efforts have been directed towards the processing of these alloys

(21-35), from the melting methods such as Vacuum Induction Melting (VIM) - Vacuum Arc Remelting (VAR), Vacuum Induction Melting - Electroslag Remelting (ESR) and Electron Beam Remelting (EBR) to post-cast heat treatment procedures such as Thermal Mechanical Processing (TMP) and Hot Isostatic Pressing (HIPing) techniques. Many of these efforts focused on the improvement of the quality, performance and working temperature range.

Only relevant issues of Ni-base superalloys were summarized in the following sections and specific microstructure of Superalloy X was included in the Materials and Experiments Chapter (Chapter 2).

1.1.1. Microstructures of Superalloys

Although superalloys have complex compositions, they are microstructurally simple when compared with steels. The microstructure consists of the austenitic FCC matrix phase and various secondary phases, including carbides (MC , $M_{23}C_6$, M_6C), intermetallic compounds (γ' , γ''), and some unwanted or less desirable phases such as σ and Laves phases (19). These phases are distributed either through the matrix or along the grain boundaries. Superalloys may be produced, depending on the consideration of cost, property and application, in the forms of cast, wrought and powder.

Austenite Matrix

The Ni-matrix phase has a face centered cubic (FCC) crystal structure and contains solid solution strengtheners. The solid strengthening effects are proportional to the difference in atom size between the matrix and the solute atoms (19). The main solid solution strengtheners include Cr, Mo, W, Fe and Co (36).

Gamma Prime Precipitates (γ')

This intermetallic compound is considered to be the main strengthening phase in many superalloys and is an ordered FCC phase with $L1_2$ crystal structure. It has a general chemical formula of Ni_3Al . The strengthening effect comes from two sources (19): coherency strain due to coherent lattice relationship between γ' and the parent phase, and antiphase boundary (APB) energy due to dislocation penetration through the ordered structure. The γ' phase is quite stable. It precipitates as a round particle whose size can be less than 200 Å and keep its round shape when it coalesces at higher temperature (37). The γ' formers are Al, Ti, and Nb (36).

Gamma Double Prime Precipitates (γ'')

In some limited systems where sufficient Nb (or Nb+Ta) is present, alloys are strengthened primarily by γ'' precipitate which has an ordered body centered tetragonal (BCT, DO_{22}) crystal structure. The compound has a chemical formula of Ni_3Nb . The mechanisms for its strengthening effect are same as that for γ' . The orientation relationships between γ'' phase and the matrix are $\{100\}_{\gamma''} // \{100\}_{\gamma}$ and $\langle 001 \rangle_{\gamma''} // \langle 001 \rangle_{\gamma}$ (19). The stability of γ'' is not as good as γ' phase. When used at elevated temperatures, for example, above 650°C, it may transform to δ phase. The γ'' phase has a disk shape with a diameter/thickness ratio of 5 to 6. It keeps disk shape when grows at higher heat treatment temperatures (37).

Delta Phase (δ)

This phase has an exactly same chemical formula (Ni_3Nb) but different crystal structure (ordered orthorhombic, DO_8) as γ'' phase. It has a platelike geometry with much bigger size than both γ' and γ'' . It exists owing to compositional, processing or exposure effects (19, 37). As will be discussed in the Chapter 3, this phase has

strong influences on the high temperature mechanical behavior of Superalloy X.

1.1.2. Properties of Superalloys

The innovation of superalloys was a truly remarkable achievement. More than forty years of metallurgical research and engineering development have advanced nickel-based superalloys to remarkable levels of engineering utility. There is no other alloy class offering the total balance of engineering properties in polycrystalline form, and there is no other structural material which offers a service temperature at as high a fraction of its melting point as the superalloys in single crystal form (5).

The Ni-base alloys in particular are able to sustain loads of 170 MPa for thousands of hours, running at temperatures of the order of $0.8T_{mp}$ (14). Their moduli of elasticity are in the vicinity of 207 GPa. And due to austenitic FCC matrices, it has very good ductility and high solubility for some alloying additions (18). Compared to other metal systems, their physical properties such as electrical conductivity, thermal conductivity and thermal expansion tend to be low (18). High content of Ni, Cr and Al contributes to the strong oxidation resistance and hot corrosion resistance. With these superior properties, superalloys have been widely used in aerospace industry in the last several decades.

Since the performance of modern jet engines is still limited by the thermal constraints of materials, great efforts have been put into raising the upper working temperature limits of superalloys. Some advances have been achieved by means of more complex alloy composition (38-39), more exquisite microstructure control (38, 40) and special techniques such as single crystals (41-44) and thermal barrier coatings (45). However, further substantial increase in the effective operating temperature of superalloys becomes extremely difficult because of their melting points and bond strengths.

Applications of superalloys in modern jet engines are confined by their property limitations.

They are too dense to be used for building large structures that must leave ground. The average density of superalloys is 8.3 g/cm^3 . Civil market surveys suggest that to the year 2000 more than half the engine purchases (by value), will be for large aircraft cruising at Mach 0.8, and above, and carrying more than 200 passengers over long distances. For such aircraft fuel efficiency predominates (46), therefore, a decrease in weight will improve range/payload performance. Light weight materials have to be used to replace superalloys.

Their working temperature capability is limited. For example, among many commercially available superalloys, alloy 718 stands out as the most dominant alloy in superalloy production. In 1986, this grade achieved 45% of the total production of nickel-base alloys in wrought form, and 25% in cast form. However, its upper temperature limit is around $600^\circ\text{C} \sim 650^\circ\text{C}$. Long term exposure at a point above this limit will cause a significant degradation of mechanical properties.

Another disadvantage of superalloys is the lack of phase stability after prolonged exposure at high temperatures. For instance, in γ' -strengthening nickel-based alloys, γ' precipitation is not the equilibrium phase. When overaged, it will be replaced by the more stable δ phase. Such transformation will degrade the alloy properties (47). Morphologically, compared with γ' phase, δ precipitate has larger dimensions and tend to aggregate at grain boundaries. Very limited literature is available that discusses how to improve the phase stability of γ' - and γ'' -hardened alloys (48-49).

Beginning about 30 years ago, attention was drawn to another family of materials, intermetallics whose mechanical behaviors were little known, yet which

exhibited a great diversity of crystal structures, compositions, and often very high melting points.

1.2. Intermetallics

1.2.1. Features of Intermetallics

The intermetallic compounds (1), in scientific terms, may be defined as phases or compounds between metallic atoms with either well defined integral atomic ratios or having a limited range of possible compositions. These compounds possess a crystallographic structure with long range order (LRO) which may either remain ordered till the melting point or become disordered at a lower characteristic temperature. Deviation from the stoichiometry may have a profound effect on the mechanical properties. It should also be noted that the defects in LRO such as anti-phase boundaries and domains play an important role. According to R.A. Varin and M.B. Winnicka, intermetallics have a number of properties which make them very attractive for high temperature applications (51):

- (a) Intermetallics are intrinsically strong and their strength does not degrade rapidly with increasing temperature. Compounds having the $L1_2$ (ordered FCC) and some with B2 (ordered BCC) crystallographic structures show an increase of yield and flow stresses with increasing temperature;
- (b) Those intermetallics formed from various combinations of aluminum, titanium and silicon, i.e. aluminides and silicides, have low or very low densities. This gives rise to high specific properties (modulus and strength divided by density) which are particularly important for aerospace and transportation applications;
- (c) Elastic moduli of intermetallics are quite high and they tend to decrease more slowly with increasing temperature than for the disordered alloys;
- (d) Intermetallics with high aluminum content are expected to have good oxidation

resistance at high temperatures;

- (e) Due to their ordered structure, intermetallics exhibit lower self-diffusion coefficients and this results in a slower rate of creep, recrystallization and corrosion.

However, the problems encountered with the intermetallic compounds are substantial. In particular, their low room temperature (RT) ductility and fracture toughness constitute a serious but not an unsurmountable barrier for their successful use as structural materials. Among the vast number of intermetallics identified to date, very few have been considered for structural applications, as shown in Table 1.1 (1). It can be seen from the table that most of these intermetallics have a disadvantage of low ductility.

Table 1.1 Some Potential Intermetallic Compounds (1)

Compound	Advantages	Disadvantages
Advanced potential candidates		
Ti₃Al	Density	Oxidation
TiAl	Density	Ductility
FeAl	Ductility, Oxidation	Melting point, Density
NiAl	Melting point, Oxidation	Ductility
Far term application (speculative)		
Ti₅Si₃	Density	Ductility
Nb₅Si₃	Melting point	Ductility, Oxidation
Nb₃Al	Melting point	Ductility, Oxidation
NbAl₃	Melting point, Density	Ductility, Oxidation
TiAl₃	Density	Ductility
MoAl₂	Melting point	Ductility, Oxidation
Nb₂Be₁₇	Melting point	Ductility, Oxidation
ZrBe₁₃	Melting point	Ductility, Oxidation

The intermetallics for structural applications, according to their perspectives of engineering employments, can be divided into three major categories (1):

- nickel aluminides (Ni₃Al and NiAl)
- titanium aluminides (Ti₃Al, TiAl and TiAl₃)

-other intermetallics

Only some aspects of intermetallics in Ti-Al system will be discussed here.

1.2.2. Ti-Al Intermetallic System

Intermetallics of the Ti-Al system offer a favorable combination of good strength, high temperature oxidation resistance and low density as compared with the currently used superalloys (1-2,9,11,52-55). In this category of intermetallics, there are three types of aluminides: TiAl_3 , TiAl and Ti_3Al , as shown in the Ti-Al binary diagram (Figure 1.1) (56).

Ti_3Al : The Ti_3Al , so called α_2 phase, has an ordered hexagonal structure. The stoichiometric compound has a density of 4.2 g/cm^3 but when alloyed with other elements, it is closer to that of the titanium alloys (4.7 g/cm^3). This intermetallic is the ordered form of the α (hexagonal) phase. The crystal structure is shown in Figure 1.2 (57). Ti_3Al -based alloys are not expected to provide any density advantage over the Ti-based alloys but they can extend the temperature capability of the currently used titanium alloys, which is about 600°C (1).

TiAl_3 : The information available on TiAl_3 or TiAl_3 -based intermetallics is scarce. TiAl_3 is a light compound which has a melting point of 1340°C and a density of 3.37 g/cm^3 . Because of the excellent oxidation resistance, good yield strength and low density, the TiAl_3 -based intermetallics are obviously of great interest. However, all attempts to improve its room temperature ductility have not been successful (1).

TiAl-based intermetallics: The TiAl-based alloys contain 46 to 54 at. % of aluminum and can be divided into single phase γ alloys and two-phase $\alpha_2 + \gamma$ alloys.

The γ TiAl has an ordered $L1_0$ structure. It remains ordered up to its melting point of about 1450°C. It is formed by the alternating package of Ti and Al atom layers as shown in Figure 1.2.

The oxidation resistance of TiAl-based alloys is much higher than those of the Ti_3Al (α_2) type alloys. The temperature potential of such alloys is up to 950°C for structural applications (1). It is generally believed (58) that the single phase alloys are extremely brittle but the two-phase binary alloy Ti-48 at. % Al shows a ductility of about 2%. Compared to the Ti_3Al intermetallic, the development of TiAl alloy is much more recent. The major concerns regarding the mechanical properties are with respect to high fatigue crack growth rates (compared with superalloys, for example), low fracture toughness, ductility and impact resistance at room temperature. The creep resistance of the TiAl-based alloys is strongly dependent on alloy chemistry and the microstructure.

A variety of microstructures can be obtained in the two-phase alloys (46-50 at. % Al). Phase transformation studies in the two-phase region are important in order to understand deformation behavior and to facilitate processing. The as-cast microstructure of a binary alloy containing 48 at. % Al is lamellar, subsequent heat treatments in the two-phase $\alpha + \gamma$ region lead to a microstructure of lamellar grains and primary equiaxed gamma grains, and is referred to as the duplex structure. The lamellar grains consist of alternate layers of γ and α_2 platelets. The ductility of such an alloy can be attributed to the existence of a fine lath microstructure formed by the presence of a low volume fraction of the α_2 phase in the γ matrix. The fine lath microstructure is thought to favor both twinning and slip.

Another type of microstructure within this composition range is the so called "fully transformed" structure. To obtain such a structure, samples need to be heat treated in the α phase region. The grains are typically greater than 500 μ m in

diameter.

1.3. Comparison Between Superalloys and Intermetallic Alloys

It should be noted that there is a natural relationship between superalloys and intermetallics. Most of superalloys developed in the last 50 years contain a significant volume fraction of intermetallic compounds which make these alloys high-temperature resistant, although in the beginning the beneficial effects of intermetallic compounds were not fully recognized. In spite of the long history for people to acquire intermetallic materials, it is clear that a significant new level of activity began in the late 1950's, with a real explosion of work on setting in the mid-1980's (14).

At present, various superalloys are major materials used in jet engines. The remainders are various titanium alloys and other alloys. The γ -based TiAl alloy is a most promising next generation jet engine material and it was successfully cast into some major engine parts such as blades and turbocharger wheels. However, before we can make full use of the alternative materials such as intermetallics, the development and/or improvement of currently used superalloys is necessary. Table 1.2 lists important properties for both currently used superalloys and titanium alloys, and next generation materials TiAl and Ti₃Al.

Table 1.2 General Properties of Ti, TiAl, Ti₃Al and Superalloys (59)

Property	Ti-Base Alloy	Ti ₃ Al-Base Alloy	TiAl-Base Alloy	Super-alloy X	General Superalloy
Density (g/cm ³)	4.5	4.1-4.7	3.7-3.9	-	8.3
RT Modulus (GPa)	96-115	120-145	160-176	220.6	206
Yield Strength (MPa)	380-1150	700-990	400-630	800-1000	-
Tensile Strength (MPa)	480-1200	800-1140	450-700	1100-1300	-
Creep Limit (°C)	600	750	1000	-	1090
Oxidation (°C)	600	650	900-1000	-	1090
Ductility (%) at RT	10-20	2-7	1-3	6-8	3-5
Ductility (%) at HT	High	10-20	10-90	13	10-20
Structure	hcp/bcc	D0 ₁₉	L1 ₀	fcc/L ₁₂	fcc/L ₁₂

Note: This table was produced by combining data from (59) and test results from this study.

The density of γ -based TiAl intermetallic (3.8) is less than half of superalloys (8.3). From the point of saving weight, TiAl is much better than Superalloy X.

Actually, superior density is one of the major advantages of TiAl alloys (even better than general Ti-alloys).

Superalloy X has higher RT yield strength and RT fracture strength than TiAl. However, the high temperature properties and specific strength are most important properties for jet engine materials. Experiments in this study (Chapter 4) have shown that, within certain temperature range (from RT to about 800°C), the yield strength of 48-2-2 alloy decreases slowly and the ultimate strength increases slightly with increasing temperature. This offers TiAl another important feature, i.e. this material system has quite stable strength at elevated temperature. Gamma alloys have a potential for structural applications in the temperature range of 650 to 900°C (1202 to 1652°F), even to 950°C.

Although the major disadvantage which stops engineering application of TiAl alloy is its low RT ductility (1-3% in elongation), it is encouraging that a lot of advances have been reached in the last several years (11,13,61-62), and it appears that its RT ductility can be enhanced with a little degradation in its superior high temperature mechanical properties.

The roles of intermetallics are different in these two materials. In Superalloy X, intermetallics γ'' and γ' act as precipitation-strengthening phases and another intermetallic phase δ may enhance creep deformation resistance. Although the distribution and morphology of intermetallics have a very important influence on mechanical properties, Superalloy X has many common features of metals such as good ductility. In TiAl alloy, both the matrix (γ) and the second phase (α_2) are intermetallic compounds. The physical and mechanical behaviors of the alloy are determined by these intermetallics. TiAl alloy has characteristics of compounds such as low RT ductility and low self-diffusion coefficients.

1.4. Factors Affecting the Room-temperature Ductility of TiAl Intermetallics

The ductility of TiAl is affected by many factors such as chemical composition, phase constituents, crystal structure and slip system. Literature survey (1,5,8,11,13,63-68) shows that extensive research work has been done in nearly every possible way to understand the deformation mechanisms and to improve the RT ductility of TiAl. Some of the work is concentrated on the following aspects:

1.4.1. Stoichiometry Effect

The stoichiometric chemical composition for TiAl is 50 at. % Al. But the composition of TiAl based alloys can vary from 46 to 54 at. % of aluminum, as shown in Figure 1.3 (69). Within this range, the ductility of TiAl varies very fast as the chemical composition changes. It is reported that for the Ti-Al binary alloy, the maximum ductility appears when the aluminum concentration reaches about 48 at. % (69). Figure 1.4 (69) shows how the RT ductility of TiAl intermetallic alloy changes with different Al contents.

It was reported (58,70) that the transition from single phase to duplex microstructure causes a change in deformation mechanism. A duplex structure is more deformable than a single-phase γ structure. According to Ernest L. Hall (71) and Young-Won Kim (59), high ductility in $\text{Ti}_{52}\text{Al}_{48}$ alloy may be related to the following factors:

- 1) There are more mobile $a/2[110]$ dislocations and $\{111\}$ twins in the alloy. Its lower c/a tetragonality (1.01) favors dislocation slipping;
- 2) Since dislocations with primarily one type of Burgers vector are found in the alloy, the possibility of dislocation reactions decreases and hence fewer sessile obstacles exist;

- 3) Enhanced twinning activity;
- 4) The segregation of interstitials to α_2 phase leaves γ phase essentially free of O_2 and N_2 . This favors deformation in the γ phase.

However, the exact mechanism for stoichiometry effect is not clear. When some other elements such as Cr or Mn are added to the alloy, the optimized Al concentration may shift a little. For example, if the alloy contains 2 at. % Cr, the highest ductility will be reached when Al concentration is about 46 at. %, as shown in Figure 1.4.

1.4.2. Effect of Alloying Elements

Addition of alloying elements can effectively change the properties of Ti-Al alloys such as ductility and oxidation resistance (72-84). The effect of addition of the alloying elements is not unique. In the alloy with chemical formula of $Ti-48Al-xM$ ($M=V, Cr, Mn, Mo, Nb$ or W), additions ($x=1-3$) of vanadium, chromium or manganese increase ductility over $TiAl_{48}$, while niobium or tungsten additions decrease the ductility (59). This effect has been the subject of intensive studies and has been explained in terms of tetragonality, unit cell volume, site occupation and torque effect, twinning, and changes of electronic structure (57).

For example, it is believed (82) that, within some range, the addition of Mn can improve the ductility of TiAl through the following mechanisms: 1) it makes grain size finer, hence the pile-up distance of dislocations become short. In other words, stress concentration is difficult to be established and the material can undergo a larger deformation before fracture; 2) it increases the symmetry and improves the deformation accommodating ability of the material; 3) it can stabilize the twin structure in the alloy, hence the twinning process becomes relatively easy. When ordinary dislocations are stopped by any reason, twinning deformation will make

contribution to plastic deformation; 4) after the addition of Mn, more stacking faults are observed in the deformed TiAl+Mn ternary alloy than in the TiAl binary alloy. This indicates that the motion of superdislocations or partial dislocation produced by splitting superdislocations is another non-negligible contributor to the alloy deformation.

Shyh-Chin Huang (83) summarized the effect of various alloying elements on properties of γ -based TiAl alloy, as shown in Table 1.3.

Table 1.3 Alloying effects observed in gamma-based alloys (83)

ELEMENT	REPORTED EFFECTS
Al	It strongly affects ductility by changing the microstructure. Best ductility typically occurs in the range of 46-50 at. %. Within the ductile Al range, increasing Al decreases the fracture toughness.
B	Additions of >0.5 at. % refine grain size, and improve strength and workability. Doping of B generally increases castability.
C	Carbon-doping increases creep resistance and reduces ductility.
Cr	Additions of 1-3 at. % increase the ductility of duplex alloys. Additions > 2 at. % enhance the workability and superplasticity. Additions > 8 at. % greatly improve the oxidation resistance.
Er	Its additions change the deformation substructures and increase the ductility of single-phase gamma.
Fe	The addition of Fe increases fluidity as well as the susceptibility to hot cracking.
Mn	The addition of 1-3 at. % Mn increases the ductility of duplex alloys.
Mo	The addition of Mo improves the ductility and strength of fine-grained material. It also improves the oxidation resistance.
Ni	It increases fluidity.
Nb	The addition of Nb greatly enhances the oxidation resistance. It slightly improves the creep resistance.
P	Doping of P decreases the oxidation rate.
Si	An addition of 0.5-1 at. % Si improves the creep resistance. The addition of Si also improves the oxidation resistance. The addition of Si increases fluidity, but reduces the susceptibility to hot cracking.
Ta	The addition of Ta tends to improve the oxidation and creep resistances. It increases the susceptibility to hot cracking.
V	The addition of 1-3 at. % V increases the ductility of duplex alloys. Its addition generally reduces the oxidation resistance.
W	The addition of W greatly improves the oxidation resistance. It improves the creep resistance.

1.4.3. Effect of Impurities

It is known that impurities such as nitrogen and oxygen have detrimental effect on the ductility of TiAl alloys (85-91). Kawabata et al. (91) have studied the effect of impurity and second phase on the ductility of TiAl and concluded that ductility is increased by using high purity materials and by the presence of Ti_3Al as a second phase.

Basically, there are two ways to minimize the effects of impurities. One is to lower their content through changing melting and casting methods. Another is to develop specific microstructure with higher solubility for impurities or to add some elements which can combine free interstitial atoms to form a stable compound. For example, the α_2 phase has a higher solubility for oxygen than the γ phase, which may be one reason why the lamellar structure has a better ductility than monolithic γ phase. V.K. Vasudevan et al. reported (86) that, by adding Er into TiAl alloy, Er_2O_3 formed from gettering of interstitial O_2 and the deformation microstructures were dominated by dislocations with $b=1/2 < 110$] and twins. No satisfactory explanation to the mechanism of the function of impurities has been given. The following are several possible reasons (86,89,91):

- 1) Decreasing impurity level can lower the flow stress of the alloy;
- 2) The less the impurity, the more active the dislocation movement. Defects will experience large Peierls stresses in the presence of the interstitial elements. Without them, mobile dislocations such as $b=1/2 < 110$] may be the dominating defects;
- 3) Due to the reduced effect of interstitial on the degree of directionality of covalent bonds, effects of covalence on dislocation mobility will also be reduced with high purity. Then twinning will be promoted by the increased mobility of dislocations with $b=1/6 < 112$].

Although the detrimental effect of oxygen has been recognized undoubtedly and many efforts have been made to minimize oxygen content, due to the high reactivity of titanium, it is very difficult to reduce oxygen to a level below certain limit (such as 500ppm) in γ -based TiAl.

In addition to what have been mentioned above, there are many other factors which can influence the plastic deformation ability of TiAl alloys. Y.-W. Kim (59) summarized the metallurgical controlling factors of RT ductility of γ -based TiAl alloys, as shown in Table 1.4.

Table 1.4 Metallurgical Factors Controlling the Ductility of γ Alloys (59)

Factors	Best Values for Ductility
Al content in γ -phase	Lowest possible
α_2/γ phase volume ratio	0.05-0.15
L/ γ grain volume ratio	0.3-0.5
α_2/γ plate thickness ratio	0.25-0.4
Grain size	Smallest

1.5. Theories of the Brittle Nature of TiAl Intermetallic Alloys

In the most crystal metallic materials, plastic deformation at room temperature is carried out by the initiation and movements of various defects, especially dislocations. The studies of the mechanisms of room temperature plastic deformation are also based the mobility of dislocations.

1.5.1. Effect of Crystal Structure

The γ -TiAl has a $L1_0$ crystal structure with slight tetragonality ($c/a=1.02$) with alternating (002) planes of Ti and Al atoms as shown in Figure 1.2. It has been reported (92-101) that dislocation slip in γ grains generally occurs on $\{111\}$ planes at close-packed directions as in FCC structure, and c/a tetragonality and atomic packing create a non-equivalency of $\langle 110 \rangle$ slip vectors, i.e. $\langle 110 \rangle$ is not equivalent to $\langle 011 \rangle$ and $\langle 101 \rangle$.

Four types $\{111\}$ dislocations have been observed in plastically deformed TiAl (97): $1/2 \langle 110 \rangle$ ordinary dislocations, $\langle 011 \rangle$ superdislocations, $1/2 \langle 112 \rangle$ superdislocations and $1/6 \langle 112 \rangle$ twin dislocations. For these $\{111\}$ dislocations, $1/2 \langle 110 \rangle$ dislocations are the "easy slip" type with high mobility and the lowest energy. The $\langle 011 \rangle$ and $1/2 \langle 112 \rangle$ dislocations are superdislocations with very low mobility and high energy.

Both the ordinary dislocations and superdislocations can further split into some partial dislocations which cause the formation of planar defects such as superlattice intrinsic or extrinsic stacking faults (SISF or SESF), antiphase boundaries (APB) and complex stacking fault (CSF) (71). For example, the $a[101]$ superdislocations can first dissociate into the other two dislocations (71):

$$a [101] \Rightarrow a/2 [110] + a/2 [1\bar{1}2] \quad (1.1)$$

The $a/2[1\bar{1}2]$ superdislocations can further dissociate:

$$a/2 [1\bar{1}2] \Rightarrow a/6 [1\bar{1}2] + (SF) + a/3 [1\bar{1}2] \quad (1.2)$$

After such local dissociations, sessile faulted dipoles are formed due to the existence of $a/6\langle 112 \rangle$ partials. The mechanism for dislocation reaction and dislocation motion during plastic deformation is still not elucidated.

The low mobility of dislocations in TiAl intermetallic alloys are expected due to the appearance of these superdislocations, planar defects, and sessiles.

1.5.2. Effect of Covalent Bond

Within the allotropic metals, those with an FCC structure are known to be ductile. TiAl has a FCT structure with only a c/a ratio 1.02, slightly deviated from FCC ($c/a=1$). Thus it is expected to be ductile too. This has not proven to be the case. While some of the intermetallic alloys with fcc-derived crystal structures are ductile, there are others, with the same structure, which are brittle. For example, both CuAu and TiAl have $L1_0$ structure and the tetragonality is characterized by a c/a ratio of 0.94 for CuAu and 1.02 for TiAl. But CuAu is much more ductile than TiAl (68). It means the mobility of dislocations in CuAu is higher than that in TiAl. Clearly, the FCC-deviated crystal structure and the ordered status are not only factors which are responsible for the brittleness of TiAl.

Recent work (65-68) indicates that the low room temperature ductility of TiAl intermetallics is related to the bonding mechanism. M.E. Eberhart et al. (68)

demonstrated the difference in bonding mechanism between CuAu and TiAl and how it affects fracture behavior. Figure 1.5 is the charge density in the (100) plane of copper. And Figures 1.6 and 1.7 are charge densities in the (100) plane for CuAu and TiAl, respectively. The charge density for CuAu shows a topology that is characteristic of fcc metals (Figure 1.6 is similar to Figure 1.5). There are four first neighbor bonds marked (3,-1)_{cp}. The bond paths are shown as straight lines connecting the bond atoms, and (3, -1)_{cp} occurs near the midpoint of each of these bonds. For TiAl there are four neighbor bonds between the Al atom and Ti atoms. However, the (3, -1)_{cp} corresponding to these bonds do not occur on the internuclear axis. The point is displaced off this axis and nearer the Ti atom, producing a bent bond path. Their analysis indicates that CuAu is topologically fcc and TiAl is topologically inequivalent to the FCC structure. There is a relationship between mechanical properties and this charge density topology.

A material will, in principle, fail in a brittle manner if the local tensile stress operating at the crack tip reaches the cohesive strength before the local shear stress reaches the shear strength. Such a situation may be expected to occur when the shear strength is high owing to the directional p-d interaction. Therefore, the reduction of the Al p-Ti d interaction and probably the enhancement of the d-d interaction are considered to improve the ductility of TiAl. Based on the above analysis, M. Morinaga et al. (65) believe that there are two ways to improve ductility by alloying. One is replacement of Al atoms by transition elements such as Ti, V, Cr, and Mn which strongly enhance the M d-Ti d bond, while keeping a small increase in the M d-Al p interaction. It should be noticed that the addition of some of these elements such as Mn and Cr may decrease the aluminum content in γ -phase and decrease d-p interaction. The other way is the replacement of Al atoms with non-transition atoms, for instance, Mg has the smaller M d-Al p and the larger M d-Ti d interaction than Al. In Chapter 4, another way of adjusting Ti content in γ phase by selecting suitable heat treatment will be discussed. The function of such treatment is similar to the

substitution of transition elements for Al atoms.

1.6. Post-Cast Treatments

The properties of both intermetallic alloys and superalloys are strong functions of the final microstructures. Selection and optimization of post-cast treatment procedures have always been a major topic in the study of high temperature materials.

1.6.1. Hot Isostatic Pressing Process (HIP)

Hot isostatic pressing is a process (28-30) that subjects a component to both elevated temperature and isostatic gas pressure in an autoclave. The most widely used pressurizing gas is argon. For the processing of castings, argon is applied at pressure between 103 and 206 MPa, with 103 MPa being the most common. Process temperatures vary from 480°C for aluminum castings to 1315°C for single-crystal nickel-base superalloys.

When castings are hot isostatically pressed, the simultaneous application of heat and pressure virtually eliminates internal voids and microporosity through a combination of plastic deformation, creep, and diffusion. The elimination of internal defects leads to improved nondestructive testing ratings, increased mechanical properties, and reduced data scatter (30).

The HIP process was invented in the mid-1950s at Battelle Columbus Laboratories. In the early 1970s, investigation into the effect of HIP on titanium and superalloy castings were conducted and it was demonstrated that significant improvements in mechanical properties could be obtained (30). In Inconel 718, General Electric (GE) has obtained tensile properties near those of forgings and notched fatigue strength equal to that of forgings by applying HIP to cast parts. The

yield strength, ultimate strength and elongation increased from 127.5 ksi, 149.1 ksi, 11.8% for the non-HIP'ed material to 140.5 ksi, 165.8 ksi and 16.5% respectively after HIPing (29).

In the last two decades, HIP has become an integral part of the manufacturing process for high-integrity aerospace castings such as turbine blades (28-30). For advanced Ni-based superalloys, microporosity is one of the major factors which affect the mechanical properties. Therefore allowance for microporosity tends to be more stringent and the application of HIP process ensures cast parts with lower porosity level and higher homogenization alloy matrix. One of the earliest successes of HIP as applied to aerospace castings was with investment cast titanium. It has been also successfully utilized in castings of aluminum alloys and stainless steels and now its usage is extended to intermetallic castings. Proper selection of HIP parameters can substantially reduce casting defects which are commonly seen in intermetallic cast parts.

1.6.2. Heat Treatment of Superalloys

Selection of heat treatments for superalloys depends on material composition (Ni, Fe or Co-based), previous fabrication processes (wrought or casting) and component requirements. What will be discussed here is limited to general processes of Ni-based superalloys such as Stress Relieving, Solution, and Aging.

Stress Relieving of heat resisting material usually is confined to alloys that are not age-hardenable. Ni-based alloy castings are seldom stress relieved because they are used in the as-cast, solution treated, or solution treated and aged condition. However, in the following situations, castings may benefit from a stress relief operation: (a) when they are of an extremely complex geometry that might crack during the initial heating-up period in service, (b) when they have very stringent

dimensional tolerances, and (c) after welding operations. Stress relieving temperatures are usually below the annealing or recrystallization temperatures (102).

Solution treatment temperatures of nickel-base alloys are determined primarily by the properties desired after subsequent aging. In wrought alloys, for optimum creep rupture properties, higher solution treating temperatures are used than when optimum short-time tensile yield strength and elongation at elevated temperature are desired. For cast alloys, solution treatment temperatures primarily are a function of incipient melting temperatures as well as furnace capability. Protective atmosphere or vacuum is necessary (102).

Current technology of cast components utilizes a HIP cycle to close porosity and partly achieve homogenization. HIP parameters (time, temperature, pressure) will vary depending on the initial segregation and requirements for grain size control. Most HIP treatments are followed by a post HIP solutioning step to dissolve the structures formed during HIP cool down and then are given a variety of intermediate and final aging cycles to produce γ'' and γ' precipitation (37).

Aging treatments strengthen age-hardenable alloys by causing the precipitation of one or more phases from the supersaturated matrix that is developed by solution treating and retained by rapid cooling from the solution treating temperature. Multi-step aging, or so called TAG aging treatment is usually used. Factors that determine the selection of aging parameters such as number of aging steps and aging temperature include (a) type and number of precipitating phases available, (b) anticipated service temperature, (c) required precipitate size, (d) the combination of strength and ductility desired and heat treatment of similar alloys. Principal aging phases in the nickel-based alloys usually include one or more of the following: γ' [Ni_3Al or $\text{Ni}_3(\text{Al},\text{Ti})$], η (Ni_3Ti), or γ'' (Ni_3Nb) (102,103). Secondary phases that

may be present include: carbides ($M_{23}C_6$, M_7C_3 , M_6C and MC), nitrides (MN), Carbonitrides ($M CN$), and Borides (M_3B_2), as well as Lavés phase (M_2Ti) and δ phase (Ni_3Nb). A double aging treatment that produces different precipitates may be employed when more than one phase is capable of precipitating from the alloy matrix. The aging temperature determines not only the type but also the size distribution of the precipitate (102,103).

1.6.3. Heat Treatment of Intermetallic Alloys

The phase constituent of intermetallic alloys is not as complex as that of superalloys. Their room temperature structure typically contains a matrix plus one or two secondary phases. For example, in the vicinity of stoichiometric TiAl, the matrix is ordered tetragonal γ phase (TiAl) and the secondary phase is ordered hexagonal α_2 phase (Ti_3Al) and sometimes disordered body centered cubic β phase. The microstructures of two-phase γ alloys can be classified into single phase, duplex structure, fully-transformed, super solvus, sub-transus and dual-phase equiaxed (69). The single phase microstructure consists of predominantly equiaxed γ grains with no obvious second phase. Fully-transformed microstructures have grains and/or colonies containing alternate layers of γ and α_2 plates of a defined crystallographic orientation relationship. The duplex microstructure is a fine mixture of equiaxed γ grains and lamellar grains. Other structures are not very common in the final state. Formation of these microstructures depends directly on processing and/or heat-treatment conditions (63,64,104-108).

HIP treatment is applied as an effective method for eliminating microporosities formed during the casting process. A two-step heat treatment is required to produce the two-phase TiAl-based alloys. The first step consists of solutioning or recrystallizing material in α or $\alpha+\gamma$ phase field. The α -transus temperature for 48-2-2 alloy is about 1380°C. Thus, solution treatment for this material conducted at

1300°C (in the $\alpha+\gamma$ region) and 1400°C (in the α phase region) will produce the duplex and fully-transformed microstructures, respectively. This heat-treatment controls the volume fraction of lamellar grains as well as the size of the constituents. It appears that maximum ductility is achieved within about 10 vol.% of α_2 phase and that if the amount of α_2 exceeds about 20 vol.%, the alloy embrittles (1). This means that the microstructure (phase volume fraction, grain size and morphology) has to be controlled very precisely if consistent properties are to be achieved. The second heat treatment in the $\alpha_2+\gamma$ phase is meant to stabilize the microstructure and phase composition at a temperature lower than eutectoid point (about 1125 °C).

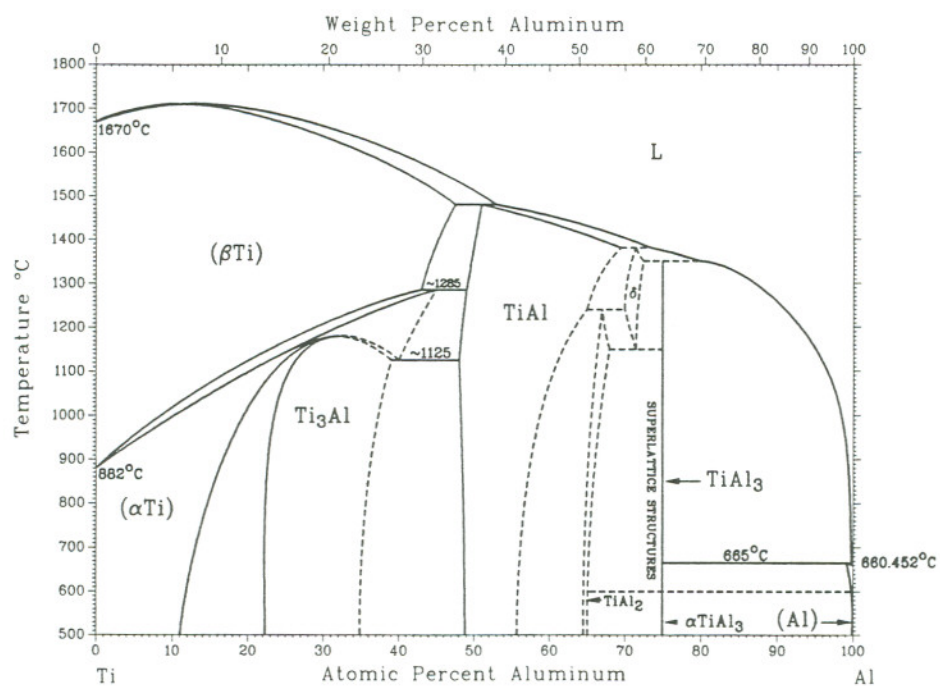


Figure 1.1 Ti-Al Binary phase diagram (56)

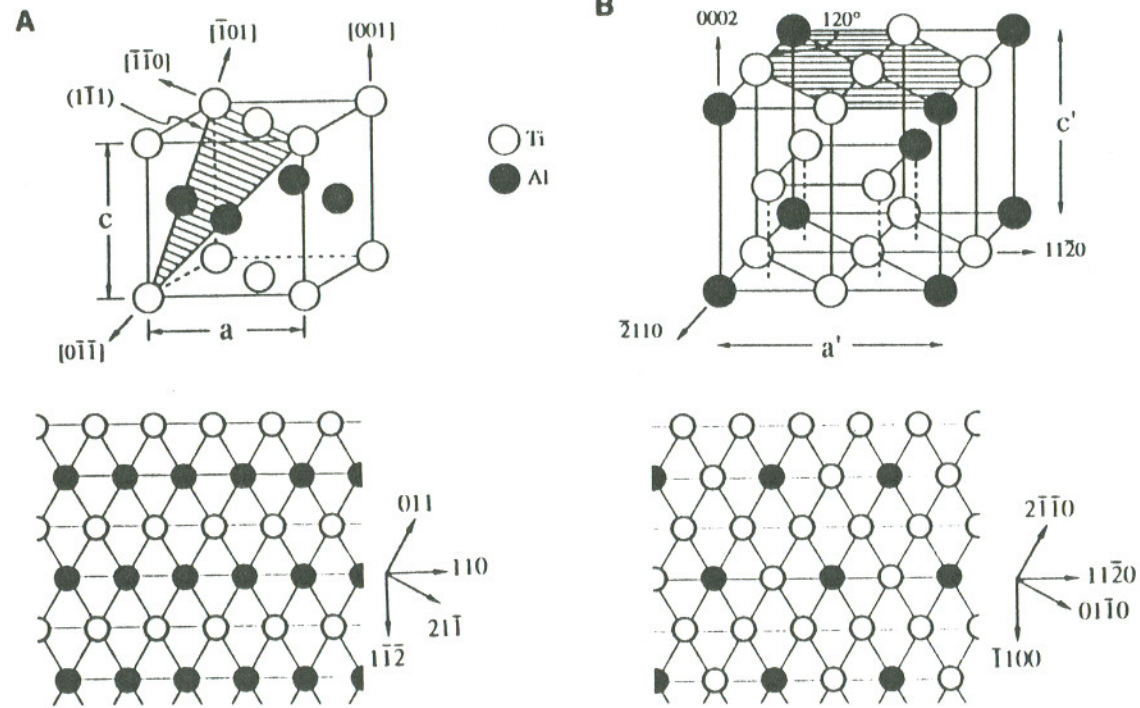


Figure 1.2 Atomic arrangement in the lattices and the close-packed planes of $L1_0$ γ -TiAl structure (a) and $D0_{19}$ α_2 -Ti₃Al structure (b) in the stoichiometric compositions (57)

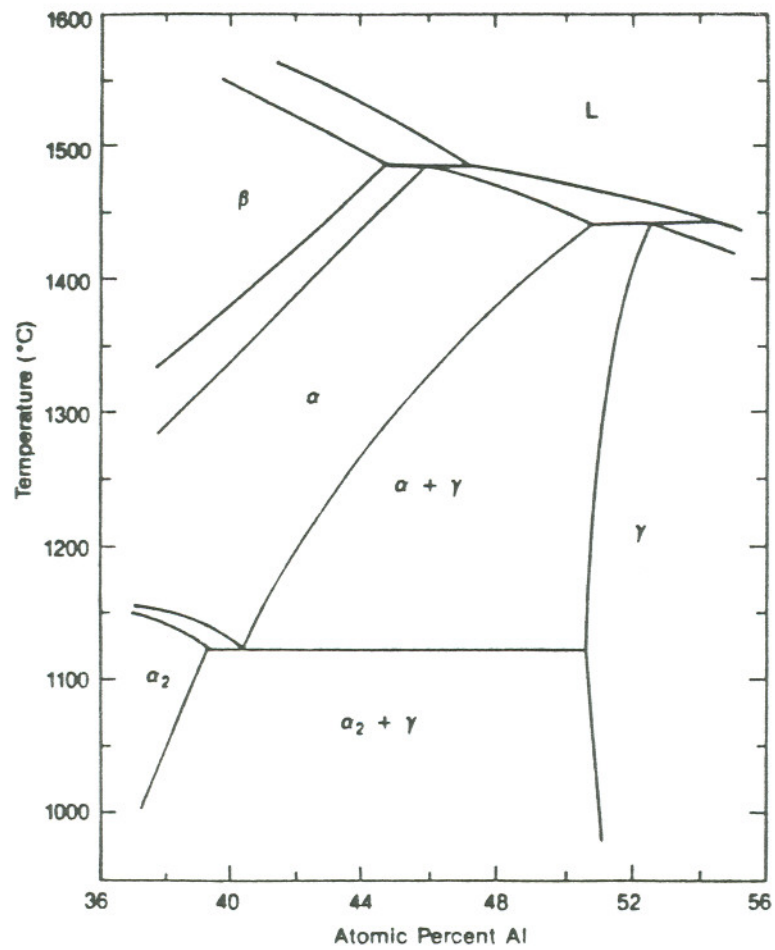


Figure 1.3 A partial Ti-Al phase diagram near the stoichiometric TiAl composition (69)

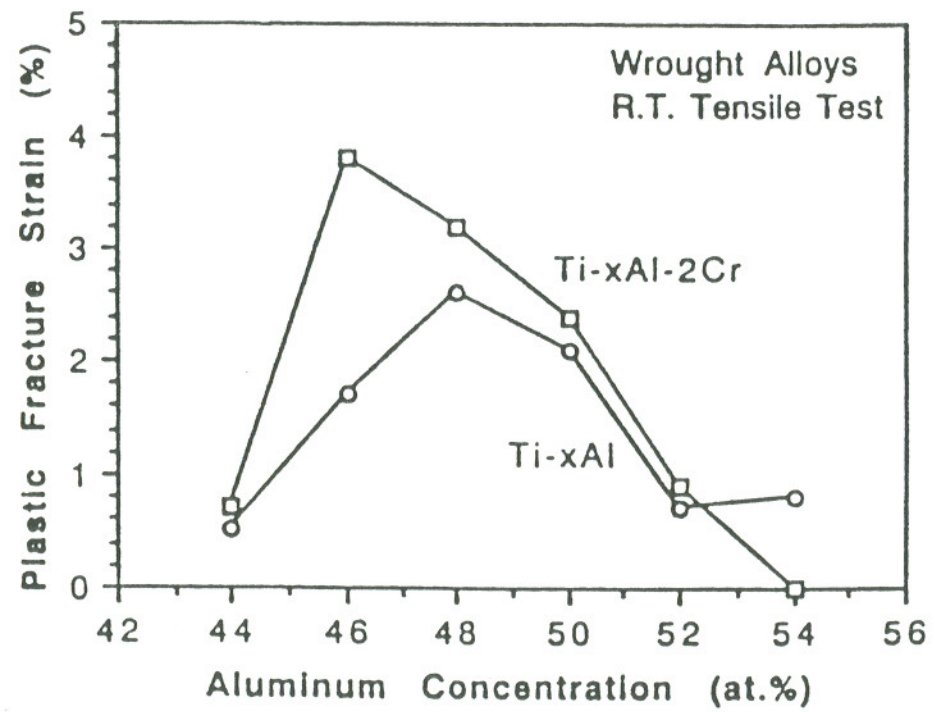


Figure 1.4 The effect of Cr addition on the plasticity of wrought γ -base alloys (69)

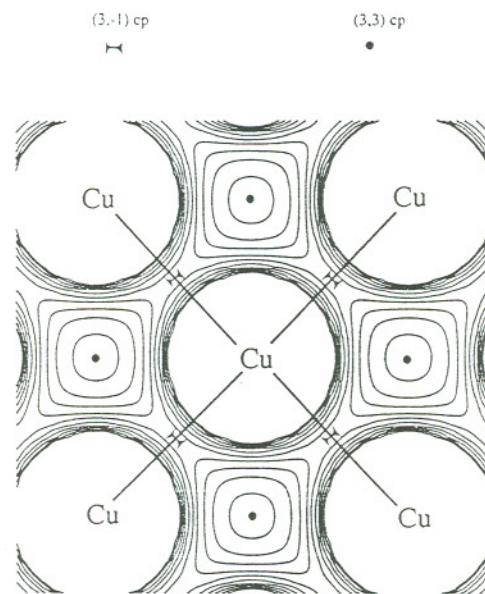


Figure 1.5 Charge density in the (100) plane of copper (68)

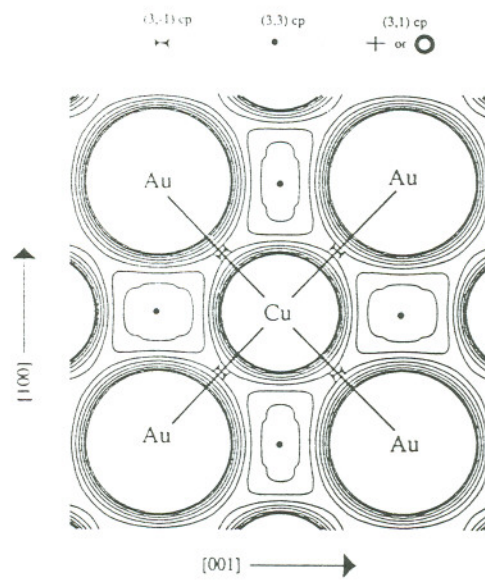


Figure 1.6 Charge density in the (100) plane of CuAu intermetallic alloy (68)

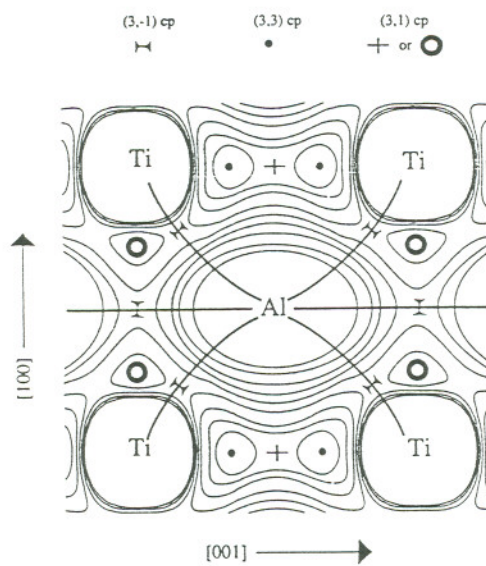


Figure 1.7 Charge density in the (100) plane of TiAl intermetallic alloy (68)

CHAPTER 2

MATERIALS AND EXPERIMENTS

2.1. Materials

2.1.1. Superalloy X

Compared with the commonly used Inconel 718, Superalloy X is higher in Ni and Co content, and lower in Fe. It utilizes γ'' as the principal strengthening phase instead of γ' which is the common strengthening phase for most superalloys. By controlling the solidification process and post-cast treatments (HIP, solution and age), different microstructures (grain sizes and distribution of precipitates) were obtained for the material. Two groups of samples having different microstructure, namely 01C and 04F, have been used in the tests.

In addition to the FCC γ matrix, there are three principal strengthening precipitate phases: gamma prime (γ'), gamma double prime (γ'') and delta (δ) phases.

The geometries for γ' phase, γ'' phase and δ phase are shown in the Figures 2.1 to 2.3, respectively. Arranging the above three phases in the order of decreasing size will produce a sequence of δ , γ'' and γ' . The δ phase is so large that it can be clearly observed under low magnification optical microscopy.

The microstructures of the heat-treated samples of the two groups are shown in Figures 2.4 and 2.5, respectively. Group 01C samples, which are also called coarse grain samples, show a microstructure of very large grain size and a non-uniform

distribution of precipitates (ppts). During solidification the matrix has a tendency to reject elements with large atomic size such as Nb to the inter-dendrite area. This causes a non-uniform distribution of these elements, rich in the inter-dendrite region and poor within the dendrite. The extent of such segregation is influenced by the cooling rate: the lower the cooling rate, the more extensive the segregation. As a result of the elemental segregation, the precipitates formed in the cooling process are also non-uniformly distributed. As it can be seen from Figure 2.4, the inter-dendrite regions are rich in ppts and most of the ppts are δ plates, and dendrites rarely contain ppts. The as-cast structure has been partially inherited in the heat treated samples. As will be discussed later, such an inhomogeneous structure plays a dominant role in influencing the high temperature mechanical properties of the material.

In the 04F group (fine grain) samples, due to small grain sizes and the post-cast heat-treatment, precipitate distribution is much more uniform than that in coarse grain samples. But considering a single grain, the precipitate distribution, especially that of the δ plates, is still non-uniform from grain boundaries to the interior of the grain. On the grain boundaries and the layers close to the grain boundaries δ precipitates are much more dense than that on the grain interior, as shown in Figure 2.5. Near this δ -rich layer is an area where most ppts are γ'' and γ' . There is nearly a ppt-free field in the centers of the grains (shown as white spots in Figure 2.5)

The general mechanical properties of Superalloy X are listed in Table 2.1.

Table 2.1 Room and High Temperature Properties of Superalloy X

Material Properties	Coarse grain		Fine grain	
	Temperature		Temperature	
	Room	1200°F	Room	1200°F
Young's modulus [ksi] (GPa)	32000 (220.6)	26100 (180.0)	32000 (220.6)	26100 (180.0)
Yield strength [ksi] (MPa)	118 (814)	100 (689)	151 (1041)	115 (793)
Ultimate tensile strength [ksi] (MPa)	158 (1089)	155-160 (1069- 1103)	200 (1379)	160-170 (1103- 1172)
Elongation at fracture [% ,min]	8	11	6	5
Reduction in area at fracture [% ,min]	--	15	10	10

2.1.2. 48-2-2 TiAl Alloy

The γ -based intermetallic alloy investigated in this study is the so called "48-2-2 alloy" which contains 48 at. % Al, 2 at. % Nb and 2 at. % Cr, and the remainder is Ti. Depending on the solidification rate and post-cast treatment procedures, samples tested in the study are different in some metallurgical factors such as grain size,

lamellar structure volume fraction, α_2 phase volume fraction, and so on. One common feature among them is that all samples have a so called duplex structure, as shown in Figure 2.6. This structure contains two components: equiaxed γ grains and lamellar structure which is formed by the alternative packing of γ layers and α_2 layers. In the lamellar structure, both γ and α_2 phases are in the plate shape and in general the γ plate is wider than α_2 plate, as shown in Figure 2.7. Table 2.2 lists the general tensile properties for Ti-Al alloys.

Table 2.2 Representative Room Temperature Physical and Mechanical Properties of Ti-Al Intermetallics (107)

Alloy Base	Elastic Modulus (GPa)	Yield Strength (MPa)	Yield Strain (%)	Fracture Strain (%)	Fracture Toughness (MPa \sqrt{m})
Ti ₃ Al	100	500-1050	0.5-1.0	0-4	12-21
TiAl	175	400-600	0.2-0.4	0.4-5	10-30

2.2. Experiments

To relate the mechanical properties to the microstructures, two groups of tests were conducted on tested materials: mechanical tests which included both ambient temperature tensile test for 48-2-2 material and elevated temperature tests for Superalloy X, and microanalysis using transmission electron microscopy (TEM), scanning electron microscopy (SEM) and optical microscopy.

2.2.1. Tensile Test

Tensile tests were performed to determine the room temperature ductility and fracture strength of the specimens. The test specimens were produced by center-less grinding the precisely cast bars. The samples were round, smooth specimens with a diameter of 5.3mm and have a gage length of 25.4mm, as shown in Figure 2.8. The tests were done on an Instron Testing Machine, under position control (stroke control) with a ramp rate of 0.0025 mm/sec. A 12.7mm gage length extensometer was used to measure the specimen displacements during loading.

2.2.2. Creep Test

Cylindrical specimens of 6.25mm (0.25in) diameter and 25mm (1in) gage length were tested at 650°C (1200°F) in air under constant loads using dead weight creep machines. Test standards and procedures were in accordance with American Society for Testing and Materials (ASTM) specification E-139 (108). The specimens were subjected to stress levels ranging from 586 MPa (85ksi) to 793 MPa (115ksi). Continuous measurement of strain in the gage section was made to characterize the full creep curve. All tests were conducted during 100h test performance. The strain/time creep data from specimens tested at various stress levels were collected.

2.2.3. Creep Crack Growth Test

2.2.3.1. Crack Length Measurement

Accurate measurements of crack extension are important in subcritical crack growth studies because rates of crack extension characterized in laboratory specimens are used to predict the cracking behavior of structures in the field.

There are several methods (109) of measuring crack growth at elevated temperatures.

Optical methods (e.g. use of a travelling optical microscope) give only the crack length on the surface and a reliable indication of average crack length can only be obtained if the crack front is relatively straight through the thickness of the specimen. A way of encouraging straight fronted crack is to increase through thickness constraint by introducing side grooves. In addition, surface oxidation can obscure the crack due to the loss of contrast with a dull background.

The compliance technique is an alternative method of monitoring crack growth. The routine for obtaining crack growth by the elastic compliance technique is to make periodic unloading and reloading of the sample at suitable time intervals to obtain the change in compliance from which the crack extension may be estimated. For constant load studies, a periodic partial unload may cause a transient response due to the regeneration of an elastic stress at the crack tip. If this happens, the subsequent crack propagation rate may not be characteristic of that for steady loading as stress redistribution by creep may be prevented.

Electrical potential is one of the methods by which crack extension during a test can be monitored continuously (110). At temperatures in creep regime for metals, this technique continues to be reliable while other techniques such as elastic compliance no longer apply. The electrical potential technique detects the changes in the electrical potential field in the vicinity of the crack, as crack extension occurs. A calibration curve is required to convert the measured changes in potential to changes in crack area in a specimen of given shape and size. By dividing the change in crack area with specimen thickness, a through-thickness average crack extension can be obtained. The measurement of crack extension is thus automatically adjusted for crack tunneling which makes the technique especially suitable for studying cracking

due to fatigue, stress corrosion, or creep loading. Its application, however, is totally dependent on an accurate calibration relating output voltage to crack length.

In the present study cracks were monitored using all of the above techniques.

2.2.3.2. Testing Procedure

The tapered double cantilever beam specimen, as shown in Figure 2.9, has been designed specifically for crack extension studies. By properly adjusting the degree of taper, the derivative of EBu/P (where B - specimen thickness, E - tensile modulus of elasticity, u - deflection, P - load) with respect to the crack length, a , is a constant in this range. This in turn implies that for a constant specimen load, a constant crack extension force, K , or equivalently a constant energy release rate, G , is reached (111). There are several methods which can be used to determine the stress intensity factor in the tapered specimen. This includes: numerical methods such as finite element methods, the compliance calibration method when the energy release rate and the stress intensity factor are determined from compliance curves, and photoelastic methods. In this study, the compliance calibration method was used.

Using the values of compliance, the crack extension force is calculated from the following equation (109):

$$K = P \left[\frac{E}{2B} \frac{dC}{da} \right]^{\frac{1}{2}} \quad (2.1)$$

where C is compliance (usually expressed as a function of the crack length a).

The same equation can also be written as:

$$K = \frac{P}{B} \left[\frac{1}{2} \frac{d\left(\frac{EBu}{P}\right)}{da} \right]^{\frac{1}{2}} \quad (2.2)$$

and

$$K = \frac{P}{B} \left[\frac{1}{2W} \frac{d\left(\frac{EBu}{P}\right)}{d\left(\frac{a}{W}\right)} \right]^{\frac{1}{2}} \quad (2.3)$$

where W is the length of tapered area.

In the present study, the compliance of the double cantilever beam specimen and the functional relationship between compliance and crack length were determined experimentally. Artificial cracks, like sawcuts, were utilized not only to accelerate the calibration tests but also to define the crack length in an unambiguous manner.

In performing the calibration test with artificial cracks, the notch was formed by a cut using an abrasive wheel. Next, a compliance reading was taken and the procedure was repeated until the desired range of crack lengths was covered. It is always convenient to determine an equation of the compliance curve by fitting the experimental data to a general polynomial:

$$C = D_1 + D_2 a + D_3 a^2 + D_4 a^3 + \dots \quad (2.4)$$

In this particular case the experimental results can be described as:

$$C = -0.39241 \times 10^{-5} + 1.958331 \times 10^{-5} a \quad (2.5)$$

However, a better fit of the experimental results can be obtained by employing the following expression:

$$C = 0.305018 \times 10^{-5} + 0.5562125 \times 10^{-5} a + 0.63809426 \times 10^{-5} a^2 \quad (2.6)$$

This indicates that, for this specimen geometry, constant K values can be assumed only for short cracks. For this reason, crack extension not longer than 10.2mm (which corresponds to $a/W \leq 0.5$) was taken into account in order to ensure an approximate constancy of K value, when the crack growth rate was estimated.

A number of constant K specimens were tested at various applied steady loads to determine the dependence of crack growth rate on the stress intensity at the crack tip. The temperature variation on the surface of the specimen along the crack plane was found to be within 5 °C. The potential drop technique was used to estimate the crack length during testing. In addition, the specimen compliance was measured by means of a displacement transducer. The crack growth process was also monitored using an optical traveling microscope. The stress intensity factor was calculated from equation (2.2).

2.2.4. High Temperature Low Cycle Fatigue Tests

Compact tension specimens shown in Figure 2.10 (110) were used in the present investigation. A two-stage process involving precracking and load shedding prior to elevated-temperature fatigue testing was employed. The initial crack length (slot plus precrack) was approximately equal to 27mm for each specimen.

The fatigue crack growth tests were performed at 1200°F in load controlled conditions with a frequency of 0.33Hz. The wave form was sinusoidal with a stress ratio of 0.05. For the low cycle fatigue with hold time, a hold period of 90 seconds was imposed at the maximum load (P_{max}). The tests were carried out in air using the Instron testing machine. It should be noted that in these conditions both creep and oxidation mechanisms are operative.

During testing, the crack growth was monitored using a travelling optical microscope and potential drop technique was employed to measure the crack lengths. Calculations of both the fatigue crack propagation rate, da/dN , and the stress intensity factor K were in accordance with standard test methods for measurement of fatigue crack growth rates (ASTM designation: E-647) (112).

2.2.5. TEM and SEM Examinations

TEM specimens with 0.2mm thickness were cut from the as received and tested (perpendicular to the loading axis) samples for both Superalloy X and TiAl alloy. These were then ground on #600 SiC papers and disks with 3mm diameter were punched out of the thinned specimens. They were electropolished in a jet electropolishing bath of 5% perchloric acid and 95% methanol in the temperature range of -40 to -30 °C. TEM examinations were done with a HITACHI-800 analytical electron microscope with a double tilt sample stage and at 200 KV

acceleration voltage. Fracture surfaces were examined under Zeiss DSM-960 scanning electron microscope. Under some cases, Back Scattered Image technique was also used for the chemical composition related studies.



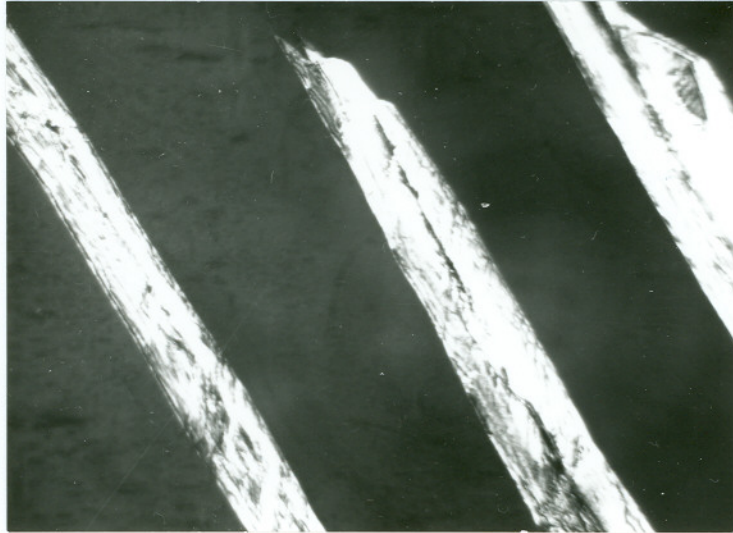
0.3 μm

Figure 2.1 Morphology of γ' phase in Superalloy X, large precipitates on the boundary are γ''



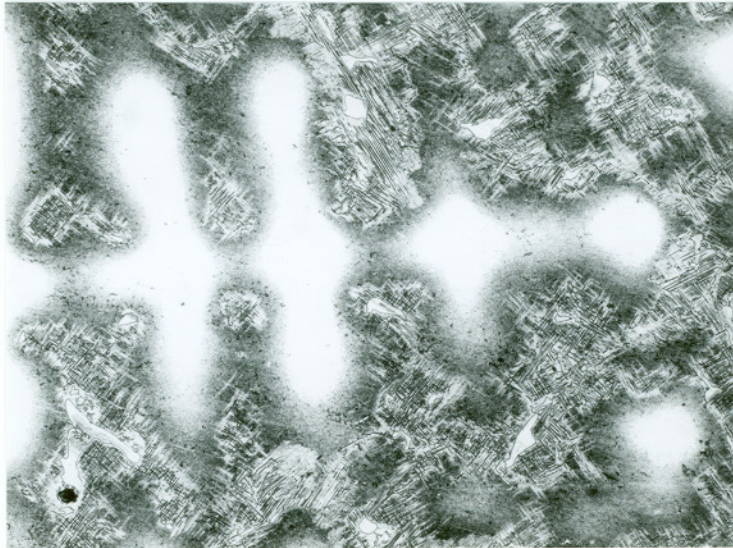
0.9 μm

Figure 2.2 Morphology of γ'' phase in Superalloy X



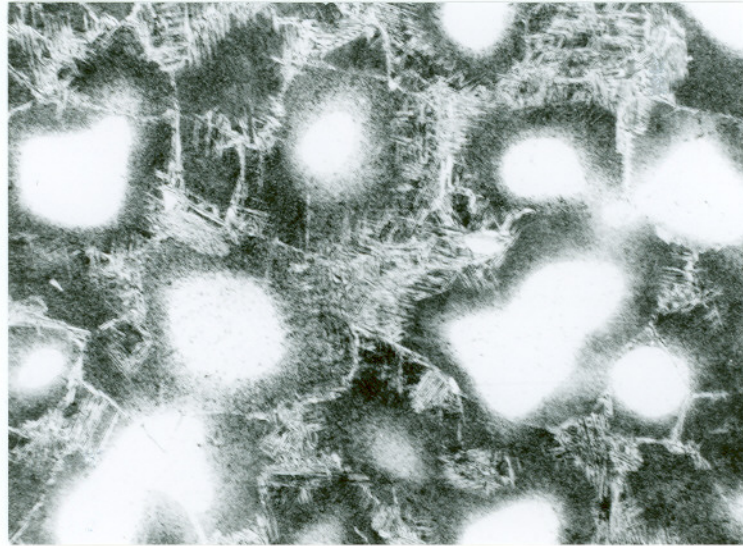
0.9 μm

Figure 2.3 Morphology of δ phase in Superalloy X



150 μm

Figure 2.4 Microstructure of coarse grain sample



150 μm

Figure 2.5 Microstructure of fine grain sample



75 μm

Figure 2.6 Microstructure of 48-2-2 TiAl alloy

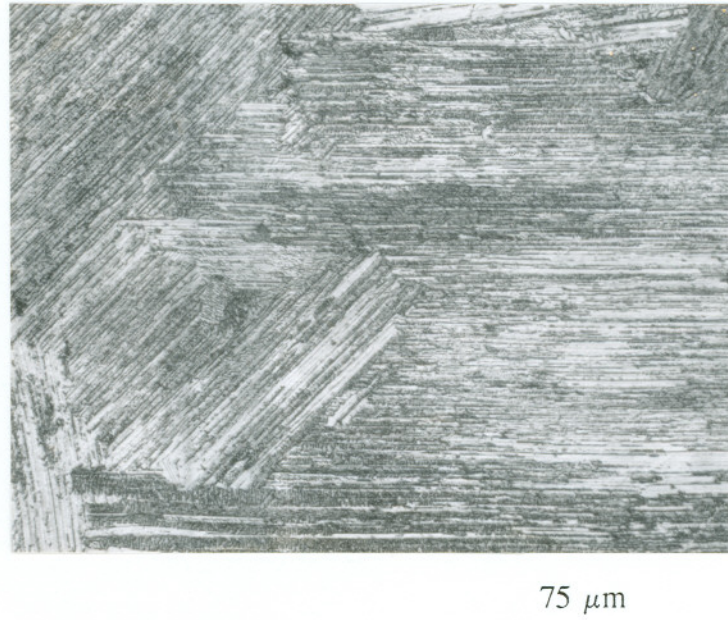


Figure 2.7 Lamellar structure in 48-2-2 TiAl alloy

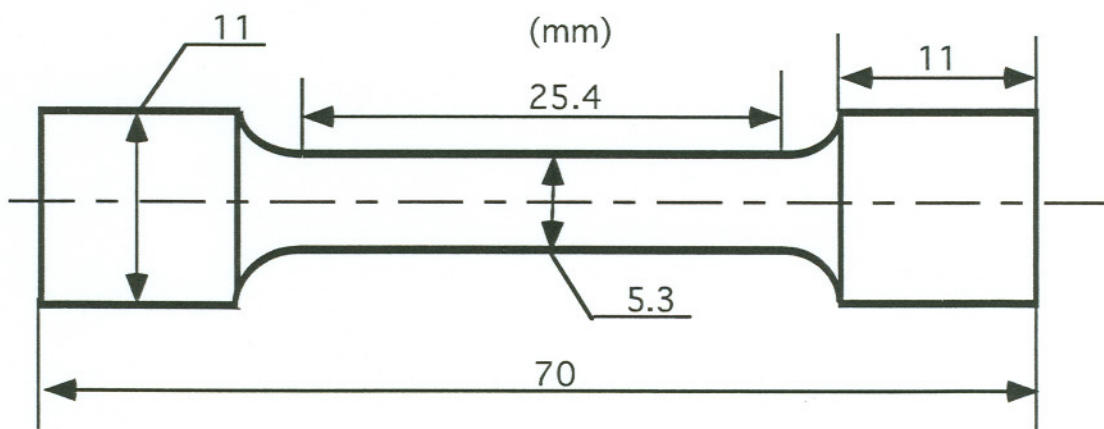


Figure 2.8 Specimen for tensile test

ALL DIMENSIONS IN mm

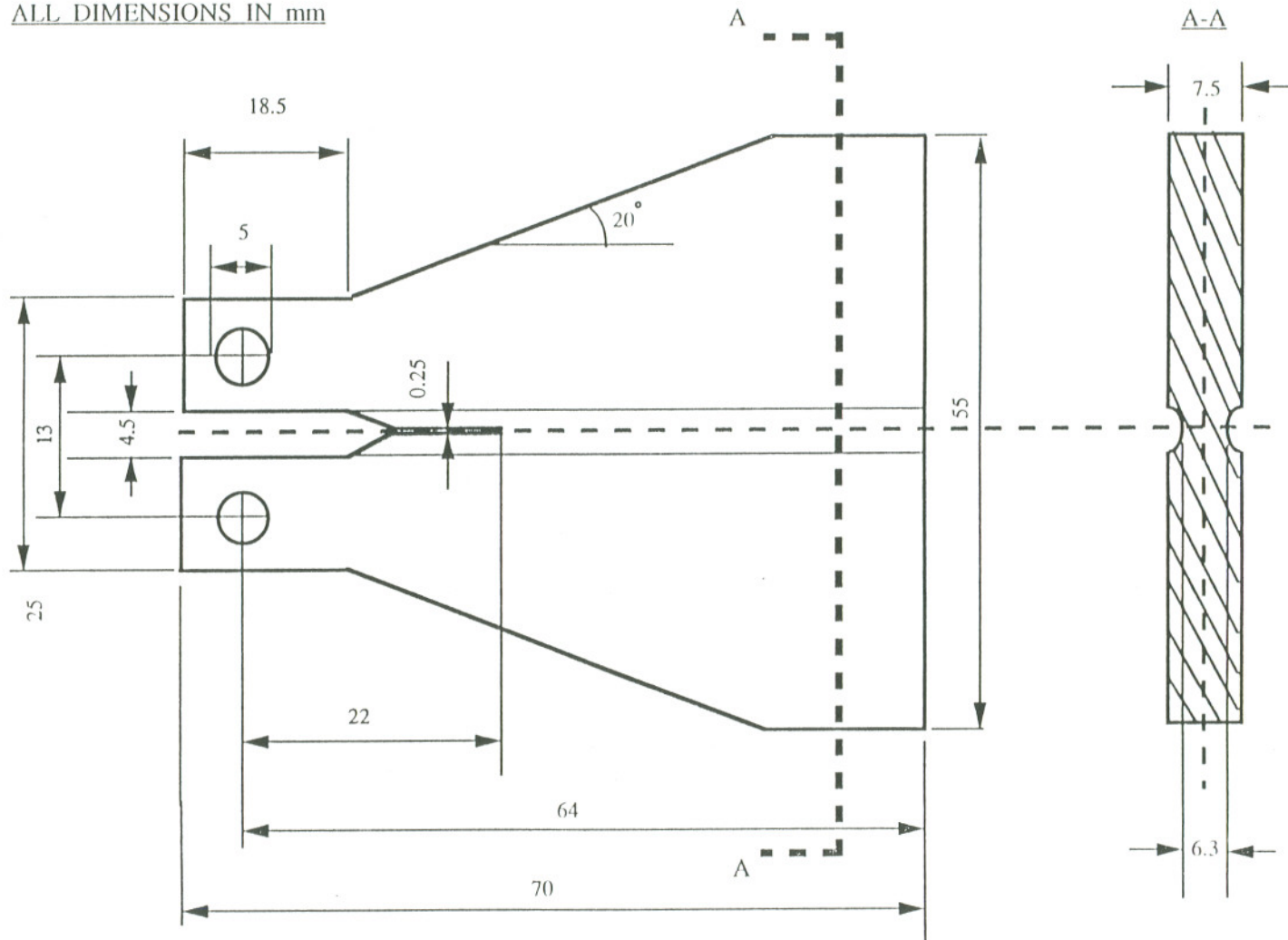


Figure 2.9 Tapered double cantilever beam specimen

All dimensions in mm

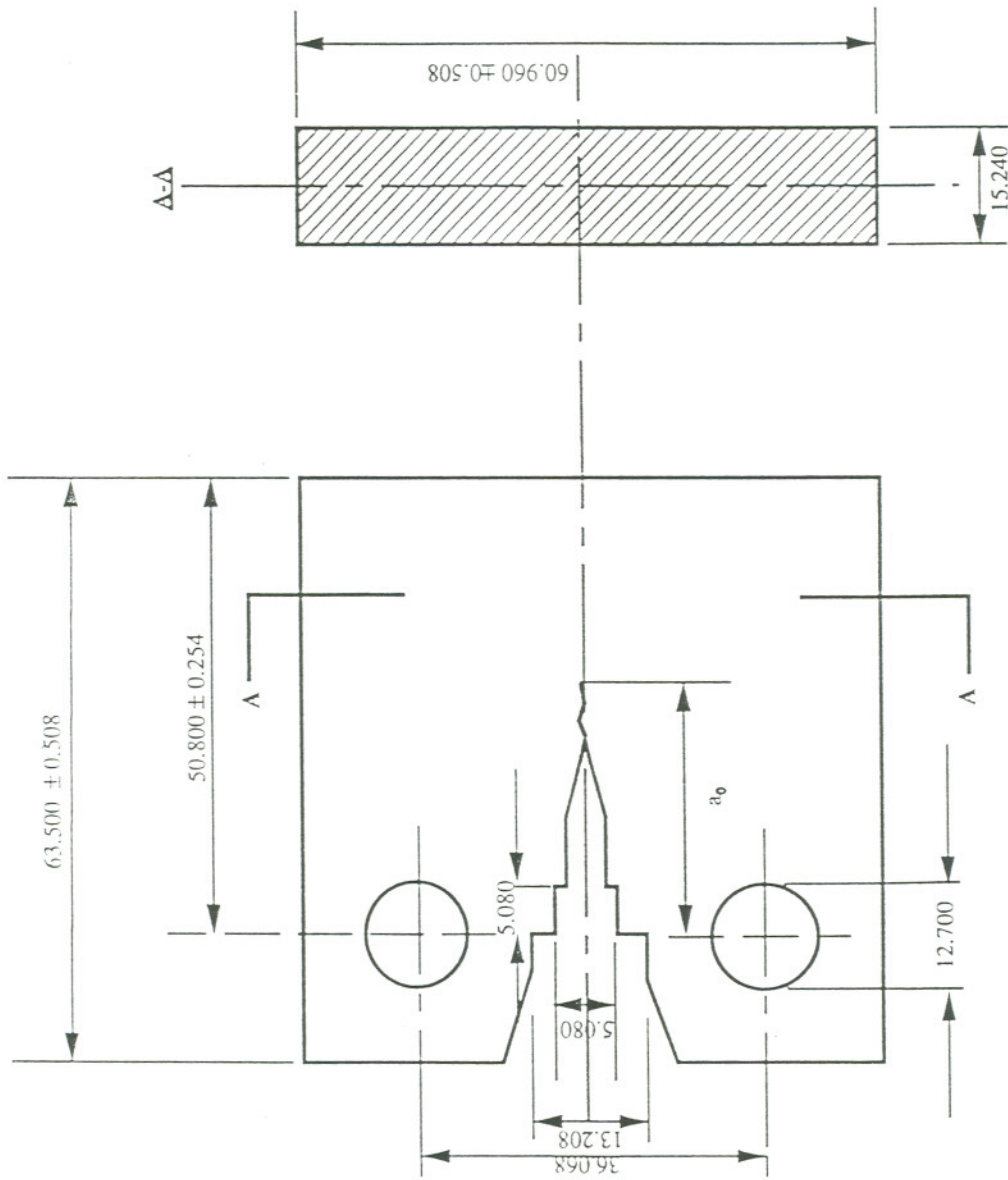


Figure 2.10 Compact tension specimen

CHAPTER 3

RESULTS AND DISCUSSION (SUPERALLOY X)

3.1. Creep Test

3.1.1. Creep Behavior of Superalloy X as a Function of Grain Size and Applied Stress

The specimens were subjected to stress levels ranging from 586MPa (85ksi) to 793MPa (115ksi) - Table 3.1. The creep behavior of Superalloy X depends on the grain size and stress level. The creep curves of the fine grain material exhibit mostly primary and secondary creep deformation for all stress levels. For the coarse grain material, in addition to the primary and secondary creep regions, the tertiary creep deformation can be seen for specimens tested at 655MPa (95ksi), 690MPa (100ksi) and 724MPa (105ksi). The fine grain material specimen tested at 793MPa (115ksi) failed by creep rupture after 20.3h. The creep strain at failure was 2.7%. The coarse grain material specimen tested at 724MPa (105ksi) failed by creep rupture after 69.1h. The creep strain at failure was 6.4%.

There was a significant difference in creep deformation between the fine grain material and the coarse grain material for the same creep time (Table 3.1). The stress-strain diagram at the constant creep time of 50h is shown in Figure 3.1. For the same load level, coarse grain material has higher creep deformation than fine grain material. An inverse trend is obtained when normalized stresses, σ/Y_S (where Y_S = yield strength at 650°C) are considered (Table 3.1). The fine grain material has higher creep deformation than the coarse grain material for the same σ/Y_S ratio

(Figures 3.2a and 3.2b). This indicates a better relative resistance to creep with respect to the yield strength for the coarse grain material.

3.1.2. Creep Rate

It can be seen from the creep data that the creep rates appear to increase with increasing stress level and grain size. Creep is traditionally divided into three stages, though not all are always present. The first stage is called primary creep, the second is called steady-state or secondary creep, and the third is called tertiary creep. Usually the increase in the creep rate in the tertiary stage is due to an increase in stress as the area is reduced either by thinning down of the specimen (necking) or by internal fracture or void formation. When secondary creep dominates, all other strain rate terms are negligible. The following equation best fits the experimental data for uniaxial tensile creep conditions:

$$\dot{\epsilon} = k\sigma^n \quad (3.1)$$

where $\dot{\epsilon}$ is creep rate, σ is applied stress, k and n are material constants.

For the steady-state creep rate (secondary creep only) equation 3.1 (the Norton-Bailey uniaxial creep law) was used (113) to describe the relationship between stress and creep rate. The creep data for the fine and coarse grain materials were fitted to the following equation to obtain the regression constants k and n :

$$\log \dot{\epsilon} = C + n \log \sigma \quad (3.2)$$

It was found that the secondary creep behavior of the fine grain and coarse grain materials can be described by the following expressions:

$$\dot{\epsilon} = (1.3 \times 10^{-47}) \sigma^{13.8} \quad (3.3)$$

$$\dot{\epsilon} = (4.2 \times 10^{-63}) \sigma^{19.4} \quad (3.4)$$

respectively.

It can be seen from Figure 3.3 that the creep rates plotted versus stresses in logarithmic system for both the fine and coarse grain materials are straight lines. A small number of test specimens does not allow the calculation of very accurate values of coefficients k and n . However, the different slopes of the straight lines indicates the difference in the creep deformation behavior of these two materials. This is consistent with visual observations of the damage zone (small amount of creep deformation and rupture without reduction in area for the fine grain material, and larger creep deformation and necking for the coarse grain material).

Table 3.1 Creep test results for both fine and coarse grain materials

	No	σ [MPa]	σ/YS	ϵ_{50h} [%]	$\dot{\epsilon}$ [1/s]
Fine grain	1	586.2	0.74	0.155	3.927E-9
	2	655.2	0.83	0.344	6.197E-9
	3	689.7	0.87	0.471	1.571E-8
	4	724.1	0.91	1.026	2.851E-8
	5	793.1	1.00	-----	2.644E-7
Coarse grain	1	586.2	0.85	0.134	2.207E-9
	2	620.7	0.90	0.547	7.326E-9
	3	655.2	0.95	0.517	1.672E-8
	4	689.7	1.00	1.023	3.621E-8
	5	724.1	1.05	4.566	1.686E-7

3.1.3. Microstructural Effects on Creep Behavior

As indicated by the test results, the coarse grain samples have lower creep resistance than fine grain samples under the same load level. Plastic deformation in the classical creep process occurs mainly because of grain boundary sliding and hence the creep strength of a material is essentially dependent on the strength of grain boundaries. Although, slip within the grains can also provide some contribution to the total plastic deformation, especially at the primary stage, grain boundary sliding usually dominates the whole creep process. The ratio of plastic deformation produced by grain boundary sliding to that by the slip within grains is a function of the temperature, the load level and the grain size. It increases with increase in temperature, decrease in stress level and grain size.

In the coarse grain sample, the fraction of grain boundaries is very small. Grain boundaries can not provide enough plastic deformation required by the corresponding loading conditions (temperature, stress level and time). On the other hand, creep resistance of the intra-dendrite area which is nearly free of precipitates is lower than that of inter-dendrite area where there are dense precipitates. So the plastic deformation occurs initially in the intra-dendrite area since there are fewer obstacles to the motion of dislocations in that region. Such motion will be arrested when the dislocations encounter large size precipitates like δ plates. This will cause a local stress concentration on the interfaces between precipitates and the matrix. From a global viewpoint, the deformation continuity requires the surrounding inter-dendrite area to participate in deformation. However, resistance to deformation is much stronger in those areas than that in the intra-dendrite region. As a result of these two opposing processes, there will be a stress concentration in the transition layer. Furthermore, the formation of dense, large size δ plates has already decreased the bonding strength of the transition layer between inter and intra dendrite areas. Under the influence of these factors, the occurrence of creep deformation is limited essentially to the intra-dendrite regions and cracks initiate in the transition layer. Figure 3.4 also shows that the cracks select transition layers as their growth paths.

Another deformation configuration is the persistent slip bands which are composed of heavily tangled dislocations, as shown in Figure 3.5. Figure 3.5 also shows that the band is a precipitate-free zone. However, around the band there are a number of γ' precipitates which are surrounded by dislocations. Although the exact mechanism of the formation for such band in the precipitate-rich area is not clear, there should be some sort of interaction between dislocations and precipitates. It can be inferred that both the precipitate distribution state and their size play an important role in determining the creep life of the material and hence care should be exercised in selecting a suitable heat treatment procedure in order to achieve the best possible results.

In the fine grain samples, the distribution of precipitates is much more uniform than that of the coarse grain samples and also the fraction of grain boundaries is much higher. This means that there are more sites available for grain boundary sliding. According to the traditional creep theory, in such case, voids will form at first on the grain boundaries and, later on, will coalesce to form a microcrack. However, there are δ -rich areas around grain boundaries and these areas have a higher stress concentration and hence lower bond strength. These are the weakest spots and are selected as the crack initiation points. Figure 3.6 exemplifies this type of crack initiation. Since cracks always propagate along the lowest energy path, they are also selected as preferential crack propagating routes.

3.2. Creep Crack Growth Test (Constant K Test)

3.2.1. Parameters Describing the Creep Crack Growth Behavior

The most commonly used parameters for characterizing the creep crack growth rate \dot{a} are the stress intensity factor K , the contour integral C^* and the net section stress σ_n or reference stress σ_{ref} across the uncracked ligament. Relations that have been proposed are usually of the form:

$$\dot{a} = AK^m \quad (3.5)$$

$$\dot{a} = D\sigma_{ref}^p \quad (3.6)$$

and

$$\dot{a} = HC^* \sigma^n \quad (3.7)$$

where A, D, H, m, p and ϕ are material constants.

Since σ_n and σ_{ref} do not describe crack tip quantities, they should not be expected to correlate with crack growth rate.

The levels of creep at which creep crack growth can occur include the small-scale creep region, the transition creep region and the extensive creep region. The C^* (114) parameter is used for extensive creep (or steady-state) conditions when $t \geq t_T$ (where t_T - transition time between small-scale creep and extensive creep). The size of the small-scale zone can be defined as (115):

$$r_\infty = \frac{1}{6\pi} \left(\frac{K}{\sigma_e} \right)^2 \quad (3.8)$$

where σ_e is elastic limit.

In case of "creep brittle" condition, the stress intensity factor K provides a fair correlation with the test data. For "creep brittle" circumstances, where little creep deformation accompanies fracture, the stress distribution will remain virtually unaltered by creep and K will continue to characterize the stress around the crack. This correlation has been observed in laboratory tests on nickel-based alloys that are susceptible to oxidation. Investigations of the commercial nickel-based superalloy 718 have revealed that in the small-scale creep region the stress intensity factor is a proper mechanical factor to describe the creep crack behavior. A threshold stress intensity factor, K_{th} , for small-scale creep crack growth has been proposed. A creep crack model represented by the effective driving force, G_e , has been suggested in the literature (115), of the form:

$$\dot{a} \sim cG_e$$

where $G_e = (K^2 - K_{th}^2)/E$, and c is a material constant.

3.2.2. Creep Crack Growth in the Fine Grain Material

Using the experimental set-up, a crack was initiated from the notch tip (without any fatigue precrack) at 650°C in air. All the data were registered by a computer using the "Solus" system. Using the calibration curves, the potential drop and displacement versus time curves can be converted for changes of crack length with time and subsequently the creep crack rate can be estimated (Table 3.2).

The creep crack propagation rate, \dot{a} , versus the stress intensity factor, K , is shown in Figure 3.7. The relationship between \dot{a} and K for higher values of K ($K \geq 43.6\text{MPa}\sqrt{\text{m}}$) is given by the following expression:

$$\dot{a} = 2.08 \times 10^{-11} K^{2.72} \quad (3.9)$$

From the experimental results shown in Figure 3.7 it can be seen that, similar to the fatigue crack propagation, there appears a threshold stress intensity factor, K_{th} , below which the creep cracks will not initiate and grow. Its value is lower than $26\text{MPa}\sqrt{\text{m}}$. Figure 3.8 shows crack incubation time as a function of the stress intensity factor. It should be noted that the incubation time substantially increases when the stress intensity factor is equal to $24.5\text{MPa}\sqrt{\text{m}}$. This phenomenon confirms the creep crack growth threshold behavior. For further calculations, K_{th} value was assumed to be equal to $24.4\text{MPa}\sqrt{\text{m}}$.

Because of the existence of a threshold value, the creep crack growth rate

should be controlled by an effective driving force G_e . In that case the creep crack growth law can be given by the following expression (Figure 3.9):

$$\dot{a} = 1.12 \times 10^{-10} (K^2 - K_{th}^2)^{1.156} \quad (3.10)$$

The exponent value equal to 1.156 is close to the value of 1.025 obtained for Alloy 718 tested at 650°C under similar creep crack growth conditions (115).

The "creep brittle" behavior of the fine grain material is evident:

- there was no evidence of extensive creep zone near the crack tip;
- the entire length of the specimen arms remained straight after the test;
- there exists a threshold stress intensity factor which is a characteristic of small-scale creep conditions;
- there is good agreement with the creep crack growth model represented by the effective driving force.

These validate the application of the stress intensity factor K as the controlling parameter for creep crack growth. In other words, the measured compliance should be predominantly elastic. In that case it is possible to determine the crack length and subsequently the crack growth rate using the compliance-crack length calibration curve.

3.2.3. Creep Crack Growth in the Coarse Grain Material

The coarse grain material specimens were investigated in the same manner as the fine grain material specimens. For this material, attempts to initiate a crack from the notch by gradual loading up to about $87.2 \text{ MPa}\sqrt{\text{m}}$ (see Figure 3.10) in two of the specimens (TAP1 and TAP2) proved unsuccessful. Because of this behavior a fatigue

precrack of 0.5mm was introduced to the third specimen. The loading sequence for this specimen is shown in Figure 3.10 (specimen TAP3). As indicated by a decrease in potential drop signal, the crack growth was temporarily arrested and crack tip blunting occurred. It is apparent that in this case the potential drop technique is not a very sensitive measurement of short crack lengths. The final crack length is 3.8mm and it implies that the crack propagation rate is very small.

Generally, in comparison with the fine grain material, the coarse grain material is much more resistant to the creep crack growth.

Table 3.2 Creep Crack Propagation Rate in Fine Grain Samples

No	K [MPa√m]	ḁ [m/S]		Incubation time [h]
		From Potential Drop	From Displacement	
TAR	72.5	2.30E-6	1.71E-6	0.20
TAR1	41.6	5.85E-7	5.69E-7	0.47
TAR5	38.5	2.71E-7	2.37E-7	0.62
TAR4	35.6	3.48E-7	3.21E-7	0.62
TAR2	31.2	3.12E-8	4.40E-8	1.60
TAR3	24.3	1.01E-9	2.09E-9	35.00

3.2.4. Microstructural Effects on Creep Crack Propagation

Mechanical test results indicate that, as opposed to the creep test results, fine grain samples have much higher creep crack growth rates than the coarse grain samples. The interactions between cracks and microstructures were examined by checking the crack profile on the different cross sections parallel to the side surface of

samples. Figure 3.11 shows one of these crack profiles from a coarse grain sample. At point A, the primary crack stopped and two other cracks started separately from points B and C. These two branches then combined together and formed the main crack. This main crack propagated for a distance and then got arrested again at point D. Ahead of crack tip (point D), another microcrack initiated at point E. Figure 3.12 shows the same crack profile as in Figure 3.11. With selective etching, the intra-dendrite area appears white (lightly etched) and the inter-dendrite area appears dark (heavily etched). From Figure 3.12 it can be seen that:

- 1) point A where the primary crack arrested is in the intra-dendrite area;
- 2) crack re-starting point B is at the boundary of two dendrite areas; crack re-starting point C is at an inter-dendrite area;
- 3) crack tip D is arrested again in front of an intra-dendrite area;
- 4) microcrack (point E) initiated at another inter-dendrite area and has a tendency to extend along inter-dendrite region.

Here, it is reasonable to conclude that the intra-dendrite area has a higher crack propagation resistance than the inter-dendrite area. The intra-dendrite region does not have as many precipitates as the inter-dendrite region and hence its strength is lower. However, its plastic deformation accommodation capability is higher. This means that higher deformation energy is needed for a crack to propagate through such areas.

Figure 3.13 is a crack profile of the tapered fine grain sample. Figures 3.14 to 3.18 show the crack tip regions of specimens TAR1 to TAR5. All the samples were fine grained and they were tested at the same temperature with varying load levels. From their crack tip structure, some common characteristics can be derived:

- 1) ahead of the crack tip, there is a damage zone inside which one or several microcracks initiated. These microcracks may or may not combine with the

main crack later on.

- 2) these microcracks always initiate in the following forms:
 - a. debonding of δ /matrix interfaces;
 - b. interface fracture between δ -rich regions and surrounding area;
 - c. fracture of δ plates;
 - d. grain boundary cracks.

Of these situations, (a) and (b) are found to be the most common ones. Situation (d) appears only on those grain boundaries where no δ -plates exist.

- 3) most of these microcracks will be used as crack propagation paths during the following loading process. This can be verified by the fact that only a few crack branches or secondary cracks can be observed in each sample.

It is obvious that the status of δ -plates, including their size, volume fraction, distribution etc. play an important role in the creep crack propagation behavior of fine grain samples. Compared with the nearly precipitate-free interior of grains, the δ -rich area around grain boundaries has weaker creep crack growth resistance. Reasons for this phenomenon may arise from the fact that the δ -rich area has a smaller deformation accommodation ability and it is easy to build stress concentration within and/or around the area. In fine grain samples, the volume fraction of grain boundaries, which are less-resistant to crack propagation, is higher. Crack tips are always able to find such easy paths to propagate. On the other hand, in coarse grain samples, crack tips can not always find weak paths to pass through. Sometimes, they have to pass through regions where crack growth resistance is high. When such a situation appears, crack propagation may be delayed or even arrested.

Actually how and where a crack will propagate are determined by the load level, stress state, microstructure ahead of crack tip and the temperature. If the material is

completely uniform, then the crack should propagate along the horizontal direction, i.e. vertical to the maximum tensile stress. However, like most real materials, the tested samples have inhomogeneous microstructures. Ahead of the crack tip, crack propagation resistance also varies with directions. Under the constant loading conditions, if a crack can find a direction in which it takes less energy to grow than along the original horizontal direction, then the crack will deviate in that direction. If such an easy path can not be found and initiating another microcrack somewhere else within the damage zone takes less energy, then the main crack arrests its growth and another crack will initiate ahead of the main crack tip. This situation occurred in both the coarse grain and the fine grain samples.

It is found that when creep crack propagation takes place in the absence of significant creep deformation, the crack tip remains sharp and there is little opening. Also, there is often evidence of discontinuous cracking ahead of the main crack tip and consequently this leads to some ambiguity in precisely locating the crack tip. The available experimental evidence suggests that voiding and microcracking can extend up to several grains ahead of the main crack and that crack advance takes place in a series of small steps in quasi-static fashion by the progressive linking of the main crack to this damage. When extensive creep deformation accompanies cracking, crack blunting takes place and there is usually little difficulty in identifying the position of the crack tip.

The resistance to creep crack growth of the materials does not necessarily correspond to their relative uniaxial creep deformation resistance. Moreover, creep crack propagation rate does not increase with temperature in the same manner as creep strain rate. It has been found that, in Superalloy X, the cracking rate increases with decrease in material creep ductility.

Creep behavior of Superalloy X and preliminary tests of creep crack growth

indicate that, for the fine grain material, the "creep brittle" conditions (predominantly brittle fracture, lower fracture toughness and high crack growth rates under either static or cyclic loadings) can be expected. For the coarse grain material, higher fracture toughness and lower crack growth rates at the same test conditions are anticipated.

3.3. Fatigue Test

3.3.1. Low Cycle Fatigue Test With and Without Holding Time

Many components operating at elevated temperatures are subjected to a combination of steady and cyclic loading, which can lead to creep-fatigue interaction and environmental effects. High temperature fatigue resistance of alloys is profoundly affected by corrosion processes which influence the time to crack initiation and growth mechanisms at the crack tip. At high temperature such corrosion mechanisms take place synergically with creep processes and lead to an acceleration of crack initiation and propagation and to a reduction in fatigue life. The presence of time dependent processes in fatigue can dramatically change the expected fatigue behavior and complicate the extrapolation process of laboratory data to the correlation of the components in service.

In general, situations involving high temperatures and high stress-ratios would be expected to favor crack growth by creep deformation. In contrast, low temperatures and low stress-ratios should result in fatigue dominated crack extension. It is of practical importance to establish the mechanism controlling crack propagation in order that the correct characterizing parameter can be used. C^* should be employed when cyclic crack growth is predominantly time dependent and ΔK should be used if it is cycle dependent.

To investigate the effect of hold time, tests are generally conducted with hold times imposed at either the tension or the compression peak of each cycle. A reduction in the fatigue life is observed for the hold time in tension, and the cracked surface is usually intergranular because of the creep damage sustained during the tensile hold period.

Potential drop changes versus number of cycles in fatigue tests without hold time effects are given in Figure 3.19. The experimental data were fitted with a best fit line and the crack growth rates were calculated. Diagrams of fatigue crack propagation rates da/dn versus range of the stress intensity factor ΔK for the fine grain material (samples 04F) and the coarse grain material (samples 01C) are given in Figure 3.20. It can be seen that, for the same values of ΔK , the fine grain material has much lower resistance to crack propagation than the coarse grain material. Crack growth behavior in the coarse grain material indicates a non-uniform crack propagation which is consistent with visual observations through the travelling microscope during testing and with the visual investigations of cracked surfaces described later.

The threshold stress intensity factor, ΔK_{th} , can not be estimated accurately from the results obtained, because of the error involved in extrapolating the da/dn values to lower region. However, it can be safely assumed to be less than $21.8\text{MPa}\sqrt{\text{m}}$ for each of the investigated materials.

Results of crack growth in low cycle fatigue with hold time are given in Figure 3.21. This figure shows the crack propagation rate versus the stress intensity factor range for the fine grain material (04F) in two of specimens (HF3 and HF5). It can be seen that there is a shift between curves. The initial loading conditions for specimen HF5 were the same as in fatigue tests without a hold time (initial $\Delta K \sim 19.6\text{MPa}\sqrt{\text{m}}$), whereas specimen HF3 was loaded with higher ΔK at the beginning

(initial $\Delta K \sim 30.5\text{MPa}\sqrt{\text{m}}$). This difference causes the shift observed in these two curves.

The relationship between da/dn and ΔK for the coarse grain material (01C) is plotted in Figure 3.21. For this specimen (HF4) the crack propagation was very slow with an approximately constant rate of 7.6×10^{-4} mm/cycle. After 40 hours, the crack propagation was arrested because the main crack split into two cracks, as shown in Figure 3.28, and the crack growth rate dropped dramatically even when a higher ΔK value ($\Delta K > 45.8\text{MPa}\sqrt{\text{m}}$) was employed.

From the comparison of the crack propagation rate versus the stress intensity factor range for fatigue with and without hold time effects in Figure 3.21 and Figure 3.20, it is obvious that, for the fine grain material, the fatigue crack growth rates are much higher with hold time. In contrast, the hold time does not influence significantly the fatigue crack propagation rate in the coarse grain material. From this, it is evident that the fine grain material reveals time dependent behavior at elevated temperatures.

3.3.2. Microstructural Effects on Fatigue Behavior

Figure 3.22 is the crack profile of a high temperature low-cycle fatigued fine grain sample. Figure 3.23 is the crack profile of a high temperature low-cycle (with holding time) fatigued fine grain sample. Comparing these two profiles, it can be concluded that:

- 1) The profile in Figure 3.23 (with holding time) has more secondary cracks or crack branches, and the main crack here is also wider;
- 2) The profile in Figure 3.22 (without holding time) has a large damage zone in which several microcracks appeared, and several discontinuities can be observed

along the main crack path.

Testing conditions for these two samples differed in the holding time at peak load level. The difference in the crack profiles could be introduced by the hold time effect. With hold time, the crack tip is in the opening state for most of the test duration and such a state favors crack growth. Assuming here that ΔK_{\max} is only a function of the crack length, the average ΔK for the sample with hold time will be higher, at any time step, than that of the sample without the hold time. So the fatigue fracture life (time) should be shorter. The main crack profile is essentially formed by the extension of crack tip. It is close to the profile of the creep-crack propagation sample.

The sample tested without the hold time behaves in a typical high temperature-low cycle fatigue mode. There is a damage zone ahead of the crack tip with some microcracks initiated. During the following cycles, the main crack may assimilate these microcracks and hence propagate in a discontinuous way.

Usually, high temperature low cycle fatigue (LCF) may be a combination of the fatigue and creep processes. However, as discussed in the Section 3.1., the fine grain microstructure has a higher creep deformation resistance and behaves in a brittle manner under creep conditions. Therefore, fatigue is the principal deformation mechanism.

In this test, ΔK exerted on the sample increases with crack growth, i.e. ΔK is not a constant. Fractographic studies show that near the notch where the crack initiates and ΔK is lower, crack growth occurs in an intergranular manner: the facets are flat and grains can be easily identified, as shown in Figure 3.24; on the other hand, after crack propagation over some distance, intergranular fracture mode is replaced gradually by the mixed mode: the fracture surface looks more like a ductile

fracture surface (see Figure 3.25).

Figure 3.26 is the crack tip structure for Figure 3.22 crack profile. Several microcracks can be seen near the crack tip. Some of them are oriented along the grain boundaries and some extend in a transgranular mode. This is consistent with the fractograph shown in Figure 3.25. The ΔK value increases with the crack extension. When the crack is short, i.e. at low ΔK , pure high temperature fatigue seems to have occurred in the sample and grain boundary cleavage is the main fracture mode. As the crack gets longer, the ΔK value also increases, leading to extensive plastic deformation, i.e. fracture transferred from grain boundaries to the interior of grains.

Figure 3.27 is the crack profile of a high temperature low cycle fatigued coarse sample. Figure 3.28 is the crack profile of a high temperature low cycle (with holding time) fatigued coarse grain sample. Figure 3.29 shows the crack tip structure of the profile shown in Figure 3.27, Figure 3.30 shows the crack tip structure of the profile shown in Figure 3.28. They indicate again that the cracks pass the dendrite area by selecting the inter-dendrite region as the preferred path of propagation. Dendrite structure can be recognized in the fractographs of these samples. Since coarse grain samples have less creep resistance, under the high temperature+holding time test conditions, creep deformation may not be a negligible part of the total deformation. For LCF with holding time in coarse grain samples, the deformation mechanism should be close to that of creep crack propagation. As creep deformation can not be separated from the total deformation, it is difficult to estimate how much of the deformation comes from each of the processes.

Comparing Figure 3.28 to Figure 3.27, it can be seen that:

- 1) Crack of the sample fatigued with holding time is wider than that of the sample without holding time;

- 2) In the sample fatigued with hold time, the main crack finally divides into two branches, each of them having an approximate 45° angle to the original crack growth direction. The reason for such division is not clear.
- 3) The crack tip structure for these two specimens are similar. Basically, crack tips select inter-dendrite regions as their propagation paths.

As shown by $da/dN-\Delta K$ curve (Figure 3.20), da/dN has a tendency to increase with the increase of crack length (or ΔK). But in some cases, da/dN may decrease, i.e. $(da/dN)/d(\Delta K)$ may have a negative value, especially in the coarse grain sample.

Based on the in-situ observations, crack propagates discontinuously. This fact is consistent with the sinuous shape of the $da/dN-\Delta K$ curve and it is related to the difference in the crack propagation resistance of the different microstructures encountered by the crack tip. In the coarse grain sample, differences in propagation resistance are very large from point to point. Some areas (e.g. intra-dendrite region) have a high resistance to crack growth; some areas (e.g. inter-dendrite region) have a low resistance. In the fine grain samples, since cracks propagate along grain boundaries and there are many grain boundaries available, the continuity of crack growth is much better.

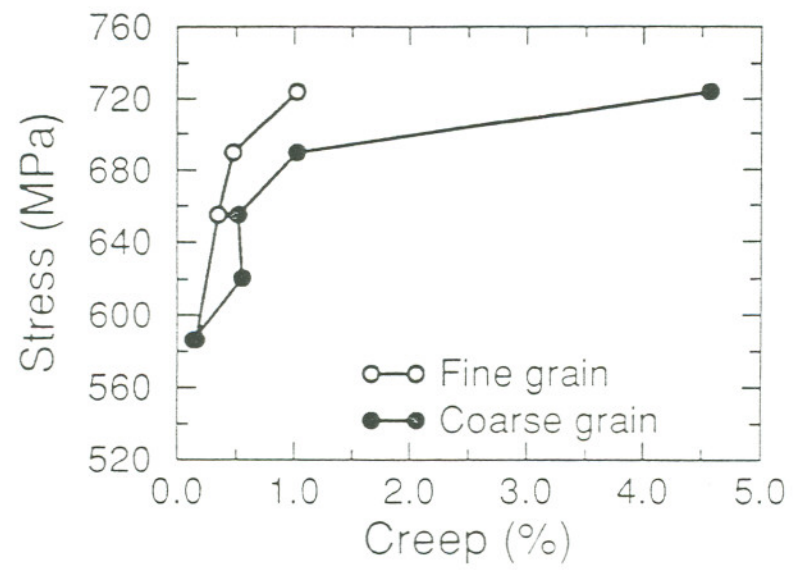


Figure 3.1 Stress-strain diagram at a constant creep time of 50h

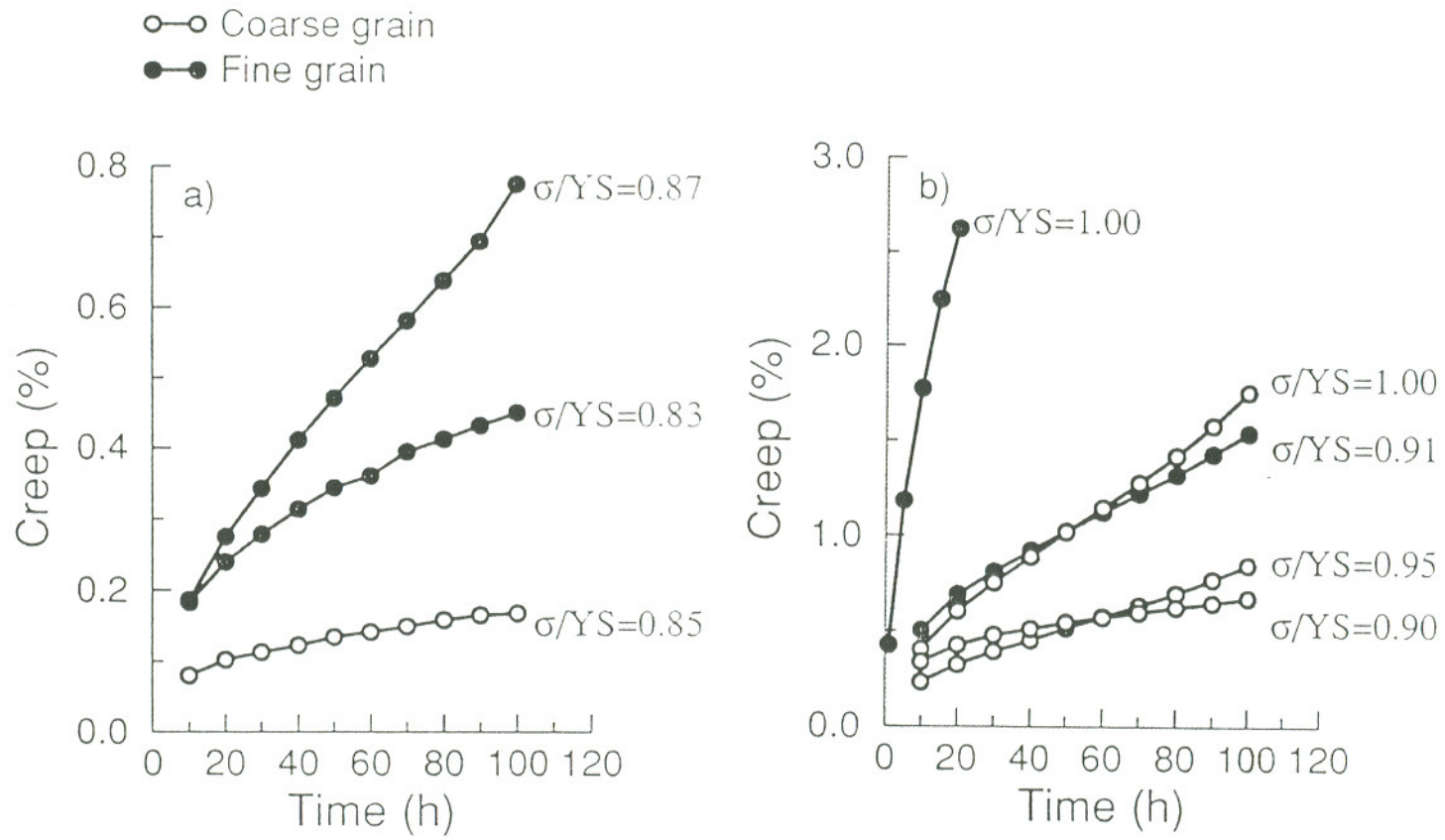


Figure 3.2 Strain-time diagrams under creep conditions for different σ/Y_S ratio

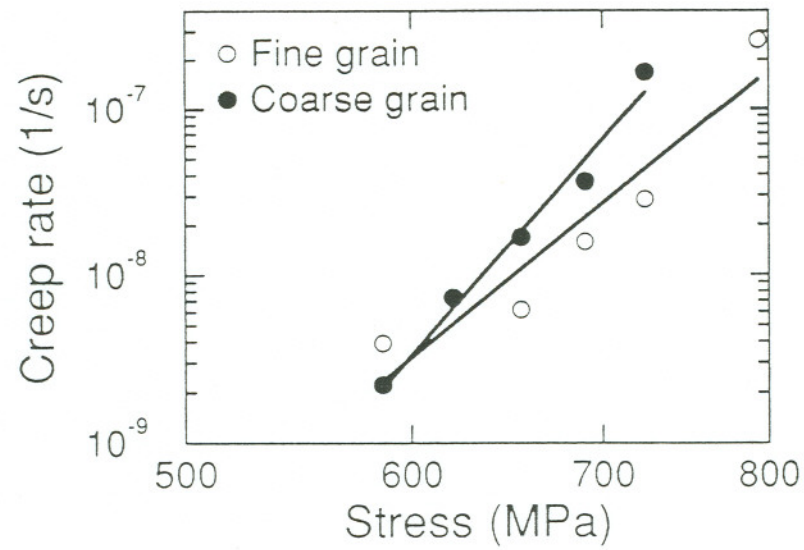


Figure 3.3 Creep rates (secondary creep only) versus stress for fine and coarse grain materials

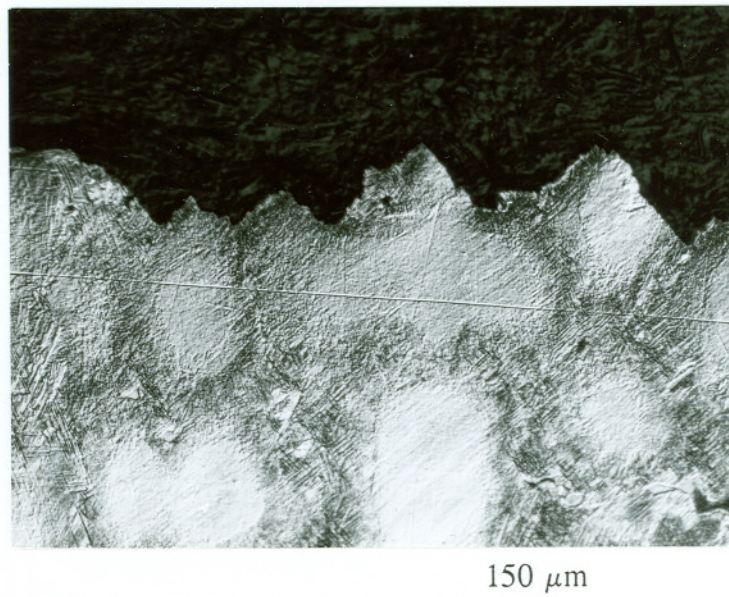
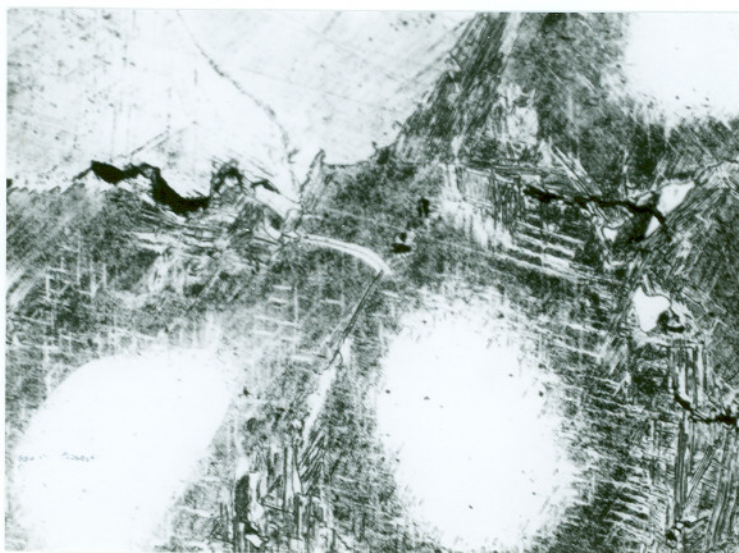


Figure 3.4 Crack propagation path in a creep tested coarse grain sample



0.3 μm

Figure 3.5 Persistent slip band in a creep tested coarse grain sample



75 μm

Figure 3.6 Creep crack initiation in a fine grain sample

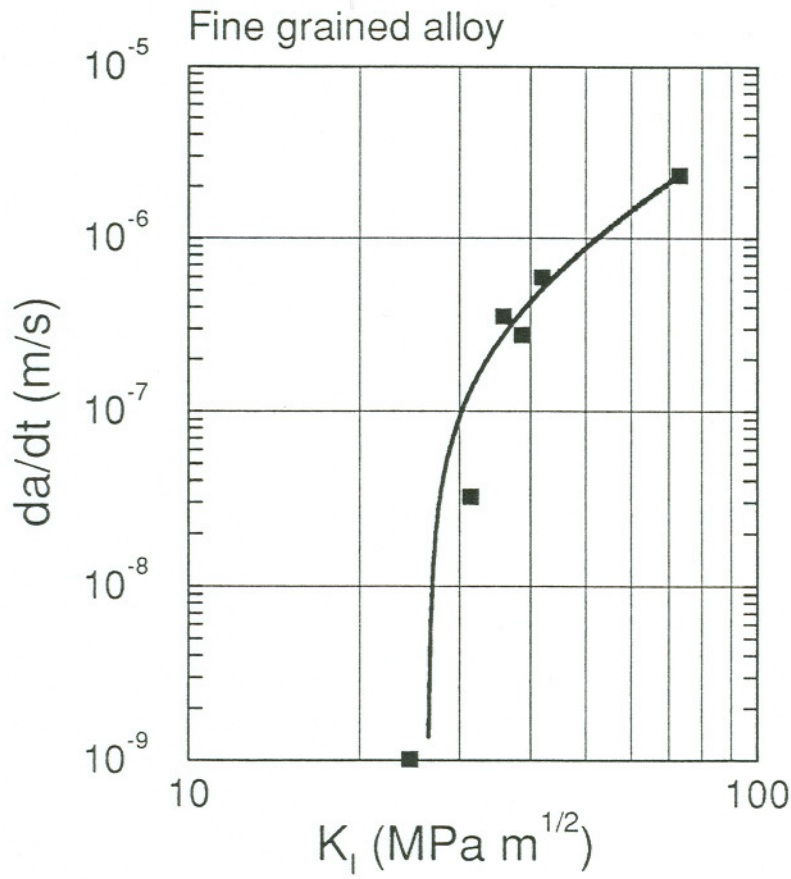


Figure 3.7 Creep crack propagation rate, da/dt versus the stress intensity factor, K

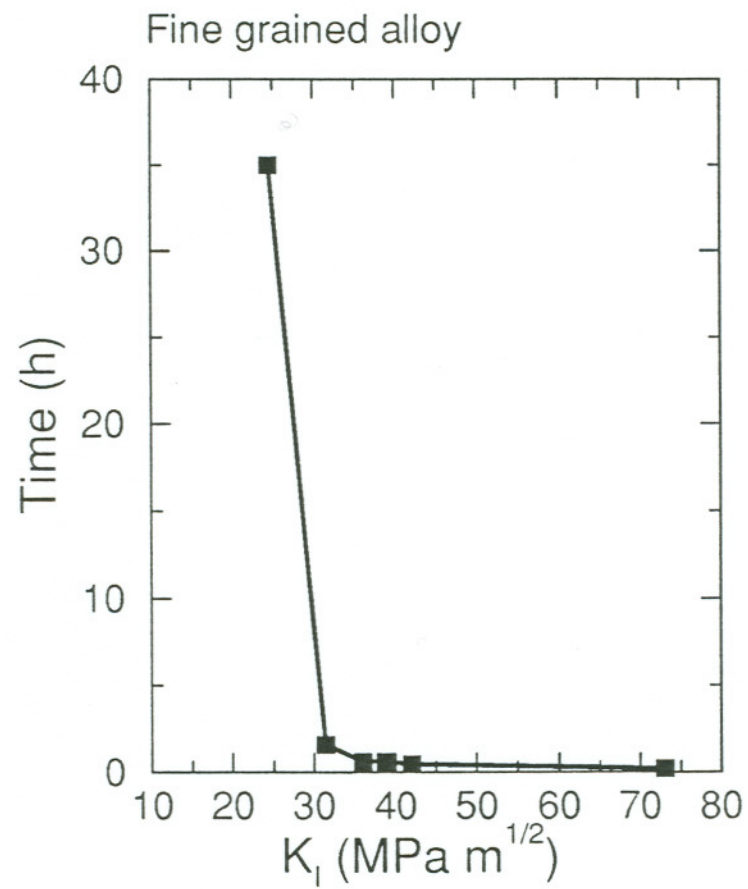


Figure 3.8 Time of crack incubation as a function of the stress intensity factor in constant K specimen tests

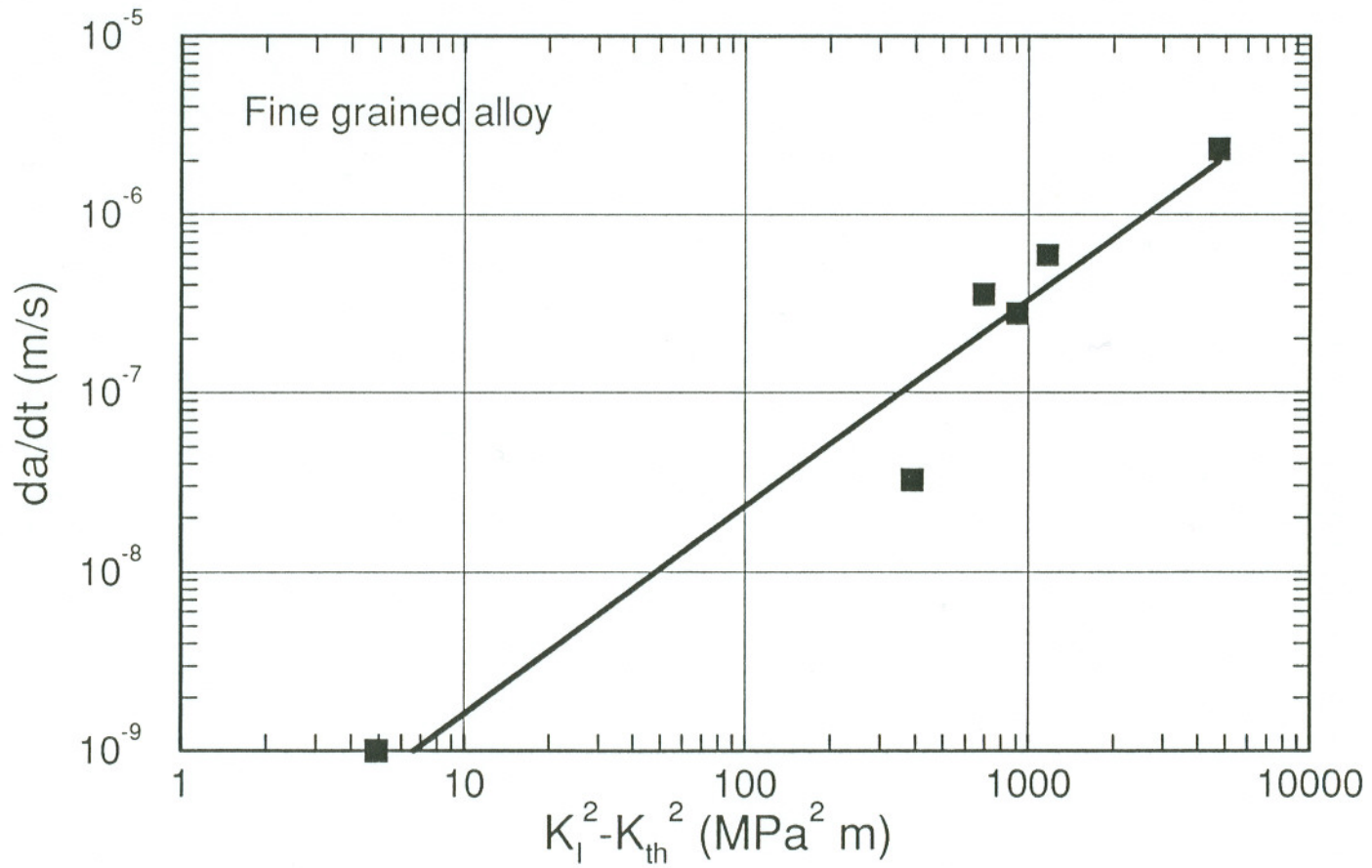


Figure 3.9 Creep crack propagation rate, da/dt versus the effective driving force, $G_e \sim K^2 - K_{th}^2$

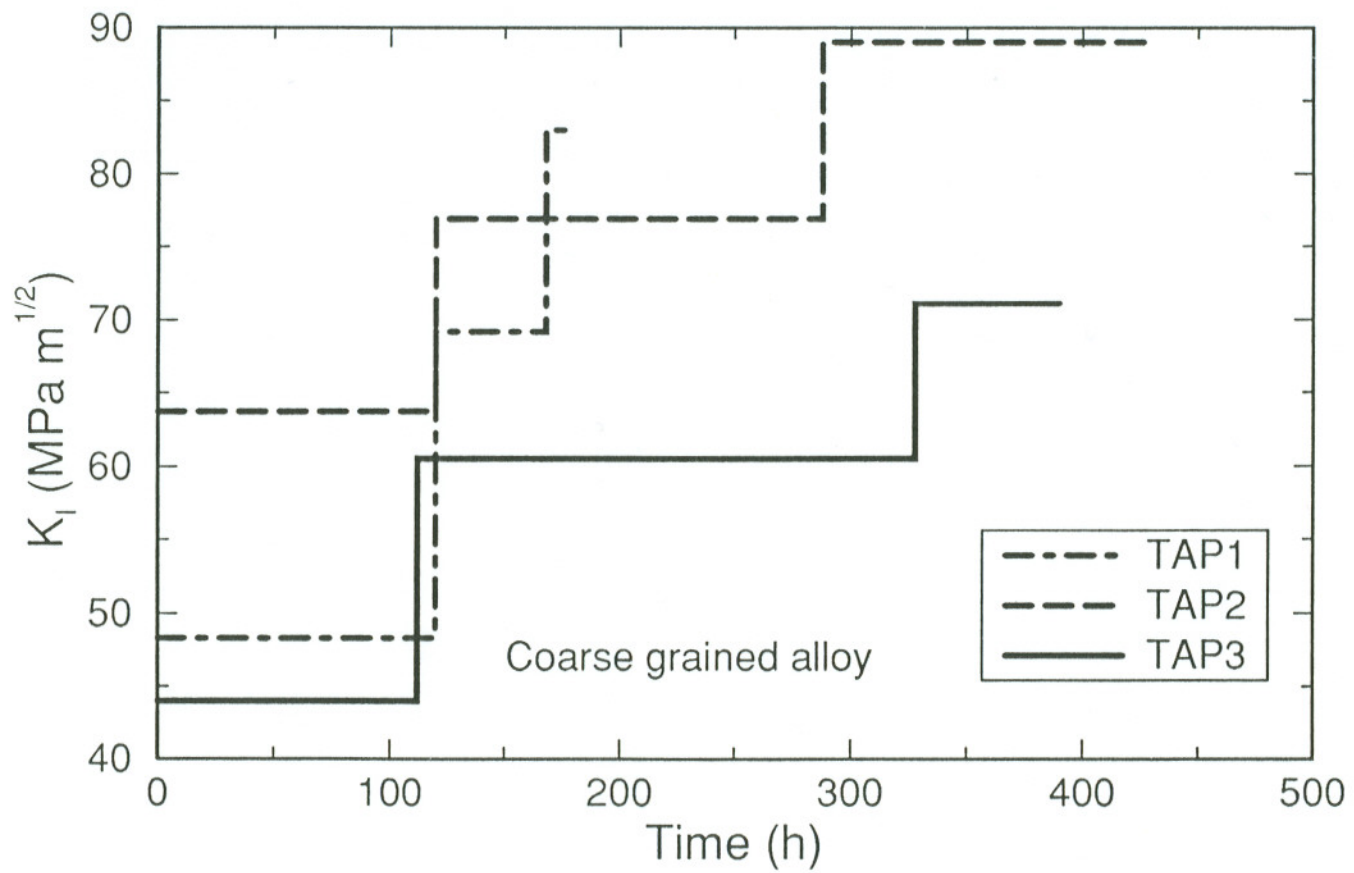


Figure 3.10 Stress intensity history used in the coarse grain specimens

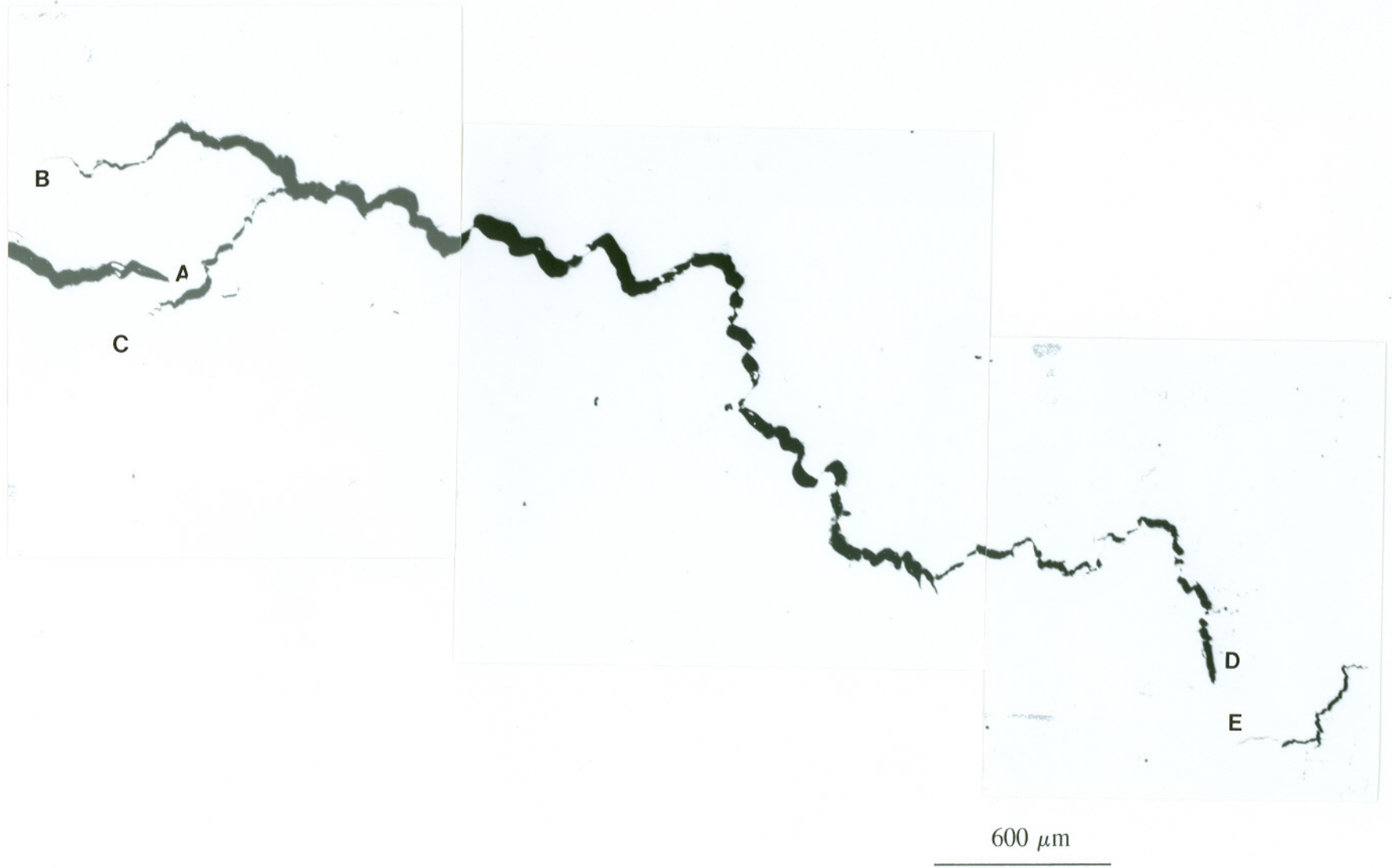
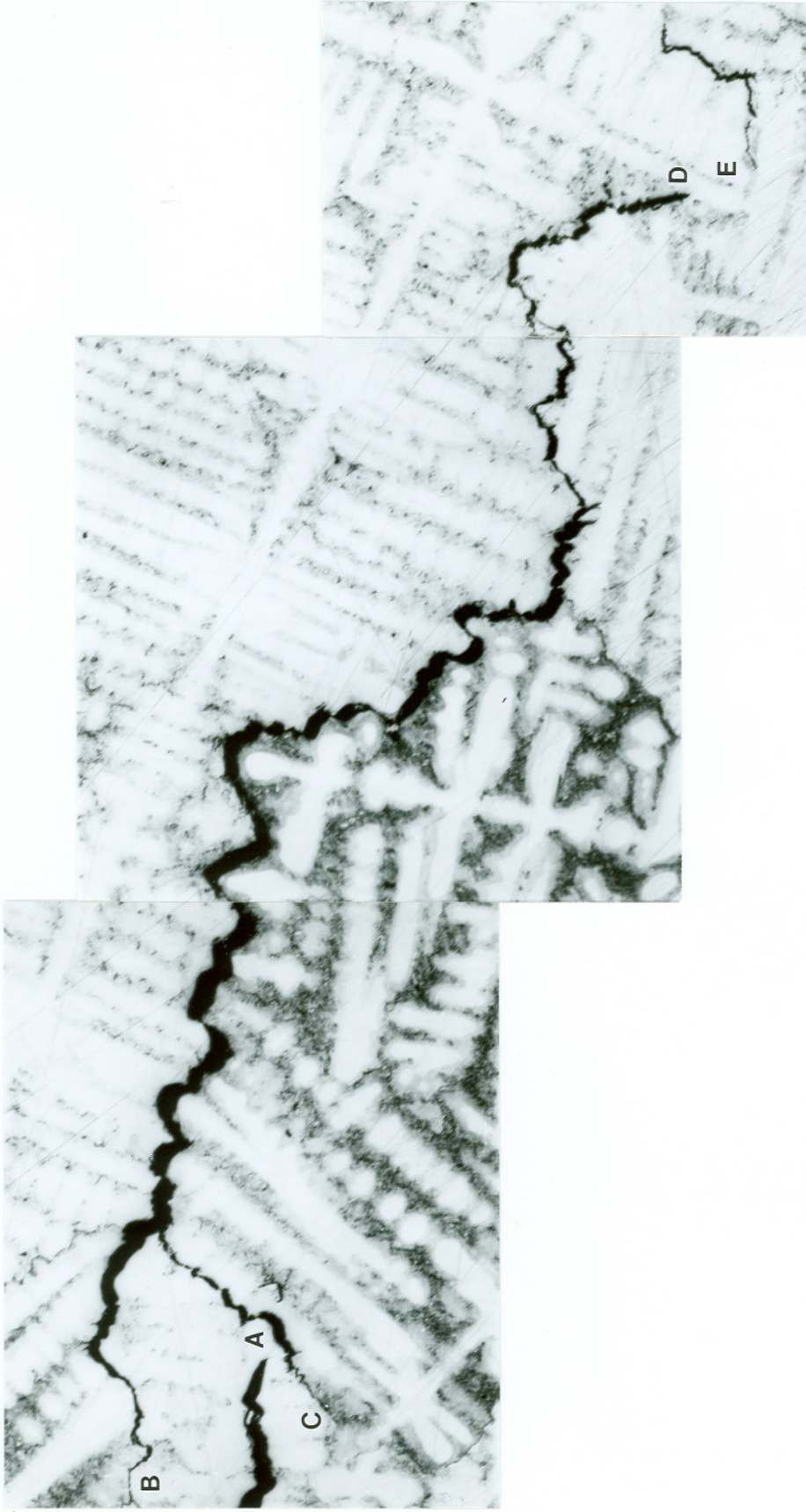
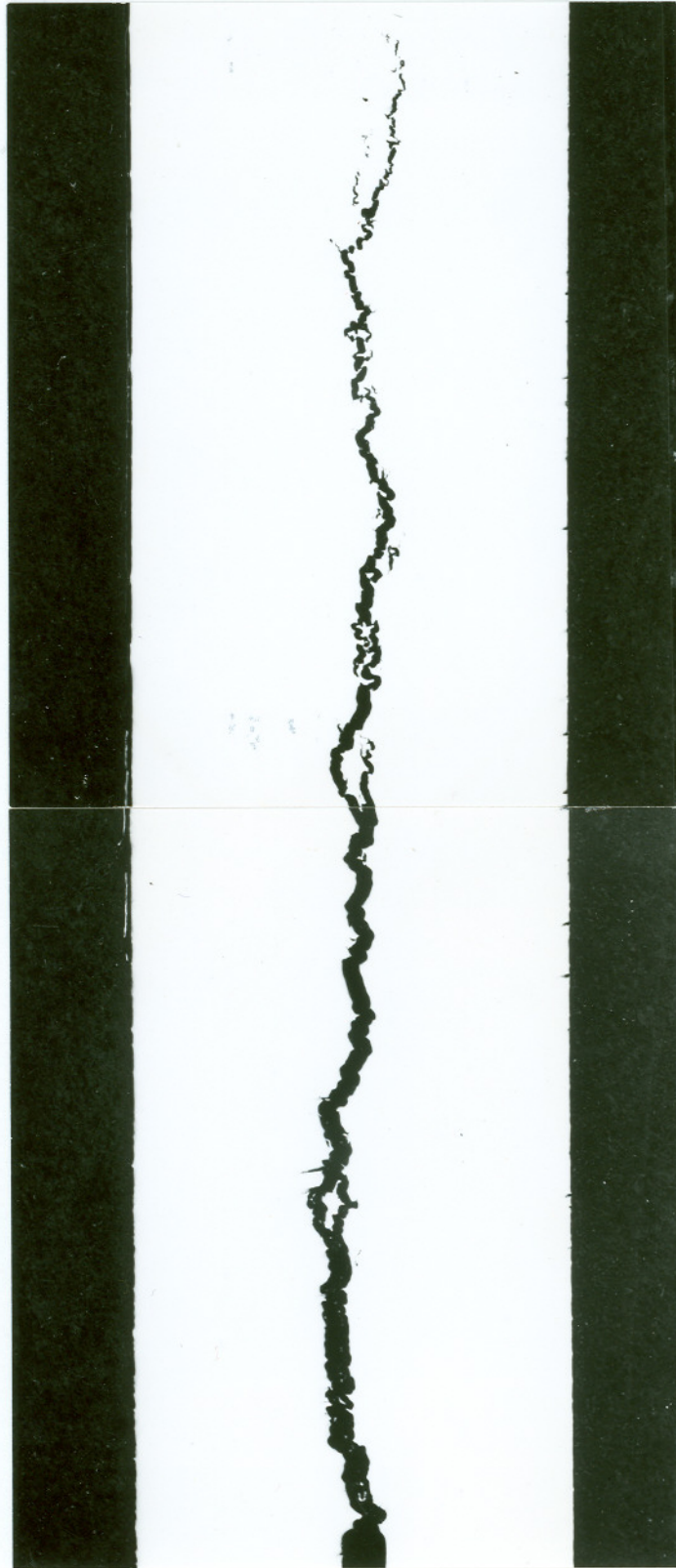


Figure 3.11 Crack profile of a coarse grain sample (TAP3)



600 μm

Figure 3.12 Crack profile of a coarse grain sample (TAP3)



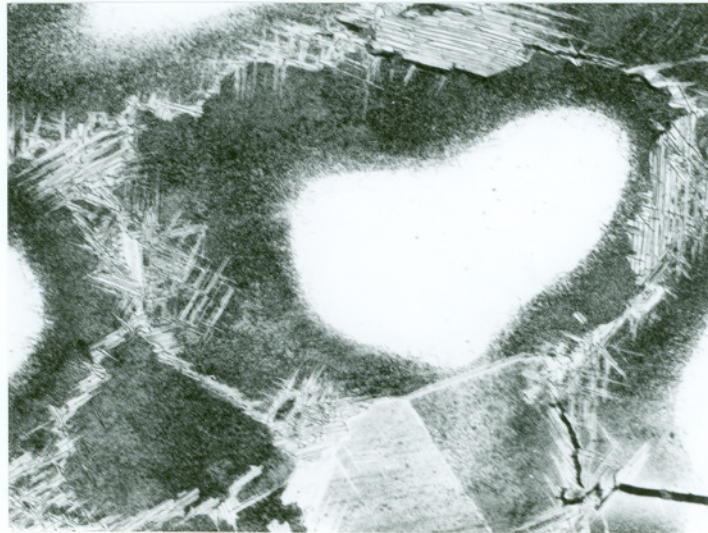
3 mm

Figure 3.13 Crack profile of a fine grain sample (TAR 4)



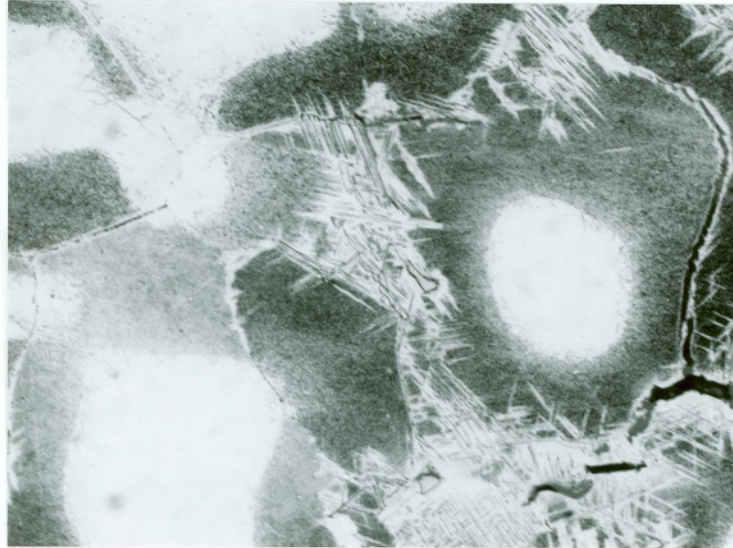
75 μm

Figure 3.14 Crack tip structure of a fine grain sample (TAR1)



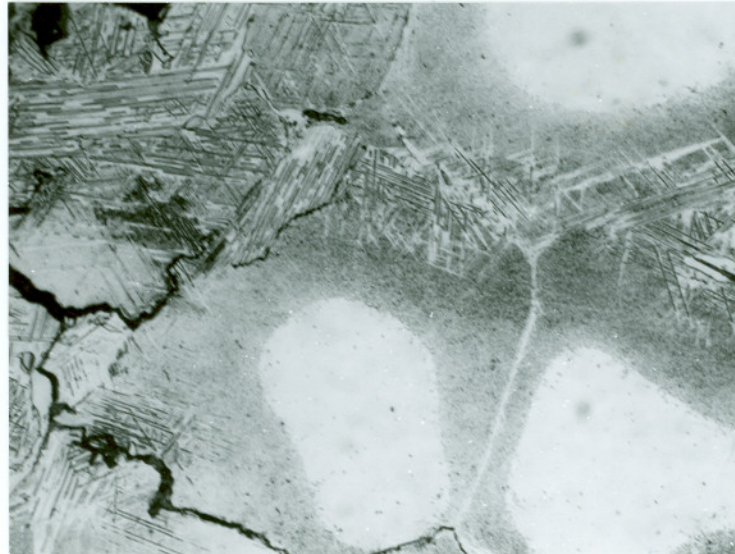
75 μm

Figure 3.15 Crack tip structure of a fine grain sample (TAR2)



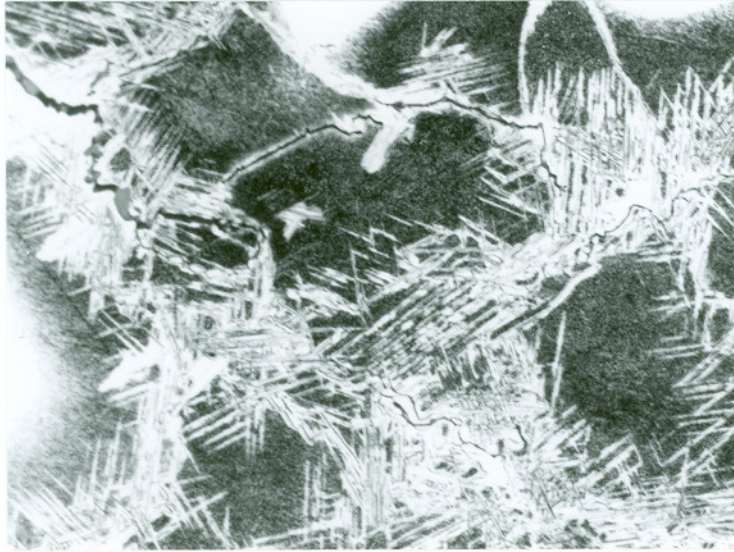
75 μm

Figure 3.16 Crack tip structure of a fine grain sample (TAR3)



75 μm

Figure 3.17 Crack tip structure of a fine grain sample (TAR4)



75 μm

Figure 3.18 Crack tip structure of a fine grain sample (TAR5)

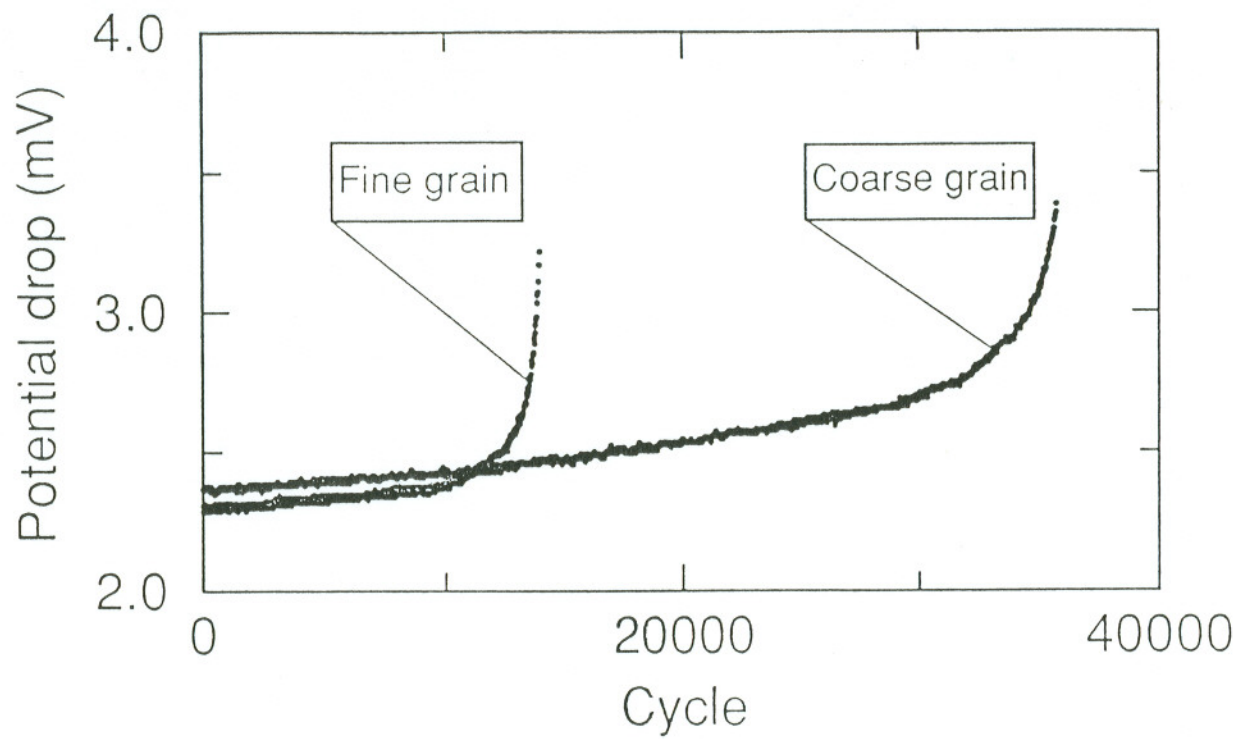


Figure 3.19 Potential drop versus number of cycles in fatigue tests without hold time effect

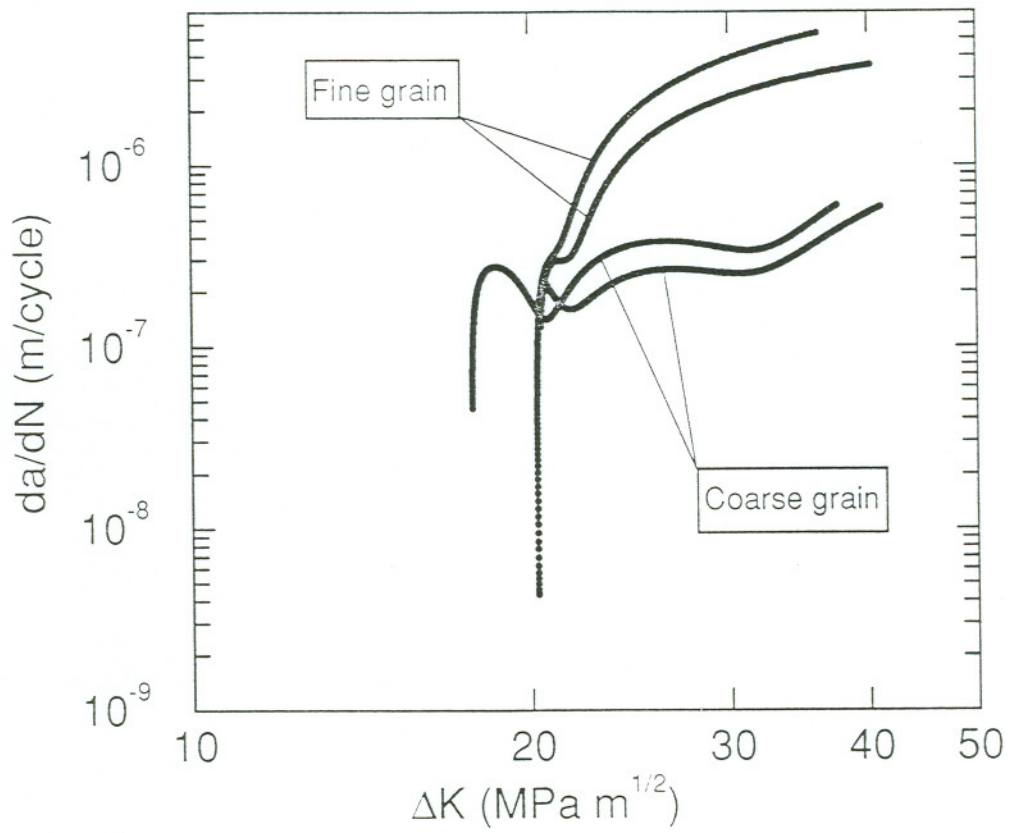


Figure 3.20 Comparison of fatigue (without holding time) crack propagation rates in coarse and fine grain samples

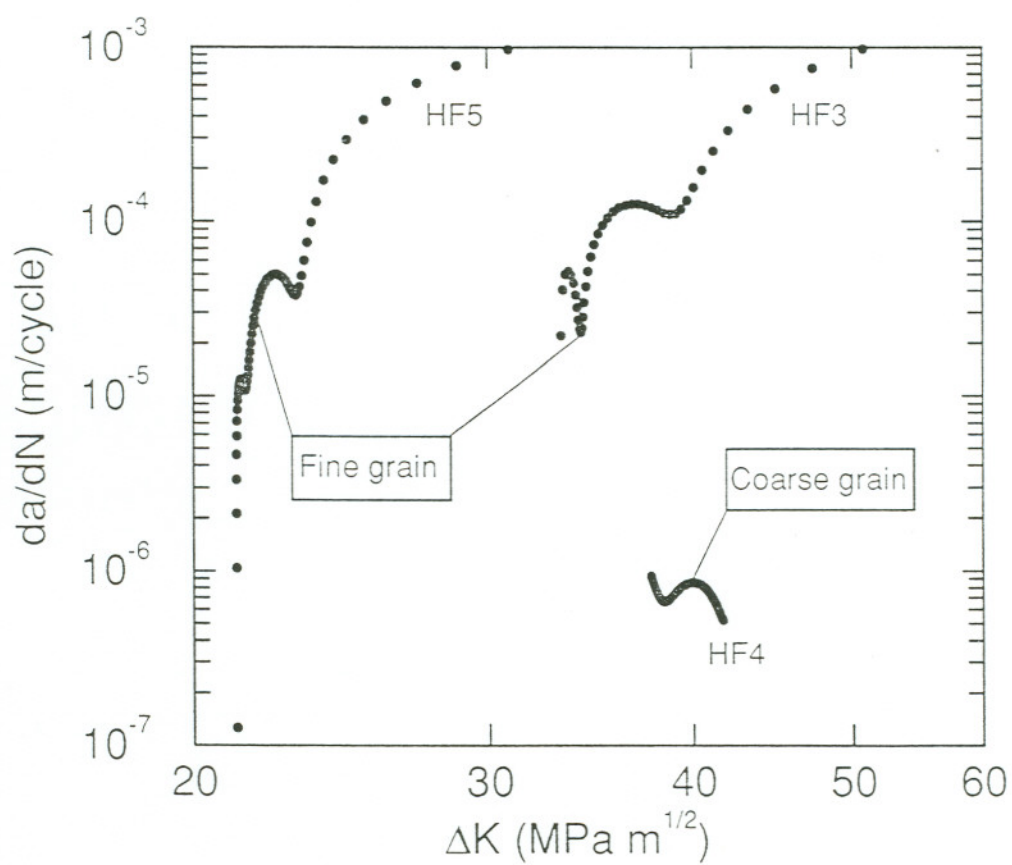
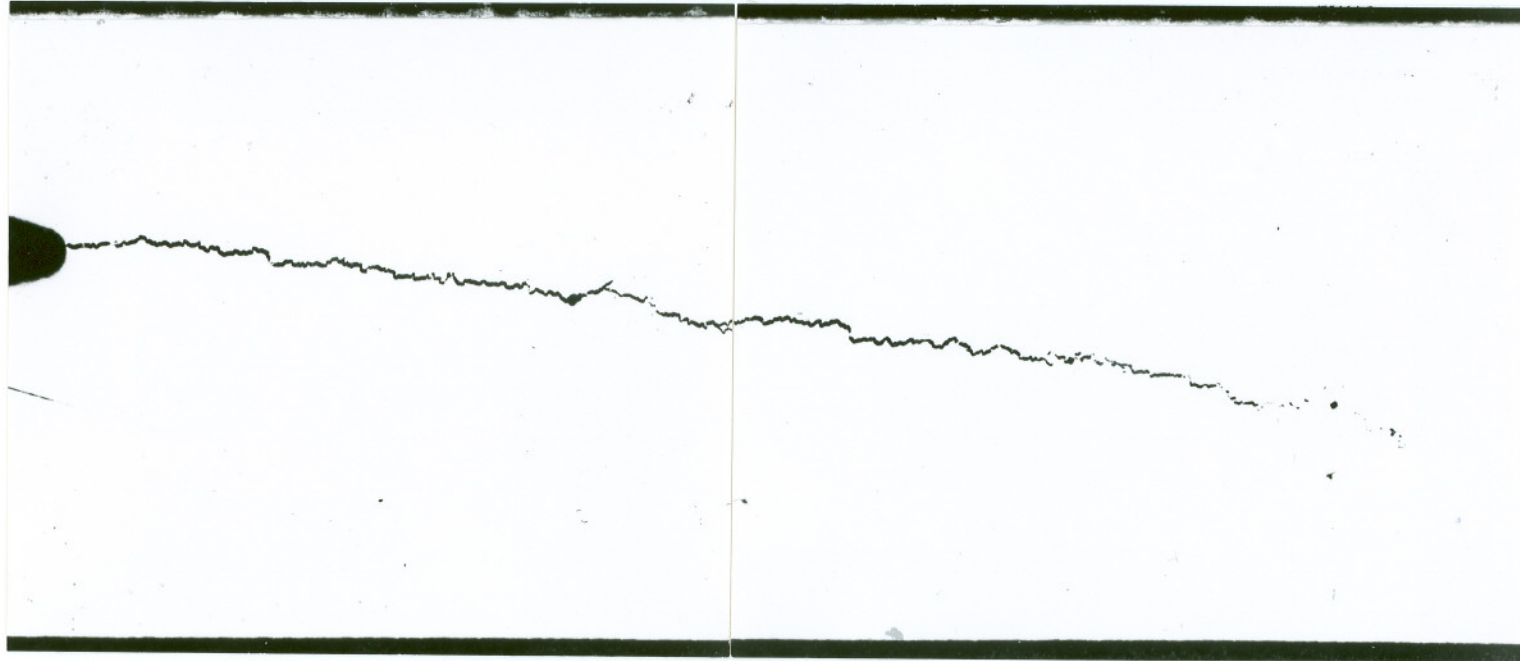
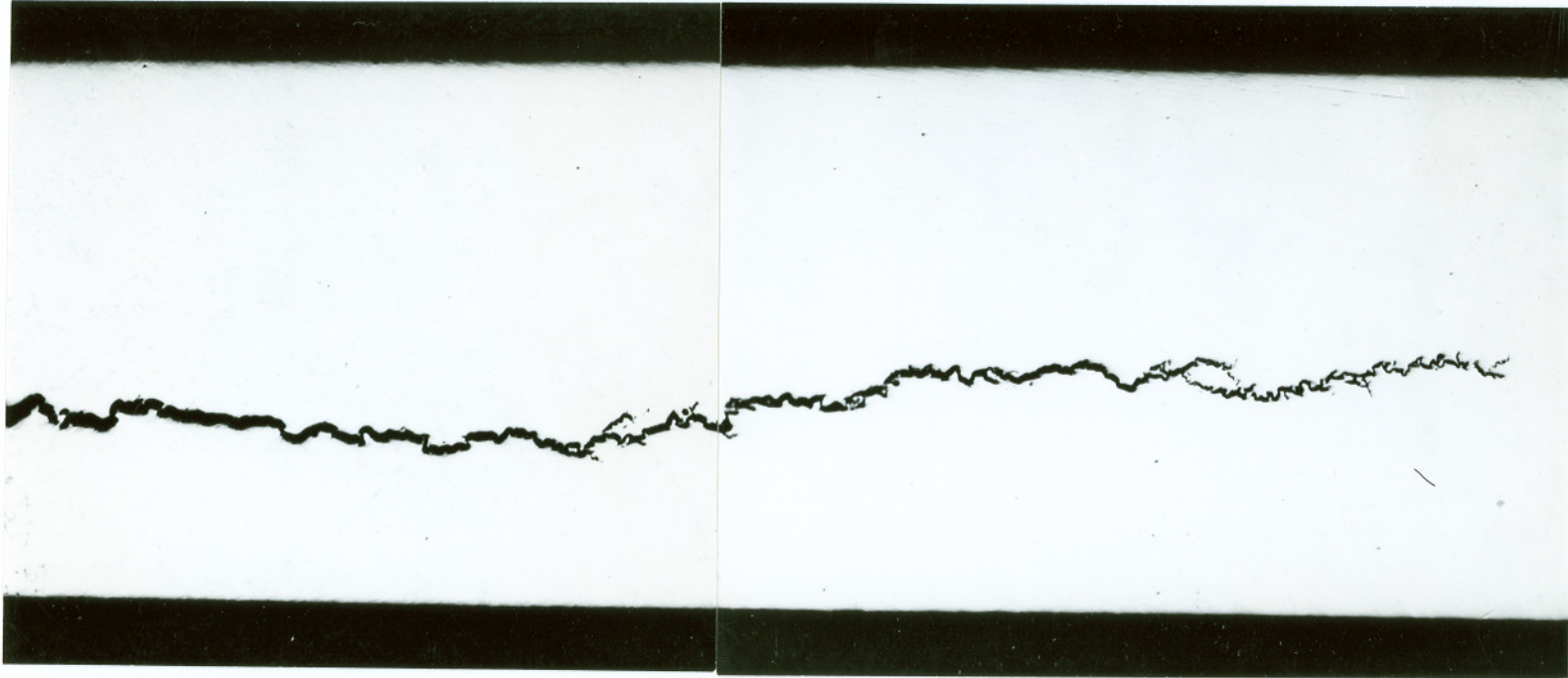


Figure 3.21 Fatigue (with holding time) crack propagation rates versus the stress intensity factor range in coarse and fine grain samples



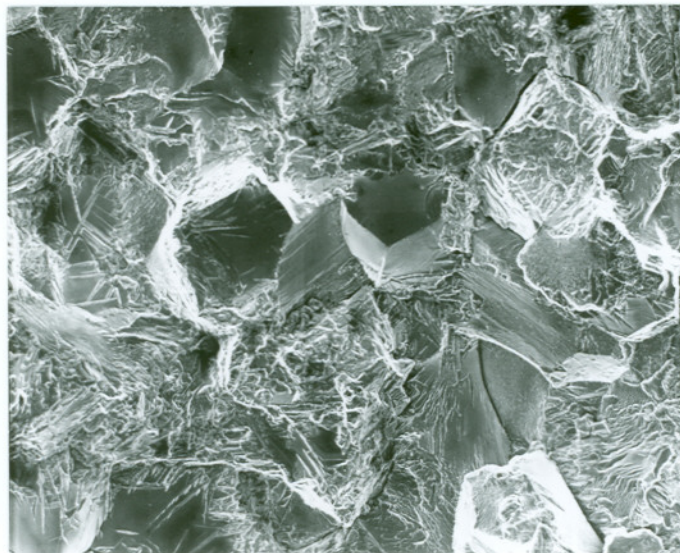
3 mm

Figure 3.22 Crack profile of a fatigued fine grain sample



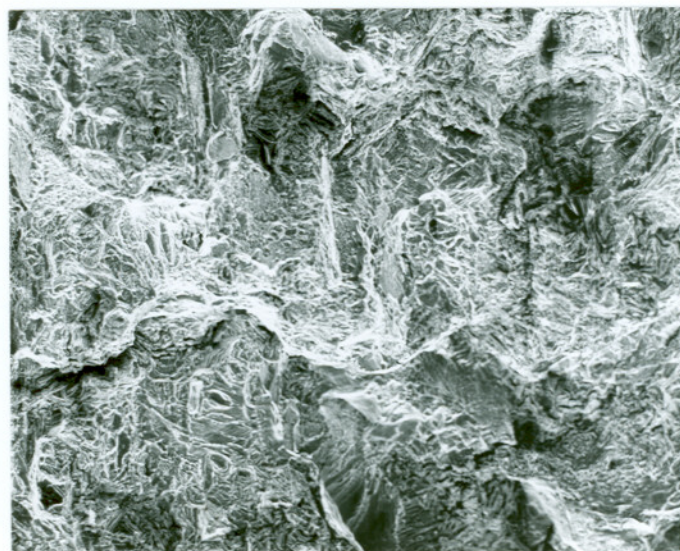
3 mm

Figure 3.23 Crack profile of a fatigued (with holding time) fine grain sample



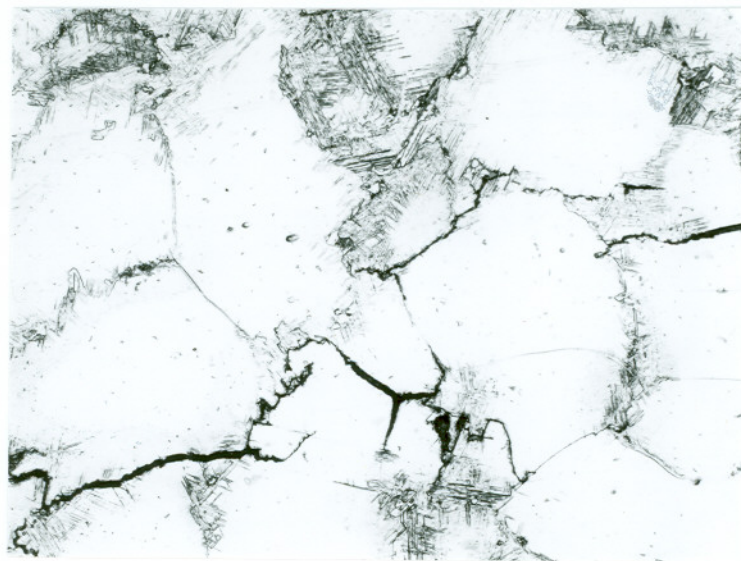
150 μm

Figure 3.24 Fractograph of a fatigued fine grain sample



150 μm

Figure 3.25 Fractograph of a fatigued fine grain sample



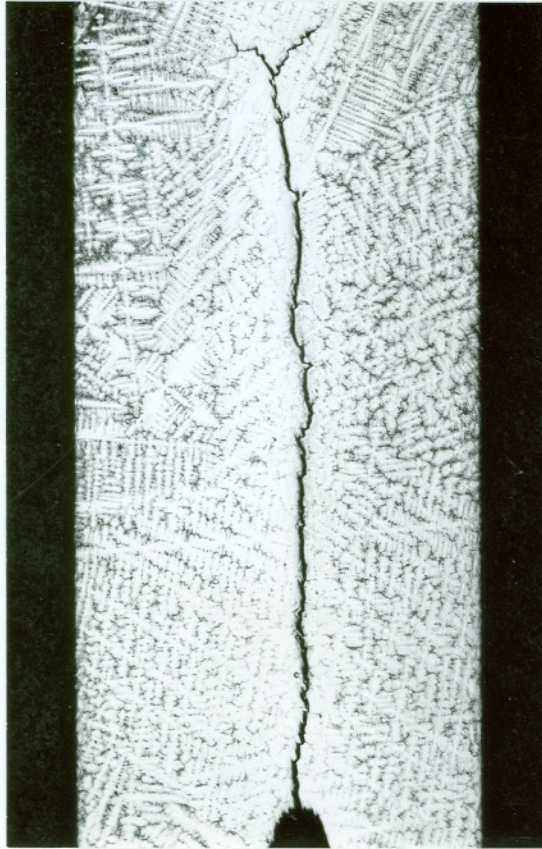
150 μm

Figure 3.26 Crack tip morphology of a fatigued fine grain sample



3 mm

Figure 3.27 Crack profile of a fatigued coarse grain sample



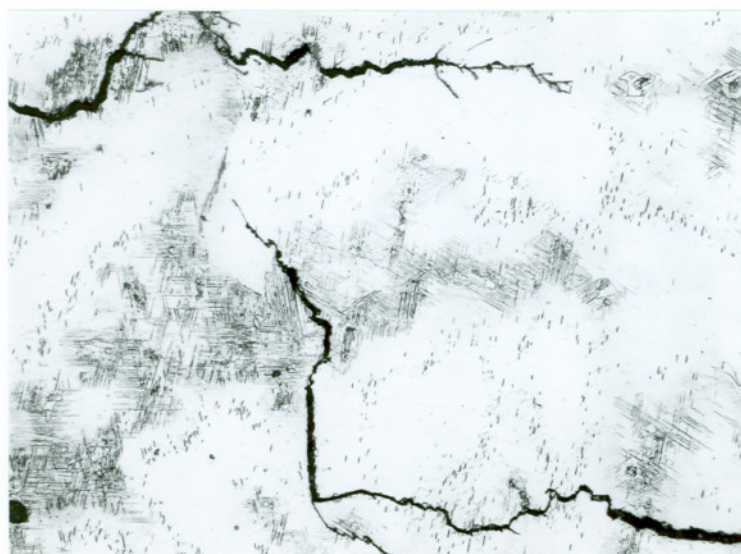
3 mm

Figure 3.28 Crack profile of a fatigued (with holding time) coarse grain sample



75 μm

Figure 3.29 Crack tip morphology of the crack profile in Fig. 3.27



75 μm

Figure 3.30 Crack tip morphology of the crack profile in Fig. 3.28

CHAPTER 4

RESULTS AND DISCUSSION (48-2-2 TiAl ALLOY)

As mentioned above, the low RT ductility of TiAl alloys is the largest obstacle to their engineering applications as structural material. In the last decade, research has been mainly concentrated on RT ductility improvement. The highest ductility reached in laboratory conditions has been about 4% with a precise control of chemical composition (including impurity level) and microstructure. However, a higher value of room temperature ductility is required for such materials to be used in engineering applications. Therefore, ductility improvement is still a major concern in this field of research.

The purpose of the present research project is to develop a γ -based TiAl alloy which is ductile at room temperature. Experimentally, several approaches have been tried, including different solidification rates, microstructures and testing temperatures. Theoretically, the study was concentrated on the possible plastic deformation mechanisms in γ -based TiAl alloys under RT conditions. The following characteristics of the system were discussed in detail: 1) Difference in plastic deformation ability between α_2 and γ phases, 2) The role of α_2 in the system, and 3) The characteristic of the α_2/γ phase boundary. The material used here in the tests was the alloy "48-2-2" (48Al-2Cr-2Nb in at.%).

4.1. Effect of Solidification Rate on RT Ductility

In these tests, samples were cast with different solidification rates by controlling casting mold temperature and insulation condition. These solidification

rates were categorized as slow, medium and fast. All the samples were then HIP treated. The results from the RT tensile tests are listed in Table 4.1. It can be clearly seen that the ductility improves with increasing solidification rate and this can be expected because of the finer microstructure with faster solidification rates.

Table 4.1 Tensile Properties of the Specimens with Different Solidification Rates

Specimen Number	Solidification Rate	Ultimate Strength (MPa)	Total Strain (%)	Elastic Strain (%)	Plastic Strain (%)
60-04	slow	440.91	1.89	0.34	1.55
60-05	slow	456.09	1.45	0.30	1.15
75-06	medium	426.97	2.22	0.28	1.94
75-07	medium	343.97	1.61	0.35	1.26
63-14	fast	494.04	3.00	0.31	2.69
63-15	fast	477.27	2.72	0.42	2.30

Figures 4.1 to 4.3 show the microstructure of the samples with different solidification rates. All of them have a duplex microstructure which is composed of lamellar structures and equiaxed single phase γ grains. The characteristic columnar structure grains consist of alternating layers of α_2 and γ . These columnar structures grow first from the circumference to the center of samples with some equiaxed γ -grains forming between the columns. However, the phase distribution, grain size, morphology and relative volume fraction are different for each specimen. As the solidification rate increases (from Figure 4.1 to Figure 4.3) the size of both the γ

grain and $\alpha_2 + \gamma$ lamellar packet decrease and the structure tends to become more uniform. A γ -rich core appears in the specimen with slow solidification rate and large size $\alpha_2 + \gamma$ columns can be seen around the core. The phase distribution is non-uniform, as shown in Figure 4.1. In the specimen with medium solidification rate (Figure 4.2), the γ -rich core disappears. The structure is basically a mixture of γ and $\alpha_2 + \gamma$ lamellar packets. In the specimen with fast solidification rate, as shown in Figure 4.3, the volume fraction of γ -grains increases but their size decreases. Some small γ -grains even appear within $\alpha_2 + \gamma$ lamellar structure. There is a large size difference among γ -grains and the columnar nature of the $\alpha_2 + \gamma$ grains seems to have been slightly obscured.

Cleavage appears to be the most common mode of fracture in these samples. River patterns which are typical of cleavage, as shown in Figure 4.4, can be seen in all the samples. The presence of the river patterns indicates that the fracture mode is basically brittle. Macro-fracture surfaces are flat and perpendicular to the tensile axis. However, the micro-cleavage path can transform from one crystal direction to another and form a sinuous pattern, as shown in Figure 4.5. The secondary fracture mode is the so called "cracking through lamellae" fashion as shown in Figure 4.6. This mode is produced by a crack cutting through the lamellar structure, and has a different morphology according to the orientation relationship between cracking direction and lamellae direction. Another important fracture feature is the interface debonding between the α_2 layer and the γ layer, as shown in Figure 4.7. This mode becomes more apparent when the grain size increases. In the samples with slow solidification rate, fracture is caused mainly by cleavage and "cracking through lamellae" mode, as shown in Figure 4.8. Due to the large grain size, fracture units are also large. In contrast, fracture units in the sample with fast solidification rate are small, corresponding to its small grain size, and the basic fracture mode is quasi-cleavage which is an indication of some ductile deformation.

It is clear that the ductility of the alloy is closely related to the microstructure. Although all the samples have the same complex structure, differences in the constituent size and uniformity of phase distribution result in differences in the RT ductility. It is well known that a finer grain size corresponds to higher RT ductility because of better deformation compatibility. The refinement is thought to promote increased ductility and tensile strength in γ -based alloy (59), and is the main advantage of fast solidification processing over slow solidification processing. Also, as will be discussed later, in terms of carrying plastic deformation, γ phase plays a more important role than α_2 phase. In the sample with more uniform phase distribution (in this case, the sample with fast solidification rate), deformation is also uniform. Therefore, stress and strain concentrations are minimized.

4.2. Effect of Microstructure on RT Ductility

Various post-cast treatments, such as HIP and heat treatment (HT), can be applied to TiAl alloys, depending on the required mechanical properties. Different routes and parameters of treatment will produce different structures and hence different RT ductility (116-125).

In the present work, a series of γ -based TiAl alloys samples were made using different techniques: As Cast, HIPing treated, HIPing treated + Heat Treatment treated. They are abbreviated As Cast, As HIP and HIP + HT, respectively.

In 48-2-2 samples, the As Cast microstructure consists primarily of large columnar grains containing lamellar $\alpha_2 + \gamma$ plates, as shown in Figure 4.9. Voids can be observed at the center part of the sample. These voids are the results of shrinkage during the solidification process. Backscattered electron image analysis indicates that chemical inhomogeneities are present in the As Cast material. Figure 4.10 is the microstructure after HIPing. HIPing did change the cast microstructure

appreciably. Shrinkage voids were totally eliminated, and recrystallized fine γ grains appeared everywhere. Both the structure homogeneity and the chemical composition homogeneity are much better than that of As Cast samples. With further heat treatment, as shown in Figure 4.11, a typical duplex structure was obtained. The ratio of lamellar structure/equiaxed γ grains decreased. As will be discussed later in the chapter, the equiaxed γ grains have a higher capability for deformation than other phase constituents.

Fractographic examination shows the difference in the fracture modes among these samples. Figure 4.12 was taken from the As Cast sample. Clearly, shrinkage voids act as existing microcracks, and these cracks cut through the remaining section area during the tensile test procedure. Figure 4.13 and Figure 4.14 are typical fracture surface morphologies obtained from tensile tested As HIP and HIP + HT samples respectively. These show that fracture occurs predominantly by cleavage across the equiaxed γ grains and the lamellar $\alpha_2 + \gamma$ grains. While there is some incidence of intergranular fracture on the fracture surface, transgranular fracture, which is manifested in the form of cleavage facets, is the dominating fracture mode. The fracture mode of lamellar structure is also important if its volume fraction is high. Based on the relative orientation of the crack with α_2/γ plates, such fracture can be categorized in one of three types: Crack Divider, Crack Delamination and Crack Arrester (124). All of these fracture modes were observed in this study.

Table 4.2 Tensile Properties of 48-2-2 TiAl Alloy with Different Microstructures

Specimen Number	Material Condition	Offset Yield Strength (MPa)	Ultimate Strength (MPa)	Elongation (%)	Area Reduction (%)
G40	As Cast	386.06	437.08	1	1
G43	As HIP	354.35	439.15	1	<0.5
G48	HIP + HT	404.68	450.15	<0.5	1

Note: Data in Table 4.2 are provided by Dr. R. Srivats of Precision Castparts Corp.

Table 4.2 lists the tensile test results of samples with different post-cast treatments. The As Cast sample has a higher σ_y value than the As HIP sample. No significant difference is found between the As HIP and HIP + HT samples. It should be noticed that the ratio of σ_y/σ_f for the As Cast sample (0.88) is higher than that for the As HIP sample (0.80). Two factors may be responsible for the phenomenon: 1) slip systems in the As Cast sample are not easy to activate and plastic deformation is not easy to transfer due to the coarse structure and lower deformation compatibility; 2) the existence of shrinkage voids and the low plastic deformation prohibit strain hardening. There is no significant difference in RT ductilities of these samples since all of them are very brittle.

4.3. Testing Temperature Effect

Table 4.3 lists the mechanical properties of a set of 48-2-2 samples which have the same microstructure and were tested at different temperatures. As expected, the ductility of the samples increased when the temperature increased. However, it is found that the ultimate tensile strength of the samples at high temperatures is higher

than at RT in this temperature range.

Table 4.3 Tensile Properties of 48-2-2 TiAl alloy at Different Test Temperatures

Specimen Number	Testing Temperature (°C)	Offset Yield Strength (MPa)	Ultimate Tensile Strength (MPa)	Elongation (%)	Area Reduction (%)
G40	RT	386.06	437.08	1	1
G40-1	650	337.81	461.21	3	3
G55	760	317.12	456.38	3	4

Note: Data in Table 4.3 are provided by Dr. R. Srivats of Precision Castparts Corp.

The positive temperature dependence of strength, typically the yield strength, of some intermetallic alloys in a certain temperature range was first reported by Kawabata et al (126). The strength anomaly was studied by several researchers (127-133). B.A. Greenberg et al. (127) attributed the anomalous temperature dependence of the yield strength in single crystals to 1) superdislocation blocking as a result of resplitting into some noncoplanar configurations or 2) blocking of single dislocations in deep Peierls valleys. Some examples for noncoplanar configurations are "roof"-type barriers, barriers of the two-layer twin type, barriers similar to Kear-Wilsdorf locks and Lomer-Cottrell-Hirth barriers. S. C. Huang et al. (129) found positive yield stress-temperature dependence in polycrystalline high Al low temperature heat treated single phase γ materials and indicated the anomalies were related to formation of faulted dipoles at elevated temperatures. They also believed that the following three factors, 1) interstitial hardening, 2) grain boundary strengthening, and 3) subtle effects of Al concentration, may affect such strength anomalies.

In the current study, the yield strength of the material has a negative dependence on the temperature. However, ultimate strength increases slightly with increasing temperature. It should be noticed that, until now, most yield strength anomalies are found in single crystal intermetallic materials and seldom in single phase polycrystalline materials. From the viewpoint of micro-mechanisms, plastic deformation in a single crystal may include the following steps: initiation of easy slip systems, defect densification and resultant hardening, opening of difficult slip systems under higher stress, local stress concentration and microcracking, and finally crack coalescence to fracture. The yield strength is defined as "the strength at which the plastic deformation starts", i.e. it should correspond to the first initiation of any easy slip system. However, for the convenience of practical measurement, an off-set plastic deformation value is defined, usually 0.2%. Therefore, σ_y value depends on both the initiation and the spreading of the slip systems. In this case, if the increasing temperature causes deeper Peierls valley or easier resplitting of superdislocations into noncoplanar configurations which are much more difficult to move, the stress level will be higher for the corresponding off-set strain level. The major difference between single crystal material and polycrystalline material is that, in the latter case, the grain boundaries (and/or interfaces in the case of multi-phases) play an important role in plastic deformation and this role becomes increasingly important with increasing temperature. It is well known that, for metallic materials, strength at elevated temperature is very much related to the strength of grain boundaries and the volume fraction of grain boundaries. In polycrystalline material, the cohesive force between grains gradually decreases with increasing temperature, and the plastic deformation transfers from the interior of grains to grain boundaries. Strain hardening inside the grains will accelerate the transfer of the deformation process. Therefore, although all of the strengthening factors responsible for the stress anomalies in single crystal intermetallic material are active in polycrystalline materials, their effect may not be reflected by increasing off-set yield strength. Instead, σ_y will decrease for activation of slip at grain boundaries (or interfaces).

It should be mentioned that the increase in the ultimate strength as the temperature increases is related to the increased ductility of the material at elevated temperature. The RT ductility is 1% and the ductility at 650°C and 760°C is 3%. The increase in ductility allows higher strain hardening to occur inside samples.

Figure 4.15 shows fractographs from a elevated temperature (760°C) tensile tested sample. The ridge-like and pit-like morphology is a major feature for elevated temperature tested fracture surface and "cracking through lamellae" mode is also observed. The morphology of fractured surface is influenced by the test temperature. Harry A. Lipsitt et al. (134) indicates that, at 700°C, the fracture surfaces show both cleavage and scattered indications of ductile fracture, however, the major change is in the propensity for separation at the grain boundaries.

4.4. Effects of Phase Constituents on Plastic Deformation of 48-2-2 TiAl Alloy

As mentioned in Chapter 1, γ -based TiAl alloys can be heat treated into various microstructures. The most common microstructures are single phase, duplex, and fully-transformed. It is generally believed that duplex structure has higher ductility than both single phase and fully transformed structure. Huang and Hall's results (58) indicate that samples with 100% equiaxed γ grains show 1% or less tensile ductility. The same result can be drawn from the Al at.% versus ductility curve (Figure 1.4). As alloy composition moves toward high Ti side, for example from 52 at.% Al to 48 at.% Al, the ductility increases. It seems reasonable to attribute this improvement to the appearance of α_2 phase, because in the binary Ti-Al phase diagram (Figure 1.3), this region corresponds to the transition from single γ -phase area to duplex $\gamma + \alpha_2$ area. Additional support for this conclusion is the fact that α_2 -based alloys are usually more ductile than γ -based alloy, as shown in Table 1.2. This conclusion also implicates that the greater the proportion of α_2 phase, the higher the ductility. However, one fact which conflicts with this conclusion is that

when the Al content is less than 48 at.%, the ductility decreases with decrease in Al content (or increase in α_2 volume fraction), as shown in Figure 1.4. Also, Kwai S. Cahn and Young-Won Kim (124) have obtained 3.7% ductility in Ti-47Al-2.6Nb-2(Cr+V) with fine, equiaxed γ grains with only small amounts of α_2 phase in particle and thin plate forms. Their result does not fit the conclusion. Obviously, it is important to understand the role of α_2 phase in plastic deformation of the alloy so further decisions in alloy design and heat treatment parameters can be made to improve its RT ductility.

Plastic deformation in polycrystalline materials comes from three major mechanisms: defect initiation and motion, interface (boundary) movement and mass transportation. The first two, especially the defects initiation and movement, dominate room temperature deformation. To get higher plastic deformation, first of all, the deformation units, such as single phase γ grain and γ/α_2 plates, should be able to undertake higher deformation without generating cracks. This requires 1) enough easy slip systems; 2) these system are active; 3) high mobility of the defects generated from these system and 4) less resistance to the defects movement. Secondly, the deformation compatibility among deformation units must be good. This can be reached by 1) activation of sub-easy slip system; 2) penetration of defects across the phase boundaries and grain boundaries and 3) interface movement to relieve and transmit localized stress and strain. By using TEM, deformation induced defect configurations and the structure of γ/α_2 interface were studied to understand the roles of these two phases in the RT ductility. Attention was paid to the function of α_2 in the deformation process and its contribution to RT ductility of the alloy. Conclusions drawn from this study supported the bond theory (Section 1.5.2.) in the interpretation of the effect of Al/Ti ratio and Cr addition on RT ductility of the alloy (Figure 1.4.). It was also demonstrated that with a fixed composition, the amount of α_2 phase could be adjusted by controlling heat treatment parameters.

4.4.1. Defect Configurations in Deformed Samples

Three major defects were observed in this study: dislocations, stacking faults and twins. Figure 4.16 shows a typical dislocation configuration in deformed γ matrix. Near the grain boundary, dislocations are tangled together and the density is high. Inside the grain, dislocations are nearly parallel and the density is low. Figure 4.17 shows a typical defect feature in the lamellar structure, i.e. twins and a few dislocations in the γ plates with very low defect density in α_2 plates. It can be clearly seen that twins are generated along certain crystal orientations. Figure 4.18 shows the interaction between a row of dislocations and a stacking fault. Note that there are twelve fringes before and eighteen fringes after the reaction. Six dislocations in the row joined the reaction. Each of these six dislocations reacts with only one fringe in every other order. Figure 4.19 shows two stacking faults with non-regular geometry. Figure 4.20 is a dislocation network in deformed γ phase.

It is found that the defect configuration and density have a close relation to the phase constituent. Stacking faults and twins are often observed in the lamellar structure, as shown in Figure 4.21. On the other hand, dense dislocations are the major product of the plastic deformation in equiaxed γ -grains, as shown in Figure 4.22. At the center of the grain, there are several rows of dislocations and dislocations are tangled together near the grain boundary. This implies that dislocations have some mobility although the resistance to slip is strong. Figure 4.23 is another defect configuration from the lamellar structure. It shows that defects are mainly concentrated in γ -layers and defect density in α_2 -layers is low, i.e. α_2 phase itself has little direct contribution to plastic deformation of the alloy.

4.4.2. Function of α_2/γ Interface

Accompanying the appearance of the lamellar structure, two features of the microstructures which may have important influences on the deformation are observed. One is the α_2 phase. Another one is the α_2/γ interface. Fractographic examination indicates that, in the lamellar structure, fracture is caused mainly by a "cracking through lamellae" mechanism. Delamination of α_2/γ interfaces happens when the grain size is large, i.e. coarse lamellar structure and wide plates. In that situation, the stress concentration is easily established by external forces. From TEM micrographs, two noticeable facts are found: the density of deformation induced defects in the lamellar structure is lower than that in the single phase γ grain, and within the lamellar structure, γ plates usually have higher defect density than α_2 plates. It seems that this may be related to the existence of α_2/γ interfaces because these interfaces may act as barriers to dislocation penetration.

Both α_2 and γ phases have long range ordered crystalline structures, as shown in Figure 1.2. Figure 4.24 is the selected area diffraction (SAD) pattern from α_2/γ interface which indicates the orientation relationship between these two phases is $(0001)_{\alpha_2} // (111)_{\gamma}$, $[11\bar{2}0]_{\alpha_2} // [1\bar{1}0]_{\gamma}$. The overlapped lattice structure is shown in Figure 4.25 (139). With the above information, the mismatch at α_2/γ interfaces can be calculated as follows:

The γ -phase has FCT crystal structure ($a=0.4005$ nm, $c=0.4070$ nm) and the α_2 phase has HCP structure ($a=0.5782$ nm, $c=0.4629$ nm) (107). With the known orientation relationship (135-139):

$$\begin{aligned} &(111)_{\gamma} // (0001)_{\alpha_2} \\ &[1\bar{1}0]_{\gamma} // [11\bar{2}0]_{\alpha_2} \end{aligned}$$

the mismatch ($\Delta d/d$) can be calculated as:

$$d_{[11\bar{1}0]\gamma} = 1.414 \times 0.4005 / 2 = 0.2832 \text{ (nm)} \quad (4.1)$$

$$d_{[11\bar{2}0]\alpha_2} = 0.5782 / 2 = 0.2891 \text{ (nm)} \quad (4.2)$$

$$\frac{\Delta d}{d} = \frac{d_{[11\bar{2}0]\alpha_2} - d_{[11\bar{1}0]\gamma}}{d_{[11\bar{2}0]\alpha_2}} = 0.02 \quad (4.3)$$

The number of atom planes between two interface dislocations is

$$N = \frac{d_{[11\bar{1}0]\gamma}}{d_{[11\bar{2}0]\alpha_2} - d_{[11\bar{1}0]\gamma}} = 48 \quad (4.4)$$

and the distance between two interface dislocations is

$$D = N \times d_{[11\bar{1}0]\gamma} = 14 \text{ (nm)} \quad (4.5)$$

Figure 4.26 shows the α_2/γ interface and dislocation arrangement on the phase boundary. The actual D value measured from TEM micrograph is between 30 to 50 nm. Mismatch value (2%) indicates that the coherence of this interface is close to perfect and hence it should not be a barrier to dislocation penetration. Differences in defect density between γ and α_2 should be related to the defect activity inside these phases, i.e. the activation and slip of dislocations in γ are easier than in α_2 .

4.4.3. Function of γ Phase

TEM examination indicates that γ phase has relatively high ductility. The fact that the duplex structure has a higher ductility than the 100% equiaxed single γ phase structure is related to the improved deformation ability of the γ phase. The following calculation is aimed at explaining how the ductility of the γ phase is enhanced.

With a fixed total Al content, the effect of α_2 volume fraction on the Al content γ -phase can be estimated by the following calculation.

Assuming

1. the chemical formula of α_2 is Ti_3Al ;
2. the average content of Al (at. %) is x ;
3. the content of Al (at. %) in γ -phase is y ;
4. the required volume fraction of α_2 phase is z ;
5. consider 100 total atoms.

The crystal parameters are known as:

$$\alpha_2: a=0.2891 \text{ nm}$$

$$c=0.4629 \text{ nm}$$

$$\gamma: a=0.4005 \text{ nm}$$

$$c=0.4070 \text{ nm}$$

So the cell volume is:

$$\begin{aligned} V_{\alpha_2} &= a^2 c \times \cos 30 \\ &= 0.033505 \text{ nm}^3 \end{aligned} \quad (4.6)$$

$$\begin{aligned} V_{\gamma} &= a^2 c \\ &= 0.065283 \text{ nm}^3 \end{aligned} \quad (4.7)$$

Then

$$z = \frac{\frac{N_{\alpha_2} \times V_{\alpha_2}}{n_{\alpha_2}}}{\frac{N_{\alpha_2} \times V_{\alpha_2}}{n_{\alpha_2}} + \frac{N_{\gamma} \times V_{\gamma}}{n_{\gamma}}} \quad (4.8)$$

where N_{α_2} and N_{γ} are numbers of atoms in α_2 and γ phases, n_{α_2} and n_{γ} are numbers of atoms per-cell volume α_2 and γ phases, respectively. Combining with:

$$N_{\alpha_2} + N_{\gamma} = 100 \quad (4.9)$$

N_{α_2} can be calculated with a given z value. Finally x can be obtained by solving the following equation with a given y value:

$$y = \frac{100x - N_{\alpha_2(AI)}}{100 - N_{\alpha_2}} \quad (4.10)$$

where $N_{\alpha_2(AI)}$ is the number of Al atom in the α_2 phase. For example, if $y=47.5\%$ and $z=10\%$, $x=46.46\%$.

The calculated results indicate that, for a Ti-48Al (at.%) alloy, if there is 10% volume fraction α_2 in the material, the Al content in γ is lower than the equilibrium value (about 51-52 at.%Al at RT, as shown in Figure 1.3), i.e. γ grains are supersaturated with Ti atoms. According to bond theory, with supersaturated Ti atoms, the M d-Ti d bond is enhanced. Based on the above analysis, one of the major factors which enhances the plastic deformation ability of γ -phase in duplex structure is the increased number of d-d interactions. This conclusion is supported by some researchers' work. It is reported (58,123) that the transition from single phase

to duplex microstructure causes a change in the deformation mechanism. In alloys of composition 48-50 at. % Al, the major substructures are mobile $1/2 \langle 110 \rangle$ unit dislocations, faults and twins. Superdislocations are essentially absent. This implies that the mobility of the whole slip system in γ -TiAl increases as Al content decreases. This conclusion is also supported by the high density of dislocations in deformed γ -phase in this study.

4.4.4. Function of α_2 Phase

It is expected that when the microstructure changes from 100% equiaxed single γ -phase grain to the duplex structure, the appearance of α_2 phase and hence the α_2/γ interface should have some effects on the RT mechanical behavior of the alloy. When α_2 phase exists in α_2 -based Ti₃Al alloys, such as the so called Super α_2 alloy containing Ti-25Al-10Nb-3V-1Mo (at. %), its RT ductility is better than the γ -based TiAl alloy. Naturally, it should have higher ductility than the γ phase. Two possible reasons may be responsible for its lower ductility when it appears in lamellar structure of γ -based TiAl alloy: 1) The α_2 phase has higher oxygen solubility than γ phase (59). The high oxygen content makes both the initiation and further slip of dislocations in the α_2 phase more difficult; 2) Its higher yield strength prevent its participation in deformation. As shown in Table 1.2, the yield strength of the α_2 -based alloys is even higher than the tensile strength of the γ -based alloys. Therefore, the α_2 is more rigid than the γ at room temperature. Although by itself, it has little contribution to the deformation directly, it has beneficial effects and assists the deformation of γ . High oxygen content is a common feature in Ti alloy. The segregation of oxygen to α_2 phase lowers the average oxygen content in γ and hence decreases the resistance to dislocation movement. Also, the appearance of α_2 effectively decreases the average grain size, which is clearly favorable for deformation. Even α_2 itself, under suitable conditions, will show significant deformation. Figure 4.27 shows a dislocation network in α_2 phase which implies

higher plastic deformation. The α_2 has both beneficial and detrimental effects on the RT ductility of γ -based TiAl alloys. This leads to the appearance of the peak value of ductility in Figure 1.3. The controlling factors here are volume fraction, distribution and geometry of α_2 phase. Among these factors, the volume fraction is the most important one. Y.-W. Kim (59) believes that 5-15% phase volume ratio of α_2/γ is optimal for achieving high ductility in γ -based alloys (Table 1.4).

4.4.5. Volume Fraction Control of α_2 Phase

There are basically two methods, alloying addition or heat treatment, for controlling the volume fraction of α_2 in γ -based alloys.

Additions of elements such as Mn reduce the Al content in γ phase, which implies that the $(\alpha_2 + \gamma)/\gamma$ phase boundary leans toward Ti-M line in the isothermal section of the ternary Ti-Al-M phase diagram (59). Volume fraction of α_2 phase decreases by the addition of Mn and V (78). This may improve RT ductility because more γ phase participates plastic deformation. It is also known (72) that Cr additions tend to depress the α transus and increase its Al concentration. This leads to decreases in the volume fraction and thermal stability of transformed α_2 laths. As a result, coarsened γ regions form in primary α grains which can deform without hindrance of α_2 laths.

In the present work, it is found that, in 48-2-2 alloy or similar γ -based TiAl systems, the Ti content in γ can be raised by suitable heat-treatment which may produce γ with super-saturated Ti atoms. As shown in Figure 1.3, above the eutectoid line, the solubility of Ti in γ increases as temperature decreases. As long as full homogenization can be reached, the lowest heat treatment temperature is preferred. The function of such treatment is similar to the substitution of transition elements for Al atoms. Figure 4.28 shows back scattered electron images of two 48-

2-2 samples with different heat-treatments. Comparing with the structure in Figure 4.28 (a), the structure in Figure 4-28 (b) has smaller grain size ($\sim 24 \mu\text{m}$ to $110 \mu\text{m}$), less α_2 phase (16% to 25%) and less volume fraction of lamellar structure.

Again, the major disadvantage which stops engineering application of TiAl is its poor RT ductility (1-3% in elongation) although its HT ductility is quite good. This is also the major obstacle for using TiAl in jet engines. The brittle behavior of γ -based TiAl alloy at RT is due to its bond type and ordering status. Therefore it can not reasonably be expected to improve significantly with either alloy addition or heat treatment.

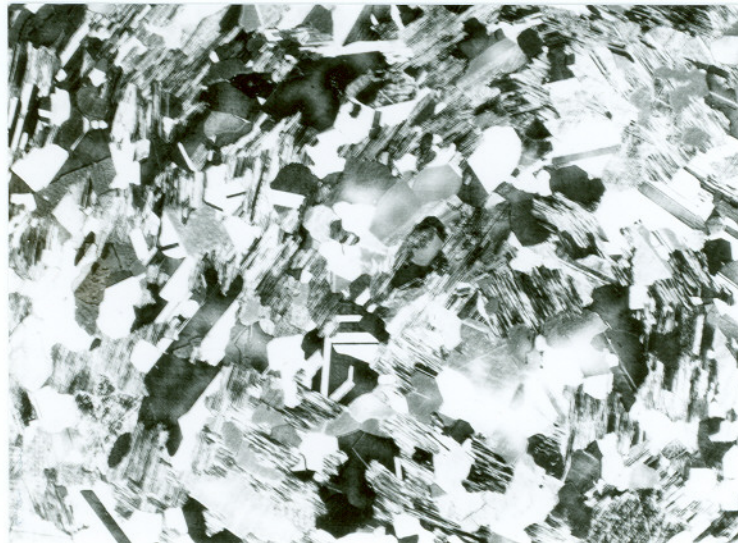
It is well known that, in most metallic systems such as the matrix of Superalloy X, the combining force is metallic bond. However, intermetallics such as TiAl may have a mixture of two different types of bond as their combining forces and they usually have a long range ordered atomic distribution. Whenever, covalent bond plays the major role, some metallic characteristics of mechanical and physical behavior will diminish and instead, some compound characteristics become stronger. For example, Superalloy X, like many other alloys, has quite good ductility at room temperatures due to metallic bond. TiAl, on the other side, has a poor RT ductility although it has many superior high temperature mechanical and physical properties. Its advantages and disadvantages reflect two sides of a conflict. It is mentioned above that addition of alloying elements with d covalent bond electrons can improve RT ductility. But there is concern that alloying to improve ductility may alter the fundamental characteristics of the intermetallics to such an extent that their other attractive properties, such as density, modulus and elevated temperature strength, may be seriously compromised. Thus it is important to seek design solutions to ameliorate the effects of brittleness in addition to the ongoing modifications of the materials to make them less brittle (65). Improvement in RT ductility of γ -based TiAl may cause a loss in some of its advantages. For example, β phase is more ductile than γ phase

and it is possible to introduce this phase in γ -based TiAl alloys for increasing ductility. However, β phase is not an ordered phase, its appearance may cause decreases in elastic modulus and high temperature strength. An optimized balance, which is represented by enabling the engineering application of this material at the least loss of its superior properties, is the aim of the current researches in the field. Evolution in design concepts is also necessary not only for using this material but also for the employment of other potential alternatives such as intermetallic-matrix composites and ceramics which are facing same mechanical limitation.



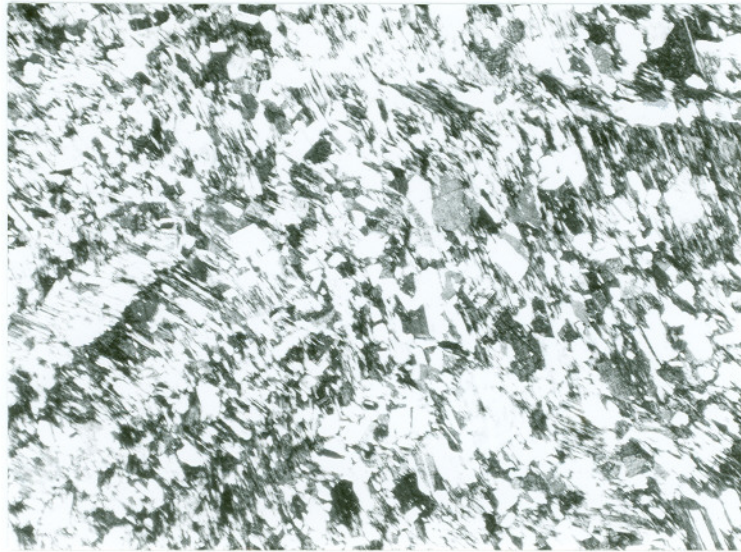
600 μm

Figure 4.1 Microstructure of the sample with slow solidification rate



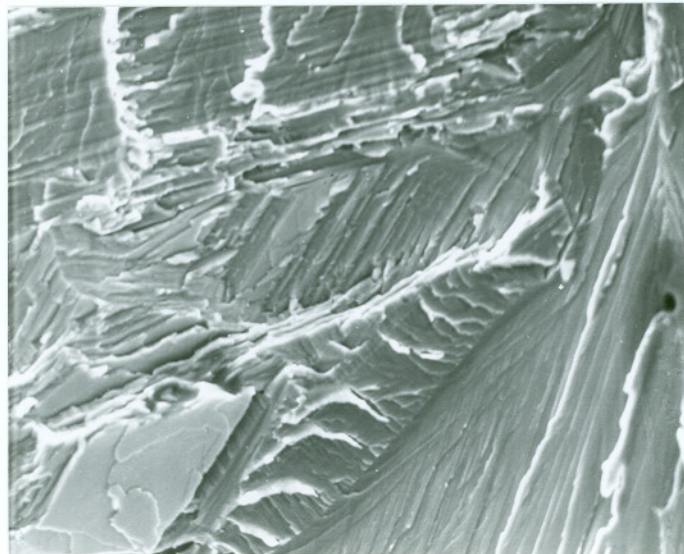
600 μm

Figure 4.2 Microstructure of the sample with medium solidification rate



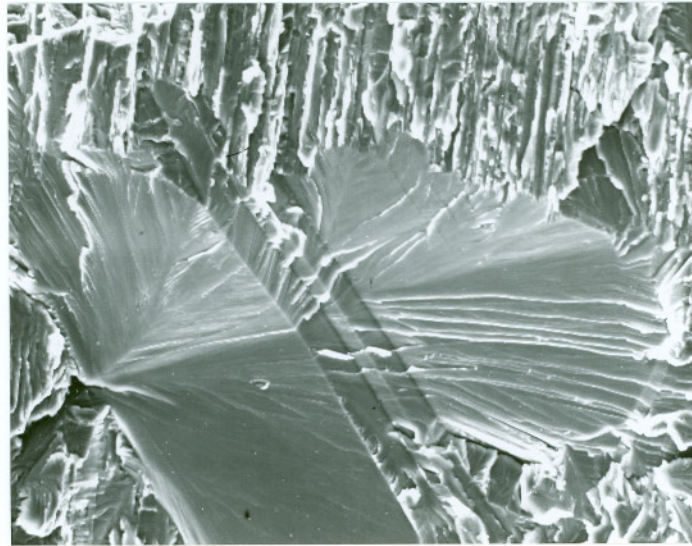
600 μm

Figure 4.3 Microstructure of the sample with fast solidification rate



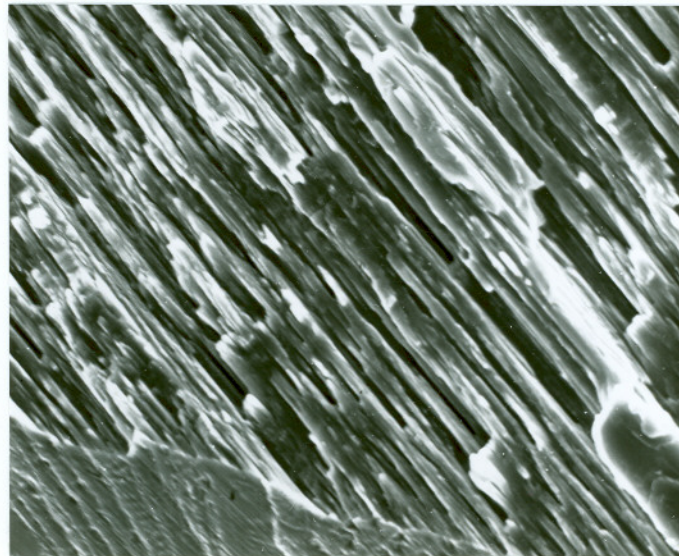
17 μm

Figure 4.4 Fractograph: River pattern



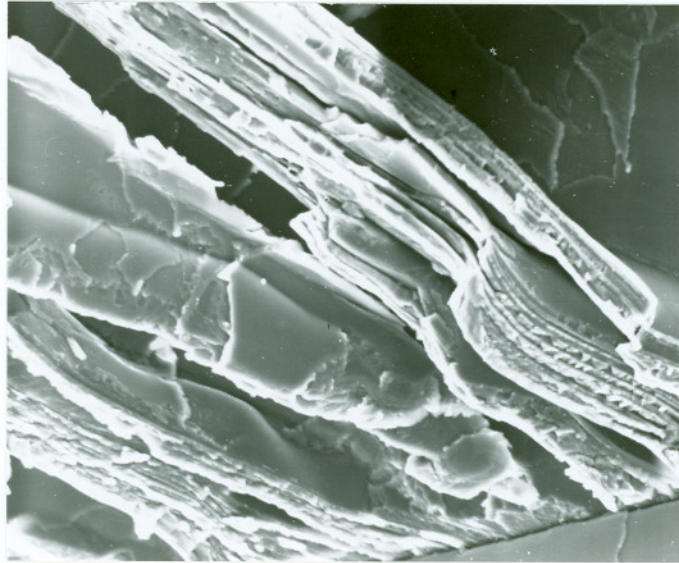
60 μm

Figure 4.5 Fractograph: Cleavage along certain crystal plane



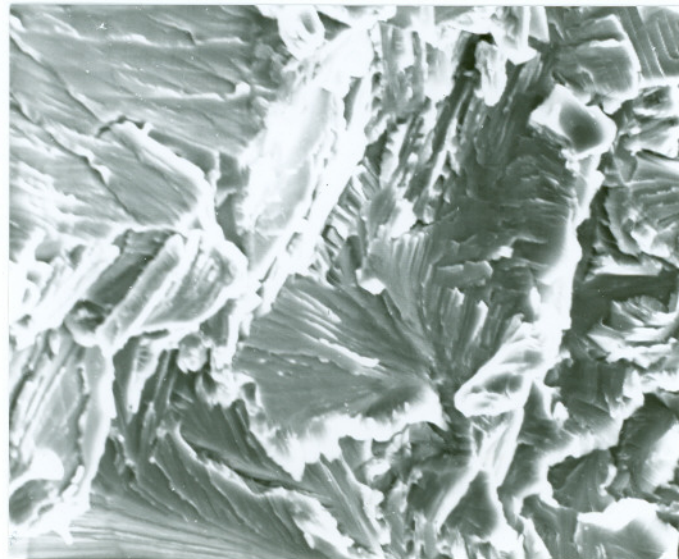
30 μm

Figure 4.6 Fractograph: Cracking through lamellar area



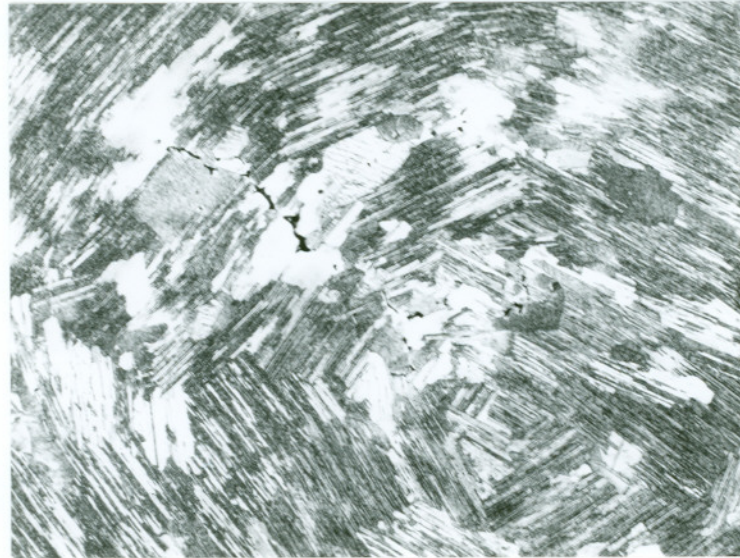
60 μm

Figure 4.7 Fractograph: Delamination of α_2/γ interfaces



30 μm

Figure 4.8 Fractograph: Cleavage



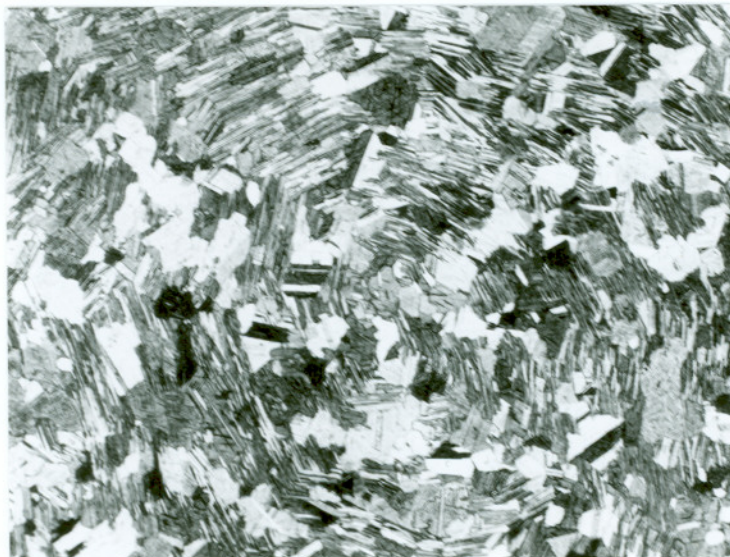
300 μm

Figure 4.9 Microstructure of the As-Cast sample



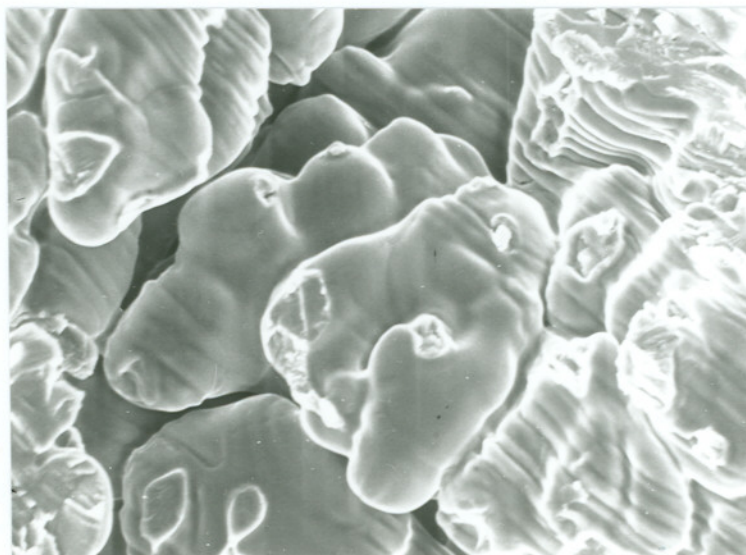
300 μm

Figure 4.10 Microstructure of the As-HIP sample



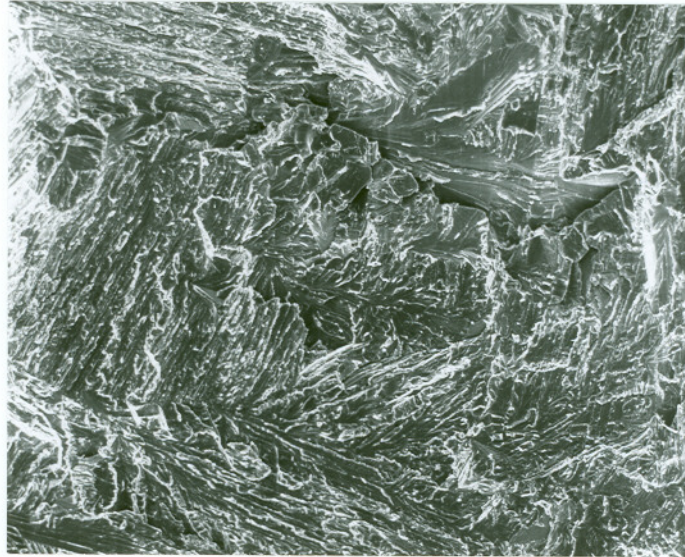
600 μm

Figure 4.11 Microstructure of the HIP + HT sample



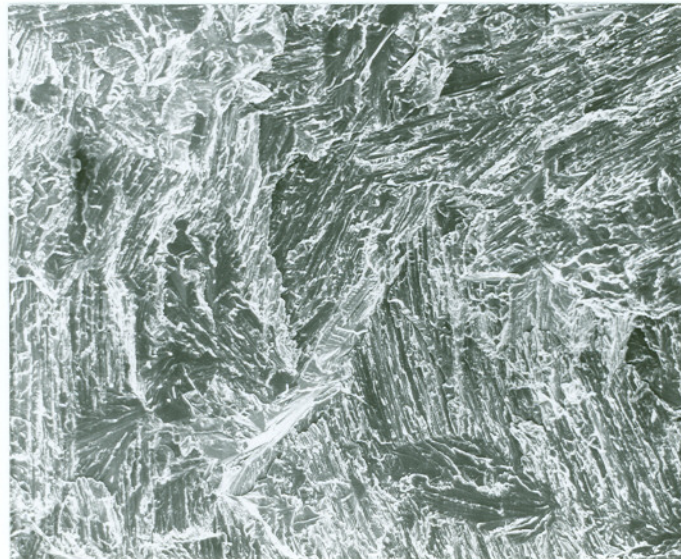
54 μm

Figure 4.12 Fractograph of the As-Cast sample



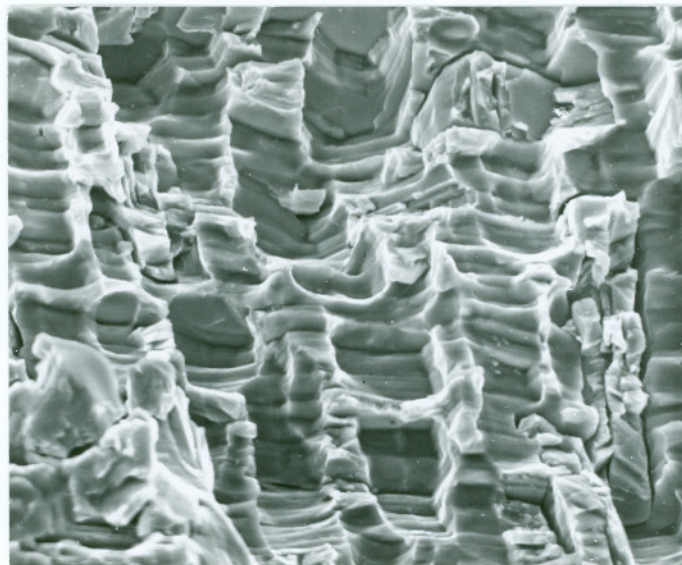
300 μm

Figure 4.13 Fractograph of the As-HIP sample

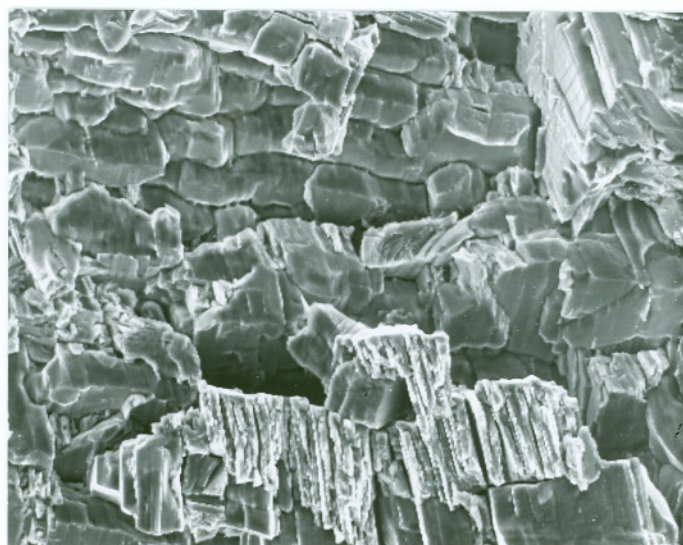


300 μm

Figure 4.14 Fractograph of the HIP+HT sample

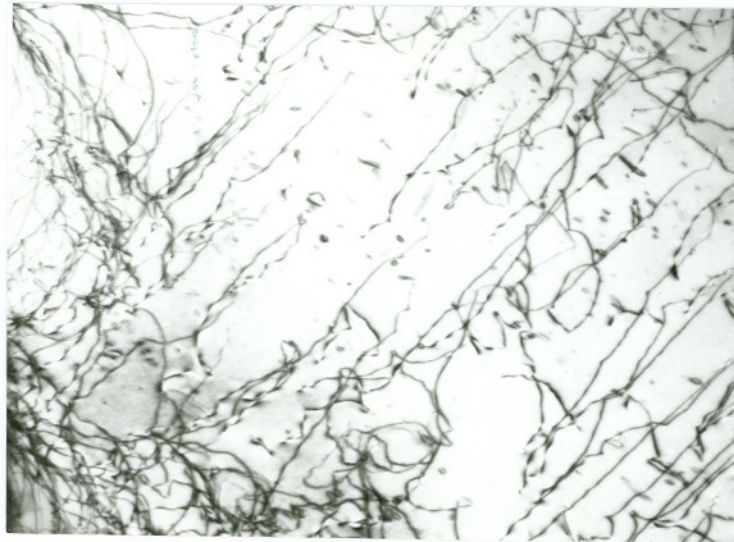


(a) 30 μm



(b) 60 μm

Figure 4.15 Fractographs of the sample tested at 760 °C



1.4 μm

Figure 4.16 Dislocation configuration in deformed γ phase, TEM



2.7 μm

Figure 4.17 Twins in deformed lamellar structure, TEM

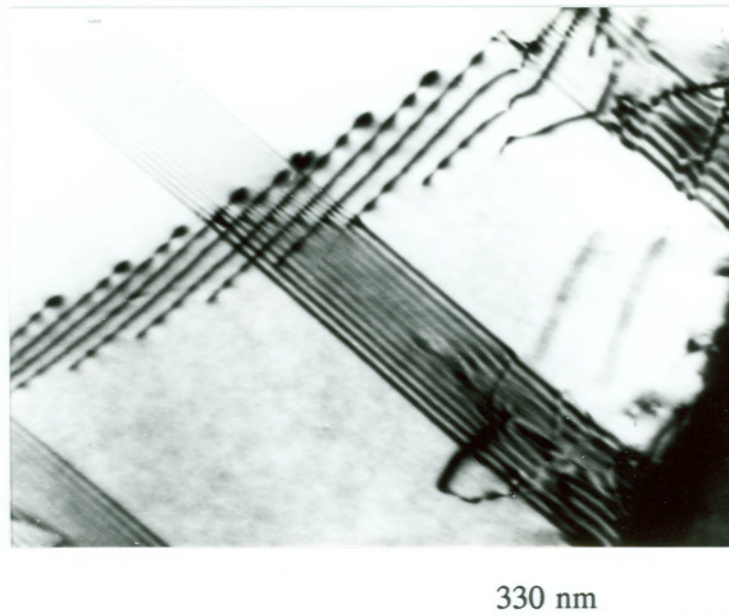


Figure 4.18 Interaction between a row of dislocations and a stacking fault, TEM

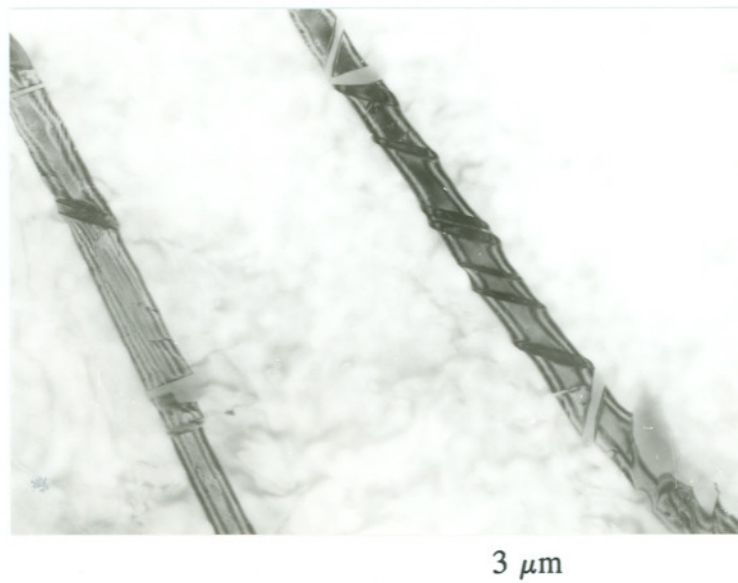
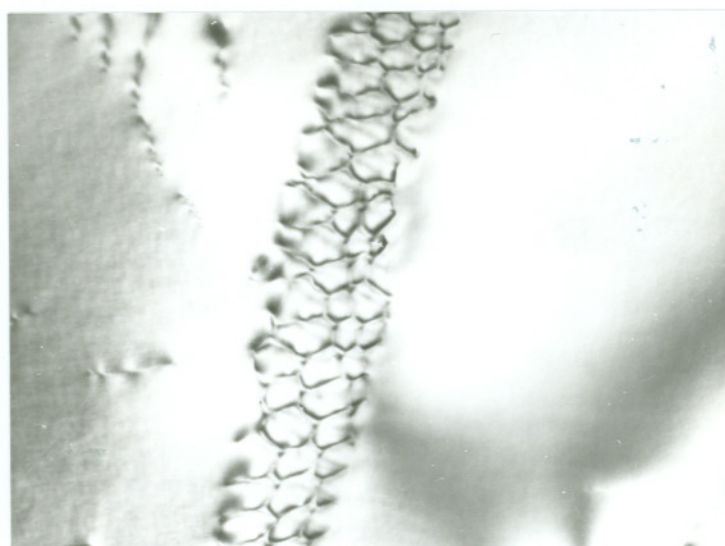


Figure 4.19 Stacking faults in γ -phase, TEM



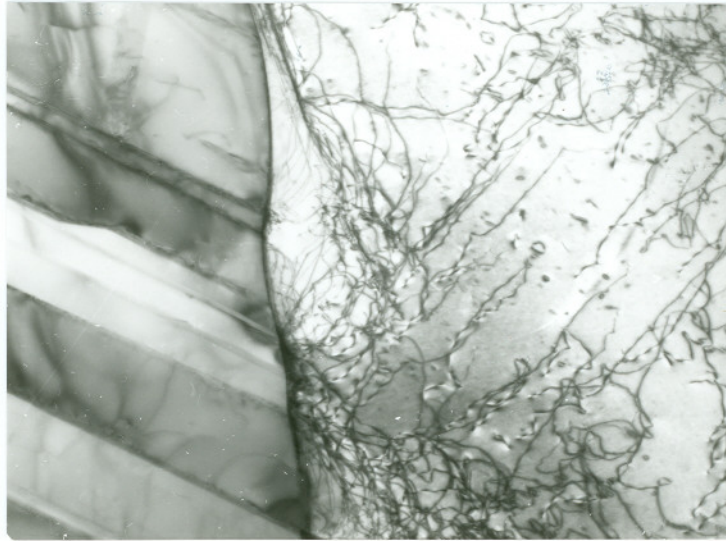
500 nm

Figure 4.20 Dislocation network in deformed γ -phase, TEM



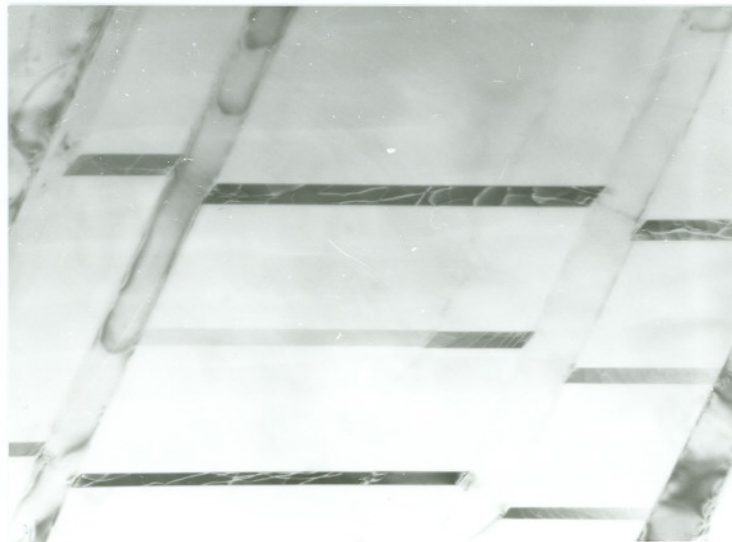
1.4 μm

Figure 4.21 Defect configurations in deformed lamellar structure, TEM



1.8 μm

Figure 4.22 Tangled dislocations near grain boundary and parallel dislocations in γ grain, TEM



0.9 μm

Figure 4.23 Defects configuration in deformed lamellar structure, TEM

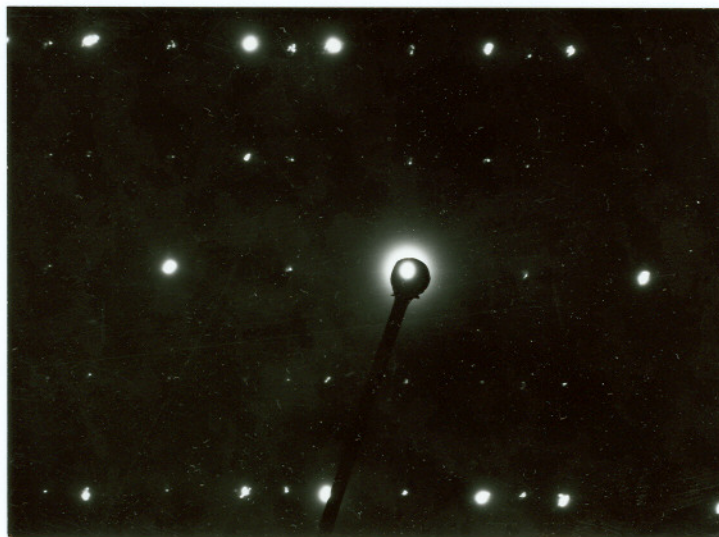


Figure 4.24 SAD pattern from α_2/γ interface

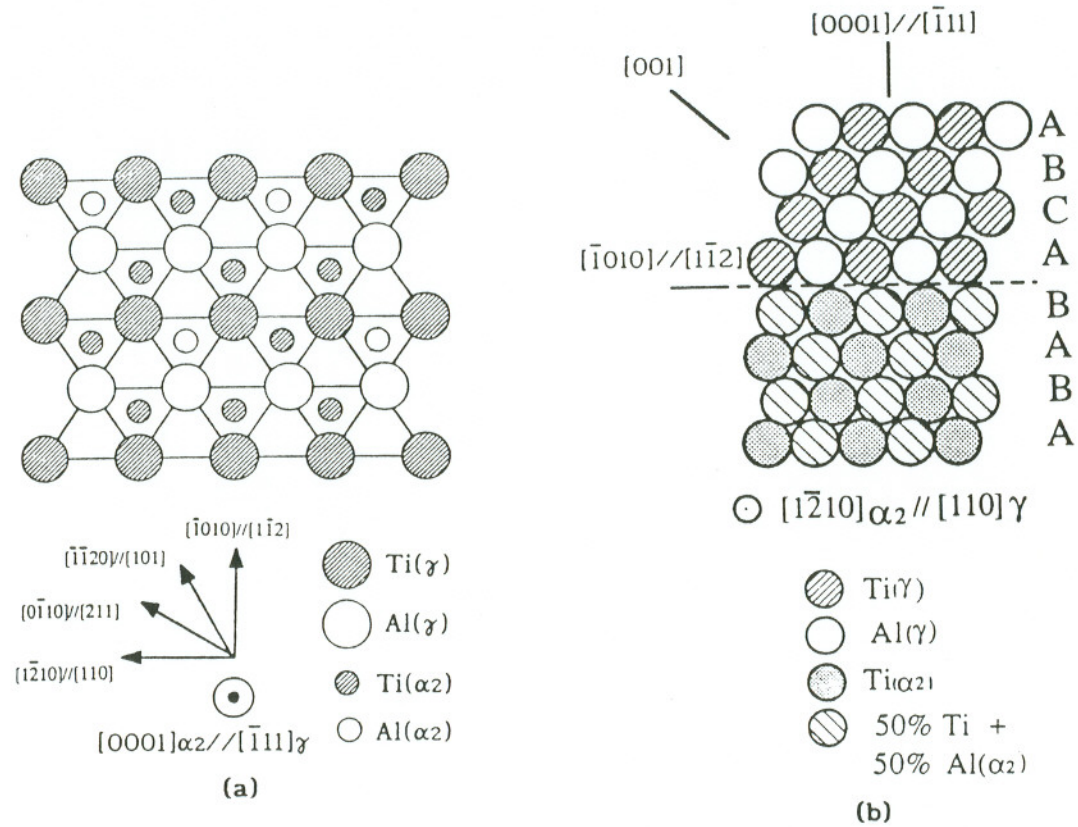
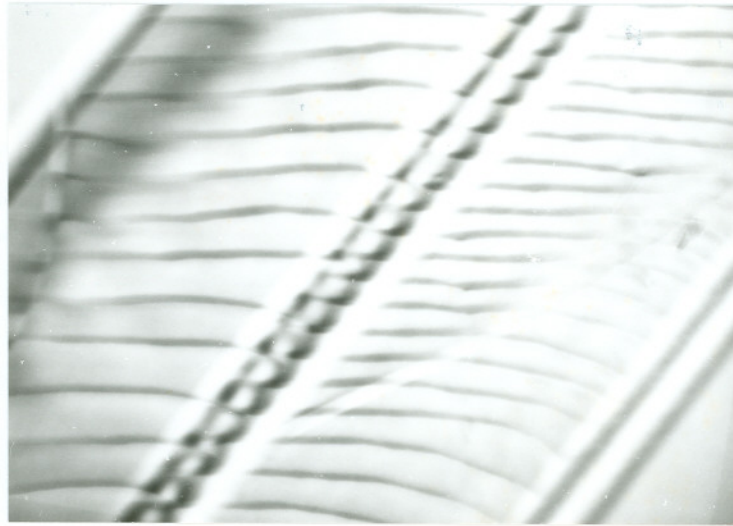
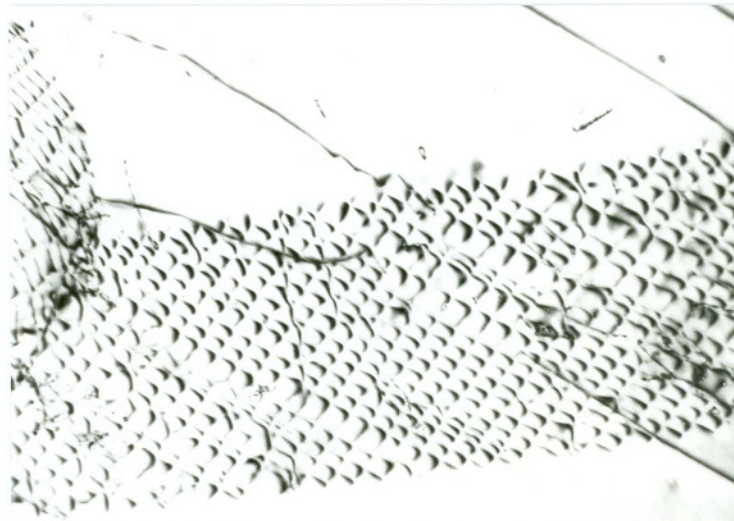


Figure 4.25 Atomic arrangement on α_2/γ interface $[0001]_{\alpha_2}/[\bar{1}\bar{1}\bar{1}]_{\gamma}$ (a) along $[0001]_{\alpha_2}/[111]_{\gamma}$ direction and (b) along $[1\bar{2}10]_{\alpha_2}/[110]_{\gamma}$ direction (139)



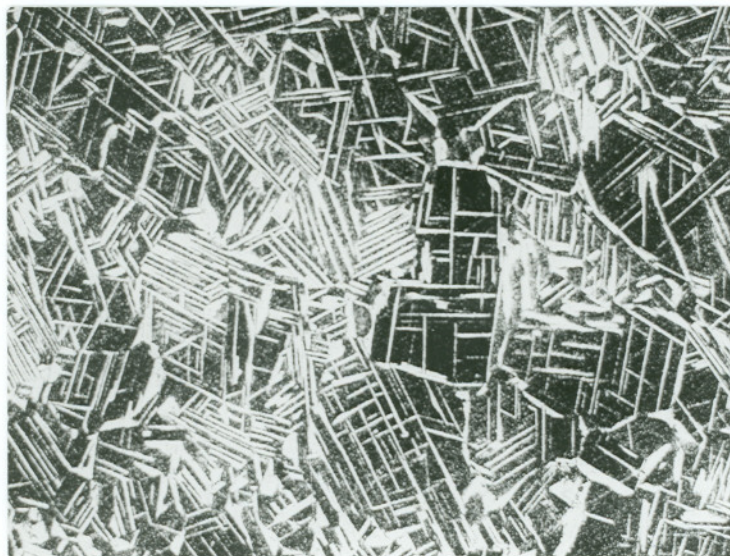
330 nm

Figure 4.26 Arrangement of dislocations along α_2/γ interface, TEM



500 nm

Figure 4.27 Dislocation network in deformed α_2 phase, TEM



(a) 140 μm



(b) 140 μm

Figure 4.28 Backscattered electron images of 48-2-2 samples with different heat treatment

CHAPTER 5

CONCLUSIONS AND SUGGESTIONS FOR FUTURE WORK

5.1. Conclusions

- (1) The creep test results show that, in Superalloy X, fine grain material has a lower high temperature ductility and a lower creep rate than the coarse grain material under the same testing conditions. Higher creep rate in the coarse grain material may be introduced by the non-uniform distribution of precipitates and lower yield and ultimate strength. Intra-dendrite regions creep faster because the nearly precipitate-free matrix is easily deformed.
- (2) For Superalloy X, constant K experiments and fatigue experiments (with and without holding times) reveal much lower fracture toughness of the fine grain material in comparison with the coarse grain material. This result is attributed to the δ precipitate-rich area that is usually selected as crack initiation spots and crack propagation paths. Unlike the coarse grain samples, in the fine grain samples, there are no ppt-free regions. Therefore the fine grain samples have lower resistance to crack propagation. The failure processes of the fine grain material under testing conditions are evidently time dependent in contrast to the coarse grain material.
- (3) The resistance to creep crack growth of Superalloy X samples with different grain size does not correspond with their resistance to creep deformation. A progressive increase in resistance to crack growth is indicated with an increase

in material ductility.

- (4) Increase in solidification rate improves the room temperature ductility of γ -based TiAl alloy. Such improvement may come from several sources such as a refined microstructure, more uniform element distribution, a more ductile γ -phase and more activation of easy slip systems.
- (5) The γ/α_2 volume fraction ratio, Ti/Al element ratio in γ -phase and morphology of phases in 48-2-2 TiAl alloy can be altered with different post-cast heat treatment procedures.
- (6) The initiation and propagation of dislocations in single phase γ grains is responsible for the major part of plastic deformation. Planar defects like stacking faults and twins also play important roles in alloy deformation. The α_2 phase indirectly assists the deformation procedure but it has little direct contribution to RT ductility.
- (7) The delamination of the γ/α_2 interface is caused by stress concentration build up during tensile testing because of the difference in ductility between these two phases.

5.2. Suggestions for Future Work

Investigation on structure-property relationships of Superalloy X indicates that the appearance of δ phase plays an important role in the high temperature mechanical behavior of the material. To further improve its high temperature properties, the distribution and volume fraction of δ phase has to be controlled. There are two possible methods to do this: 1) addition of alloy elements which can enhance the stability of γ' phase and 2) modification of heat treatment to reduce the direct

precipitation of δ phase.

For the 48-2-2 γ -based TiAl alloy, in the near future, the improvement of RT ductility of γ -based TiAl alloys will still be a major task. Based on results from this study, the following future work is suggested:

- (1) Optimization of the heat treatment conditions and structure parameters, especially the grain size, α_2 volume fraction and morphology.
- (2) Adjustment of alloying elements to produce high mobility dislocations.
- (3) Improvement of melting method and solidification parameters to get uniform metallurgical structure with less oxygen content.

REFERENCE

1. T.Khan et al., Intermetallics for Structural Applications, *Proceeding of high temperature Materials for Power Engineering*, Edited by E. Bachelet et al., Kluwer Academic Publishers, 1990, 1533-1558.
2. Steven Ashley, Tough Materials for Tomorrow's Engines, *Mechanical Engineering*, **113(12)**, 1991, 49-52.
3. R.L. Fleisher, High-strength, High-temperature Intermetallic Compounds, *J. Mater. Sci.*, **22(7)**, 1987, 2281-2288.
4. David L. McDanel, Tito T. Serafini and James A. DiCarlo, Polymer, Metal, Ceramic Matrix Composites for Advanced Aircraft Engine Applications, *Advanced Composites (Conference Proceedings)*, ASM, 1985, 263-275
5. Dennis M. Dimiduk and Daniel B. Miracle, Directions in High Temperature Intermetallics Research, *High-Temperature Ordered Intermetallics Alloys III*, Edited by C.T. Liu et al., Mat. Res. Soc. Symp. Proc., **133**, 1989, 349-359.
6. Hugu R. Gray and Carol A.Ginty, NASA's High-Temperature Engine Materials Program for Civil Aeronautics, *JOM*, **44(5)**, 1992, 12.
7. P. Prasad Rao and Kris Tangri, Yielding and Work Hardening Behaviour of Titanium Aluminides at Different Temperatures, *Mater. Sci. & Engng. A***132**, 1991, 49-59.
8. Masaharu Yamaguchi and Haruyuki Inui, TiAl Compounds for Structural Applications, *Structural Intermetallics*, Edited by R. Darolia et al., The Mineral, Metals & Materials Society, 1993, 127-142.
9. D.S. Shih et al., The Microstructural Dependence of Mechanical Properties of Ti-48Al-2Cr-2Nb, *Microstructure/Property Relationships in Titanium Aluminides and Alloys*, Edited by Y.W. Kim and Rodney R. Boyer, The Minerals, Metals & Materials Society, 1991, 135-148.
10. S.M. Jeng, J.-M. Yang, Mechanical Behavior of SiC Fibre-reinforced Titanium/titanium Aluminide Hybrid Composites, *J. of Mater. Sci.*, **27(20)**, 1992, 5357-5364.
11. Dennis M. Dimiduk et al., Recent Progress on Intermetallic Alloys for Advanced Aerospace Systems, *ISIJ International*, **31(10)**, 1991, 1223-1234.

12. Kamleshwar Upadhyaya, Ceramics and Composites for Rocket Engines and Space Structures, *JOM*, **44(5)**, 1992, 15.
13. D.M. Dimiduk, M.G. Mendiratta and P.R. Subramanian, Development Approaches for Advanced Intermetallic Materials-Historical Perspective and Selected Successes, *Structural Intermetallics*, Edited by R. Darolia et al., The Minerals, Metals & Materials Society, 1993, 619-630.
14. J.H. Westbrook, Structural Intermetallics: Their Origins, Status and Future, *Structural Intermetallics*, Edited by R. Darolia et al., The Minerals, Metals & Materials Society, 1993, 1-15.
15. C.M. Austin and T.J. Kelly, Development and Implementation Status of Cast Gamma Titanium Aluminide, *Structural Intermetallics*, Edited by R. Darolia et al., The Minerals, Metals & Materials Society, 1993, 143-150.
16. J. Wadsworth, T.G. Nieh, and J.J. Stephens, Recent Advances in Aerospace Refractory Metal Alloys, *International Materials Reviews*, **33(3)**, 1988, 131-150.
17. L. Krousiewicz, J. Ding, M.S. Kumosa, Micro- and Macro- Structural Aspects of Fatigue Crack Growth Behavior in Structure Casting Superalloys, Annual Progress Report to Precision Castparts Corp. and GE, August, 1991.
18. Matthew J. Donachie, Jr., Introduction to Superalloys, *Source Book of Superalloys*, Edited by Matthew J. Conachie, Jr., ASM, 1984, 3-15.
19. Stephen D. Antolovich and J.E. Campbell, Fracture Properties of Superalloys, *Source Book of Superalloys*, Edited by Matthew J. Conachie, Jr., ASM, 1984, 112-169.
20. N.A. Wilkinson, Technological Considerations in the Forging of Superalloy Rotor Parts, *Source Book of Superalloys*, Edited by Matthew J. Conachie, Jr., ASM, 1984, 234-247.
21. Gerhard Kienel, Vacuum Melting and Remelting Processes, *Metals Handbook*, Ninth Edition, **15**, ASM, 1988, 393-399.
22. J.W. Pridgeon et al., Principles and Practices of Vacuum Induction Melting and Vacuum Arc Remelting, *Source Book of Superalloys*, Edited by Matthew J. Conachie, Jr., ASM, 1984, 201-216.

23. S.J. Patel and I.C. Elliott, Trends in Clean Melting Technology for Ni-based Superalloys, *Proceeding of high temperature Materials for Power Engineering*, Edited by E. Bachelet et al., Kluwer Academic Publishers, 1990, 1757-1766.
24. A. Choudhury and F. Knell, Electroslag Remelting (ESR), *Metals Handbook*, Ninth Edition, **15**, ASM, 1988, 401-406.
25. H. Pannen and G. Sick, Plasma Melting and Casting, *Metals Handbook*, Ninth Edition, **15**, ASM, 1988, 419-425.
26. L.A. Jackman, Forming and Fabrication of Superalloys, *Source Book of Superalloys*, Edited by Matthew J. Conachie, Jr., ASM, 1984, 217-233.
27. Kempton H. Roll, History of Powder Metallurgy, *Metals Handbook*, Ninth Edition, **7**, ASM, 1988, 14-20.
28. Krister Torssell, High Performance Steel by Hot Isostatic Pressing - Processing, Applications and Perspectives, *Proceeding of High Temperature Materials for Power Engineering*, Edited by E. Bachelet et al., Kluwer Academic Publishers, 1990, 1513-1531.
29. Peter G. Bailey and Wilbur H. Schweikert, HIP Improves Castings, *Source Book of Superalloys*, Edited by Matthew J. Conachie, Jr., ASM, 1984, 342-346.
30. John M. Eridon, Hot Isostatic Pressing of Castings, *Metals Handbook*, Ninth Edition, **15**, ASM, 1988, 538-544.
31. L.W. Lherbier, Melting of Superalloys, *Source Book of Superalloys*, Edited by Matthew J. Conachie, Jr., ASM, 1984, 189-200.
32. G.H. Gessinger, Recent Developments in Powder Metallurgy of Superalloys, *Source Book of Superalloys*, Edited by Matthew J. Conachie, Jr., ASM, 1984, 277-285.
33. K. Schneider, Advanced Blading, *Proceeding of High Temperature Materials for Power Engineering*, Edited by E. Bachelet et al., Kluwer Academic Publishers, 1990, 935-954.
34. R. McCallum, Casting Critical Components, *Source Book of Superalloys*, Edited by Matthew J. Conachie, Jr., ASM, 1984, 286-291.

35. William A. Owczarski, Process and Metallurgical Factors in Joining Superalloys and Other High Service Temperature Materials, *Source Book of Superalloys*, Edited by Matthew J. Conachie, Jr., ASM, 1984, 369-400.
36. F.R. Morral, Wrought Superalloys, *Source Book of Superalloys*, Edited by Matthew J. Conachie, Jr., ASM, 1984, 20-40.
37. John F. Radavich, The Physical Metallurgy of Cast and Wrought Alloy 718, *Superalloy 718-Metallurgy and Applications*, Edited by E.A. Loria, The Minerals, Metals & Materials Society, 1989, 229-240.
38. J.K. Tien et al., Raising the High Temperature Limit of In718-- Designing Ticolloy, *Proceeding of High Temperature Materials for Power Engineering*, Edited by E. Bachelet et al., Kluwer Academic Publishers, 1990, 1341-1356.
39. S.K. Srivastava and M.F. Rothman, An advanced Ni-Mo-Cr Alloy for Gas Turbines, *Proceeding of High Temperature Materials for Power Engineering*, Edited by E. Bachelet et al., Kluwer Academic Publishers, 1990, 1357-1366.
40. G. Raisson, and J.H. Davidson, N18, A New Generation PM Superalloy for Critical Turbine Components, *Proceeding of High Temperature Materials for Power Engineering*, Edited by E. Bachelet et al., Kluwer Academic Publishers, 1990, 1405-1416.
41. H. Harada et al., Design of High Specific-strength Nickel-base Single Crystal Superalloys, *Proceeding of High Temperature Materials for Power Engineering*, Edited by E. Bachelet et al., Kluwer Academic Publishers, 1990, 1319-1328.
42. M. Gell, D.N. Duhl, and A.F. Giamei, The development of Single Crystal Superalloy Turbine Blades, *Source Book of Superalloys*, Edited by Matthew J. Conachie, Jr., ASM, 1984, 297-306.
43. K. Matsugi et al., High-temperature Properties of Single Crystal Superalloys Optimized by an Electron Theory, *Proceeding of High Temperature Materials for Power Engineering*, Edited by E. Bachelet et al., Kluwer Academic Publishers, 1990, 1251-1260.
44. J.E. Northwood, Improving Turbine Blade Performance by Solidification Control, *Source Book of Superalloys*, Edited by Matthew J. Conachie, Jr., ASM, 1984, 292-296.

45. F.S. Pettit and G.W. Goward, High Temperature Corrosion and Use of Coating for Protection, *Source Book of Superalloys*, Edited by Matthew J. Conachie, Jr., ASM, 1984, 170-186.
46. D. Driver, Materials and Process Directions for Advanced Aero-engine Design, *Proceeding of High Temperature Materials for Power Engineering*, Edited by E. Bachelet et al., Kluwer Academic Publishers, 1990, 883-902.
47. Stephen D. Antolovich, The Effect of Metallurgical Instabilities on the Behavior of IN 718, *Superalloy 718-Metallurgy and Applications*, Edited by E.A. Loria, The Minerals, Metals & Materials Society, 1989, 647-653.
48. Edward A. Loria, Thermal Stability of Superalloy 718 from a Compositional Viewpoint, *Proceeding of High Temperature Materials for Power Engineering*, Edited by E. Bachelet et al., Kluwer Academic Publishers, 1990, 1367-1375.
49. F. Schubert, Temperature and Time Dependent Transformation: Application to Heat Treatment of High Temperature Alloys, *Source Book of Superalloys*, Edited by Matthew J. Conachie, Jr., ASM, 1984, 71-101.
50. Venkat Seetharaman and Carl M. Lombard, Plastic Flow Behavior of a Ti-Al-Nb--Mn Alloy at High Temperatures, *Microstructure/Property Relationships in Titanium Aluminides and Alloys*, Edited by Y.W. Kim and Rodney R. Boyer, The Minerals, Metals & Materials Society, 1991, 237-251.
51. R.A. Varin and M.B. Winnicka, Plasticity of Structural Intermetallic Compounds, *Mater. Sci. & Engng.*, **A137**, 1991, 93-103.
52. C. McCullough, J. J. Valencia, C.G. Levi and R. Mehorabian, Phase Equilibria and Solidification in Ti-Al Alloys, *Acta Metall.*, **37(5)**, 1989, 1321-1336.
53. Harry A. Lipsitt, Dan Shechtman and Robert E. Schafrik, The Deformation and Fracture of TiAl at Elevated Temperatures, *Metall. Trans. A*, **6A(11)**, 1975, 1991-1996.
54. K.S. Chan and Y.-W. Kim, Influence of Microstructure on Crack-Tip Micromechanics and Fracture Behaviors of a Two-Phase TiAl Alloy, *Metall. Trans. A*, **23A(6)**, 1992, 1663-1677.
55. W.O. Soboyejo, D.S. Schwartz and S.M.L. Sastry, An Investigation of the Fracture Behavior of Gamma-Based Titanium Aluminides: Effects of

- Annealing in the $\alpha+\gamma$ and $\alpha_2+\gamma$ Phase Fields, *Metall. Trans. A*, **23A(7)**, 1992, 2039-2059.
56. J.L. Murray, The Al-Ti (Aluminum-Titanium) System, *Phase Diagrams of Binary Titanium Alloys*, Edited by Joanne L. Murray, ASM International, 1987, 12-24.
 57. Young-Won Kim, Recent Advances in Gamma Titanium Aluminide Alloys, *High-Temperature Ordered Intermetallic Alloys IV*, Edited by L.A. Johnson et al., Mat. Res. Soc. Symp. Proc., **213**, 1991, 777-794.
 58. Shyh-Chin Huang and Ernest L. Hall, Plastic Deformation and Fracture of Binary TiAl-Base Alloys, *Metall. Trans. A*, **22A(2)**, 1991, 427-439.
 59. Young-Won Kim, Intermetallic Alloys Based on Gamma Titanium Aluminide, *JOM*, **41(7)**, 1989, 24-30.
 60. Munetsugu Matsuo, Developments in Processing Technology of Gamma Titanium Aluminides for Potential Application to Airframe Structure, *ISIJ International*, **31(10)**, 1991, 1212-1222.
 61. J. C. Williams, Intermetallic compounds; as Assessment of Progress and Potential, *Structural Intermetallics*, Edited by R. Darolia et al., The Minerals, Metals & Materials Society, 1993, 839-844.
 62. Subhayu Sen and Doru M. Stefanescu, Melting and Casting Processes for High-Temperature Intermetallics, *JOM*, **43(5)**, 1991, 30-34.
 63. S.L. Semiatin et al., Homogenization of Ingot Metallurgy Near-gamma Titanium Aluminides, *High-Temperature Ordered Intermetallic Alloys IV*, Edited by L.A. Johnson et al., Mat. Res. Soc. Symp. Proc., **213**, 1991, 883-888.
 64. Young-Won Kim, Microstructural Evolution and Mechanical Properties of a Forged Gamma Titanium Aluminide Alloy, *Acta Metall. Mater.*, **40(6)**, 1992, 1121-1134.
 65. M. Morinaga et al., Electronic Effect on the Ductility of Alloyed TiAl Compound, *Acta Metall. Mater.* **38(1)**, 1990, 25-29.
 66. M.H. Yoo and C.L. Fu, Fundamental Aspects of Deformation and Fracture in High-Temperature Ordered Intermetallics, *ISIJ International*, **31(10)**, 1991,

1049-1062.

67. C. Woodward, Electronic Structure of Planar Faults in TiAl, *J. Mater. Res.*, **7(7)**, 1992, 1735-1750.
68. M.E. Eberhart, D.P. Clougherty and J.M. MacLaren, Bonding-property Relationships in Intermetallic Alloys, *J. Mater. Res.*, **8(3)**, 1993, 438-448.
69. Shih-Chin Huang and Donald S. Shih, Microstructure-Property Correlation in TiAl-Base Alloys, *Microstructure/Property Relationships in Titanium Aluminides and Alloys*, Edited by Young-Won Kim and Rodney R. Boyer, The Minerals, Metals and Materials Society, 1991, 105-121.
70. J.Y. Kim, Y.D. Hahn, and S.H. Whang, Dislocation Structure in γ Phase Grains of Ti₅₅Al₄₅ Alloy, *Scripta Metall.*, **25(3)**, 1991, 543-548.
71. Ernest L. Hall and Shyh-Chin Huang, Stoichiometry Effects on the Deformation of Binary TiAl Alloys, *J. Mater. Res.*, **4(3)**, 1989, 595-602.
72. Shyh-Chin Huang and Ernest L. Hall, The Effects of Cr Additions to Binary TiAl-Base Alloys, *Metall. Trans. A*, **22A(11)**, 1991, 2619-2627.
73. E. Mohandas and P.A. Beaven, Site Occupation of Nb, V, Mn, and Cr in γ -TiAl, *Scripta Metall.*, **25(8)**, 1991, 2023-2027.
74. T. Kawabata, Takashi, and O. Izumi, Parameters for Ductility Improvement in TiAl, *High-Temperature Ordered Intermetallic Alloys III*. Edited by C.T. Liu et al. *Mat. Res. Soc. Symp. Proc.*, **133**, 1989, 329-334.
75. T. Maeda, M. Okada, and Y. Shida, Ductility and Strength in Mo Modified TiAl, *High-Temperature Ordered Intermetallic Alloys IV*, Edited by L.A. Johnson et al., *Mat. Res. Soc. Symp. Proc.*, **213**, 1991, 555-560.
76. M. Nazmy and M. Staubi, Alloy Modification of γ TiAl for Improved Mechanical Properties, *Scripta Metall.*, **31(7)**, 1994, 829-833.
77. T.Kawabata, T. Tamura, and O. Izumi, Effect of Ti/Al Ratio and Cr, Nb, and Hf Additions on Material Factors and Mechanical Properties in TiAl, *Metall. Trans. A*, **24A(1)**, 1993, 141-150.
78. Kenki Hashimoto et al., Effects of Third Elements on the Structures of TiAl-based Alloys, *J. Japan Inst. Metals*, **52(8)**, 816-825.

79. B.A. Greenberg, M.A. Ivanov, A Comparison Analysis of the Deformation Behaviour of Al-rich and Ti-rich TiAl-based Compounds, *Structural Intermetallics*, Edited by R. Darolia et al., The Minerals, Metals & Materials Society, 1993, 293-298.
80. Keizo Hashimoto and Masao Kimura, Effects of third Element Additions on Mechanical Properties of TiAl, *Structural Intermetallics*, Edited by R. Darolia et al., The Minerals, Metals & Materials Society, 1993, 309-318.
81. Q. Gao and R.A. Varin, The Effect of Chromium and Annealing on the Crystallographic Parameters of γ Phase in TiAl-Based Alloys, *Scripta Metall.*, **31(7)**, 1994, 933-938.
82. Qu Xuanhui, Kong Xiangyan, Huang Boyun and Qian Yuan, Ductility Improvement of L1₀-TiAl Intermetallic Compounds by the Addition of Mn, *J. Cent.-South Inst. Min. Metall.*, **21(4)**, 1990, 191-197.
83. Shyh-Chin Huang, Alloying Considerations in Gamma-Based Alloys, *Structural Intermetallics*, Edited by R. Darolia, J.J. Lewandowski, C.T. Liu, P.L. Martin, D.B. Miracle and M.V. Nathal, The Minerals, Metals & Materials Society, 1993, 299-307.
84. P.K. Khowash, D.L. Price and B.R. Cooper, Energetics and Structural Effects of Boron Additive to Intermetallic Compound: γ -TiAl, *High-Temperature Ordered Intermetallic Alloys IV*, Edited by L.A. Johnson et al., *Mat. Res. Soc. Symp. Proc.*, **213**, 1991, 31-36.
85. Takeshi Kawabata, Masayoshi Tadano and Osamu Izumi, Effect of Carbon and Nitrogen on Mechanical Properties of TiAl Alloys, *ISIJ International*, **31(10)**, 1991, 1161-1167.
86. V.K. Vasudevan et al., Effect of Purity on the Deformation Mechanisms in the Intermetallic Compound TiAl, *Scripta Metall.*, **23(6)**, 1989, 907-912.
87. S.C. Huang and E.L. Hall, Structures and Properties of Gamma-TiAl Alloys Containing Interstitial Elements, *High-Temperature Ordered Intermetallic Alloys IV*, Edited by L.A. Johnson et al., *Mat. Res. Soc. Symp. Proc.*, **213**, 1991, 827-832.
88. Wu-Yang Chu and Anthony W. Thompson, Effect of Microstructure and Hydrides on Fracture of TiAl, *Scripta Metall.*, **25(9)**, 1991, 2133-2138.

89. S. Sriram et al., Deformation Mechanisms in TiAl-Based Alloys Containing Low Oxygen, *High-Temperature Ordered Intermetallic Alloys IV*, Edited by L.A. Johnson et al., Mat. Res. Soc. Symp. Proc., **213**, 1991, 375-384.
90. Hideyuki Ogishi et al., Effect of Chlorine Content on Tensile Properties of Titanium Aluminide, *ISIJ International*, **31(10)**, 1991, 1168-1171.
91. T. Kawabata et al., Effect of Purity and Second Phase on Ductility of TiAl, *Scripta Metall.*, **22(11)**, 1988, 1725-1730.
92. Yoo-Dong Hahn and Sung H. Whang, Deformation and Its Structure in L1₀ Ti-Al-Nb Compound Alloys, *High-Temperature Ordered Intermetallic Alloys III*. Edited by C.T. Liu et al., Mat. Res. Soc. Symp. Proc., **133**, 1989, 385-390.
93. Z.X. Li, J.Y. Kim and S.H. Whang, Decomposition of Superdislocations via Interaction with Ordinary Dislocations in γ -Titanium Aluminides, *Scripta Metall.*, **25(11)**, 1991, 2595-2600.
94. S.M. L. Sastry and H.A. Lipsitt, Fatigue Deformation of TiAl Base Alloys, *Metall. Trans. A*, **8A(2)**, 1977, 299-308.
95. B.Y. Huang et al., Compression Deformation Structures of Single Crystal TiAl, *High-Temperature Ordered Intermetallic Alloys III*. Edited by C.T. Liu et al., Mat. Res. Soc. Symp. Proc., **133**, 1989, 231-236.
96. Daniel S. Schwartz and W.O. Soboyejo, Relationships Between Deformation and Interfaces in γ -based Titanium Aluminides, *Microstructure/Property Relationships in Titanium Aluminides and Alloys*, Edited by Young-Won Kim and Rodney R. Boyer, The Minerals, Metals and Materials Society, 1991, 65-74.
97. T. Kawabata and O. Izumi, Dislocation Reactions and Fracture Mechanism in L1₀ Type Intermetallic Compound, *Scripta Metall.*, **21(4)**, 1987, 435-440.
98. Ernest L. Hall and Shyh-Chin Huang, Microstructural Studies of the Deformation of TiAl Alloys, *High-Temperature Ordered Intermetallic Alloys III*. Edited by C.T. Liu et al., Mat. Res. Soc. Symp. Proc., **133**, 1989, 693-698.
99. T. Kawabata and O. Izumi, Dislocation Structures in TiAl Single Crystals Deformed at 77K, *Scripta Metall.*, **21(4)**, 1987, 433-434.

100. W.T. Donlon, W.E. Dowling Jr., and J.E. Allison, Dislocation Structures in Deformed γ/α_2 Titanium Aluminides, *Microstructure/Property Relationships in Titanium Aluminides and Alloys*, Edited by Young-Won Kim and Rodney R. Boyer, The Minerals, Metals and Materials Society, 1991, 75-87.
101. M.H. Yoo, C.L. Fu and J.K. Lee, Deformation Twinning in Ordered Intermetallic Compounds, *High-Temperature Ordered Intermetallic Alloys III*, Edited by C.T. Liu et al., Mat. Res. Soc. Symp. Proc., **133**, 1989, 189-197.
102. ASM Committee on Stainless Steels and Heat-Resisting Alloys, Heat Treating of Heat-Resisting Alloys, *Source Book of Superalloys*, Edited by Matthew J. Conachie, Jr., ASM, 1984, 347-368.
103. ASM Committee on Cast Corrosion-Resisting and Heat-Resisting Alloys, Heat-Resistant Castings, *Source Book of Superalloys*, Edited by Matthew J. Conachie, Jr., ASM, 1984, 41-44.
104. G.E. Fuchs, Homogenization and Hot Working of Ti-48Al-2Nb-2Cr Alloys, *Structural Intermetallics*, Edited by R. Darolia et al., The Minerals, Metals & Materials Society, 1993, 195-202.
105. Young-Won Kim, Microstructural Evolution and Mechanical Properties in Gamma Titanium Aluminides, *Microstructure/Property Relationships in Titanium Aluminides and Alloys*, Edited by Y.W. Kim and Rodney R. Boyer, The Minerals, Metals & Materials Society, 1991, 91-103.
106. H.E. Deve, A.G. Evans, and D.S. Shih, A High-Toughness γ -Titanium Aluminide, *Acta Metall. Mater.*, **40(6)**, 1992, 1259-1265.
107. C. Suryanayana et al., Structural Evolution of Mechanically Alloyed Ti-Al Alloys, *Mater. Sci. and Engng.*, **A158(1)**, 93-101.
108. ASTM Designation E139: Standard Practice for Conducting Creep, Rupture, and Stress-Rupture Tests of Metallic Materials, *Annual Book of ASTM Standards*, **03.01.**, 1992.
109. B.F. Brown, *Stress-Corrosion Cracking in High Strength Steels and in Titanium and Aluminum Alloys*, Naval Research Laboratory, 1972.
110. Ashok Saxena, Electrical Potential Technique for Monitoring Subcritical Crack Growth at Elevated Temperatures, *Engineering Fracture Mechanics*, **13(4)**,

1980, 741-750.

111. H.H. Ottens and C.J. Lof, Compliances of a Tapered DCB Specimen Configurations by a Finite Element Method, *Engineering Fracture Mechanics*, **6(10)**, 1974, 573-585.
112. ASTM Designation E647: Test Method for Measurements of Fatigue Crack Growth Rates, *Annual Book of ASTM Standards*, **03.01.**, 1992.
113. J. Wayne Jones, Theory of Creep Deformation, *Metals Handbook*, Ninth Edition, ASM, **8**, 1985, 308-310.
114. ASTM Designation E1457: Standard Test Method for Measurement of Creep Crack Growth Rates in Metals, *Annual Book of ASTM Standards*, **03.01.**, 1992.
115. C.D. Liu, Y.F. Han, and M.G. Yan, Small-Scale Creep Crack Growth, *Engineering Fracture Mechanics*, **41(2)**, 1992, 229-239
116. M.H. Yoo et al. Deformation and Fracture of Intermetallics, *Acta Metall. Mater.*, **41(4)**, 1993, 987-1002.
117. D.L. Anton et al., Aspects on Microstructure and Mechanical Behavior of Three γ -TiAl base Alloys, *Structural Intermetallics*, Edited by R. Darolia et al., The Minerals, Metals & Materials Society, 1993, 265-273.
118. M. Nazmy, M. Staubli and D. Anton, Aspects of Mechanical Behavior of Two Gamma Ti-Aluminide Base Intermetallics, *Scripta Metall.*, **26(1)**, 1992, 105-108.
119. W.E. Dowling, Jr. et al., The Influence of Microstructure on the Mechanical Behavior of γ/α_2 Titanium Aluminides, *Microstructure/Property Relationships in Titanium Aluminides and Alloys*, Edited by Y.W. Kim and Rodney R. Boyer, The Minerals, Metals & Materials Society, 1991, 123-133.
120. B. Dogan, R. Wagner, and P.A. Beaven, Fracture Behaviour of a Ti-48.5Al-1Mn Alloy, *Scripta Metallurgica*, **25(4)**, 1991, 773-778.
121. R.M. Imayev, O.A. Kaibyshev, and G.A. Salishchev, Mechanical Behaviour of the Fine Grained TiAl Intermetallic Compound-I. Superplasticity, *Acta Metall. Mater.*, **40(3)**, 1992, 581-587.

122. F.H. Froes, C. Suryanarayana, D. Eliezer, Synthesis, Properties and Applications of Titanium Aluminides, *J. Mater. Sci.*, **27(19)**, 1992, 5113-5140.
123. Ernest L. Hall and Shyh-Chin Huang, Deformation Mechanisms in Gamma Titanium Aluminides: A Review, *Microstructure/Property Relationships in Titanium Aluminides and Alloys*, Edited by Young-Won Kim and Rodney R. Boyer, The Minerals, Metals and Materials Society, 1991, 47-63.
124. Kwai S. Chan and Young-Won Kim, Fracture Processes in a Two-phase Gamma Titanium Aluminide Alloy, *Microstructure/Property Relationships in Titanium Aluminides and Alloys*, Edited by Young-Won Kim and Rodney R. Boyer, The Minerals, Metals and Materials Society, 1991, 179-196.
125. D.L. Davidson and J.B. Campbell, Fatigue Crack Growth through the Lamellar Microstructure of an Alloy Based on TiAl at 25 °C and 800 °C, *Metall. Trans. A*, **24A(7)**, 1993, 1555-1574
126. T. Kawabata, T. Kanai, and O. Izumi, Positive Temperature Dependence of the Yield Stress in TiAl L1₀ Type Superlattice Intermetallic Compound Single Crystals at 293-1273K, *Acta Metall.*, **33**, 1985, 1355.
127. B.A. Greenberg et al., Dislocation Transformations and the Anomalies of Deformation Characteristics in TiAl-I. Models of Dislocation Blocking, *Acta Metall. Mater.*, **39(2)**, 1991, 233-242.
128. B.A. Greenberg et al., Dislocation Transformations and the Anomalies of Deformation Characteristics in TiAl-II. The Structure of dislocation Ensemble: Experiment and Theory, *Acta Metall. Mater.*, **39(2)**, 1991, 243-254.
129. S.C. Huang and E.L. Hall, On the Temperature Dependence of Yield Stress in TiAl Base Alloys, *Scripta Metall.*, **25(8)**, 1991, 1805-1809.
130. S. Krishnamurthy and Y-W. Kim, The Temperature Dependence of Tensile Behaviour of a Gamma Titanium Aluminide Alloy, *Microstructure/Property Relationships in Titanium Aluminides and Alloys*, Edited by Young-Won Kim and Rodney R. Boyer, The Minerals, Metals and Materials Society, 1991, 149-163.
131. T. Kawabata, T. Kanai, and O. Izumi, A Mechanism of the Positive Temperature Dependence of Yield Stress in TiAl, *High-Temperature Ordered Intermetallic Alloys IV*, Edited by L.A. Johnson et al., Mat. Res. Soc. Symp.

- Proc., **213**, 1991, 279-284.
132. S.C. Huang, Temperature Dependence of Microhardness and Yield Stress in Rapidly Solidified TiAl Alloys, *Scripta Metall.*, **22(12)**, 1988, 1885-1888.
 133. B.A. Greenberg, Anomalies in the Deformation Characteristics of Intermetallic TiAl: Theoretical Models, *Scripta Metall.*, **23(5)**, 1989, 631-636.
 134. Harry A. Lipsitt, Dan Shechtman, and Robert E. Schafrik, The Deformation and Fracture of TiAl at Elevated Temperatures, *Metall. Trans. A*, **6A(11)**, 1975, 1991-1996.
 135. W. Wunderlich, Th. Kremser, and G. Frommeyer, Mobile Dislocations at the α_2/γ Phase Boundaries in Intermetallic TiAl/Ti₃Al-Alloys, *Acta Metall. Mater.*, **41(6)**, 1993, 1791-1799.
 136. W. Wunderlich, G. Frommeyer and P.v. Czarnowski, Arrangement of Misfit Dislocations at Ti₃Al/TiAl Phase Boundaries, *Mater. Sci. and Engng.*, **A164(1-2)**, 1993, 421-427.
 137. R.V. Ramanujan et al., A Discrete Lattice Plane Analysis of the Energy of Coherent $\{0001\}_{\text{h.c.p.}}//\{111\}_{\text{f.c.c.}}$, $\langle 1120 \rangle_{\text{h.c.p.}}//\langle 110 \rangle_{\text{f.c.c.}}$ Interfaces, *Acta Metall.*, **37(11)**, 1989, 3051-3059.
 138. F. Appel, P.A. Beaven and R. Wagner, Deformation Processes Related to Interfacial Boundaries in Two-phase γ -Titanium Aluminides, *Acta Metall. Mater.*, **41 (6)**, 1993, 1721-1732.
 139. L. Zhao and K. Tangri, TEM Investigation on the Interfacial Boundaries in As-cast Ti₃Al+TiAl Alloy, *Acta Metall. Mater.*, **39(10)**, 1991, 2209-2224.

VITA

The author was born on January 13, 1958, in Haiian, Jiangsu, China. He enrolled at East China Institute of Technology in 1978 and received his B.E. degree and M.S. degree in Metallic Material and Heat Treatment in 1982 and 1985, respectively. Then he worked there as a lecturer and a researcher for five years.

The author joined Oregon Graduate Institute in 1990 to pursue a Ph. D. degree in Materials Science and Engineering. He completed the requirements for the Doctor of Philosophy degree in April 1995.